Regional and laminar organization of the entorhinal cortex in tree shrews based on cytoarchitecture, chemoarchitecture, and connectivity

Running title: Subdivisions and layers of the tree shrew entorhinal cortex

Yi-Fan Ye[1,2,5], Chu Deng[1,2,5], Xiao-Fan Ge[1,2], Rong Zhang[1,3], Jia-Li Long[1,2], Jia-Xue Jia[1,2], Hao-Yun Ye[1], Cheng-Ji Li[1,3], Xing Cai[1,3], Menno P. Witter[4], & Li Lu[1,3,6]

[1] State Key Laboratory of Genetic Evolution & Animal Models, and Key Laboratory of Animal Models & Human Disease Mechanisms of Yunnan Province, Kunming Institute of Zoology, Chinese Academy of Sciences, Kunming, Yunnan 650201, China.

[2] Kunming College of Life Science, University of Chinese Academy of Sciences, Kunming, Yunnan 650204, China.

[3] National Resource Center for Non-Human Primates, Kunming Primate Research Center, and National Research Facility for Phenotypic & Genetic Analysis of Model Animals (Primate Facility), Kunming Institute of Zoology, Chinese Academy of Sciences, Kunming, Yunnan 650107, China.

[4] Kavli Institute for Systems Neuroscience, NTNU Norwegian University of Science and Technology, Trondheim 7491, Norway.

[5] Equal contributions.

[6] Correspondence: luli@mail.kiz.ac.cn, phone number: (+86-871-65155338).

Abstract

The entorhinal cortex (EC) is a pivotal interface that integrates multimodal cortical and subcortical information into the hippocampal formation and distributes hippocampal output to widespread telencephalic targets. It is also one of the earliest and most

severely affected regions in Alzheimer's disease (AD). The tree shrew (*Tupaia belangeri chinensis*) has emerged as a promising model for AD research. However, the uncharted organization of tree shrew EC has limited its application in modeling early stages of AD. In this study, we provide a comprehensive anatomical reference for the tree shrew EC by delineating its boundaries, parcellating its medial and lateral subregions, and mapping its laminar connectivity based on cyto- and chemoarchitecture combined with tracing experiments. We found that the tree shrew EC exhibits an intermediate architecture between rodents and monkeys, mirroring its phylogenetic position and potentially links to the gradual evolution of place codes from rodents to primates. This study provides the first detailed entorhinal atlas of this species, establishing a critical foundation for future neural-tracing and electrophysiological investigations. It enhances the utility of the tree shrew in mechanistic studies of spatial coding, conscious memory, as well as a naturalistic model for incipient AD.

Keywords: tree shrew entorhinal cortex, delineation and parcellation, laminar organization, cytoarchitecture, chemoarchitecture, connectivity

Foundation items

This research was supported by the Brain Science and Brain-like Intelligence Technology - National Science and Technology Major Project (2022ZD0205000 to L.L.), CAS "Light of West China" Program (xbzg-zdsys-202404 to L.L.), Yunnan Revitalization Talent Support Program Yunling Scholar Project (to L.L.), Yunnan Fundamental Research Projects (202305AH340006, 202301AS070060 to L.L., and 202401AT070206 to X.C.).

Introduction

The EC was first identified by Ramón y Cajal over a century ago as the origin of the most massive cortical projection to the hippocampus (Ramón Y Cajal, 1902). Contemporary neural-tracing and functional-imaging studies have since refined this view, revealing the EC as the pivotal interface that funnels multimodal neocortical information into the hippocampal formation and, in turn, distributes hippocampal output back to widespread cortical and subcortical targets (Canto et al., 2008; Cappaert et al., 2015; Insausti et al., 1987a;b; Kerr et al., 2007; Witter and Amaral, 1991;2021; Zeineh et al., 2017). However, rather than serving as a simple passive relay station, the EC actively transforms and integrates incoming information before it reaches the hippocampus, acting as a dynamic hub that orchestrates mnemonic, spatial, and temporal computations essential for episodic memory and spatial navigation (Eichenbaum, 2017; Moser et al., 2017; Sugar and Moser, 2019).

The EC is exquisitely vulnerable to pathological insult. Structural and functional compromise has been documented across a spectrum of neuropsychiatric and neurodegenerative disorders, including paraphrenia (Casanova, 2010), schizophrenia (Li et al., 2025), and temporal-lobe epilepsy (Vismer et al., 2015). Most notably, the EC is one of the earliest and most severely affected cortical regions in AD (Igarashi, 2023; Karimani et al., 2024; Kobro-Flatmoen et al., 2021; Olajide et al., 2021; Setti and Reed, 2022). Post-mortem staging demonstrates that neurofibrillary tangles first appear in the EC followed by the hippocampus and association cortices (Arnold et al., 1991; Braak and Braak, 1991). In vivo imaging corroborates these histological findings, revealing EC atrophy in cognitively normal individuals who later progress to mild cognitive impairment (Kulason et al., 2019; Kulason et al., 2020; Tward et al., 2017; Zhou et al., 2016). Studies in rodent models of amyloidosis and tauopathy further confirm the sequential appearance of AD pathology in the brain, interpreted to be indicative of transsynaptic spread of AD from EC to its downstream targets (De Calignon et al., 2012; Pickett et al., 2017; Pignataro and Middei, 2017), culminating in progressive dysfunction (Fu et al., 2017; Jun et al., 2020; Ying et al., 2022). Despite

these insights, the translational value of rodent models is constrained by divergences in genetics, cortical organization, and aging relative to humans. Larger non-human primates offer closer homology, but their use is limited by prohibitive costs, protracted life spans, technical challenges, and ethical considerations (Alexandra Lopes and Guil-Guerrero, 2025; Yenkoyan et al., 2025). An intermediate model that balances genetic and anatomical proximity to humans with experimental tractability is therefore urgently needed.

The Chinese tree shrew (*Tupaia belangeri chinensis*) has emerged as a compelling candidate. Endemic to the subtropical forests of southwest China and Southeast Asia (Yao et al., 2024), this small, diurnal mammal occupies an evolutionary position markedly closer to primates than to rodents (Fan et al., 2013; Fan et al., 2019; Xu et al., 2012; Ye et al., 2021). Its 6–8-year lifespan permits longitudinal studies of age-related neurodegeneration within a practical timeframe (Li et al., 2024a; Li et al., 2024b; Savier et al., 2021; Yao et al., 2024). Crucially, tree shrews share an identical beta-amyloid (Aβ) amino-acid sequence with humans and express AD susceptibility genes at comparable levels (Fan et al., 2018; Pawlik et al., 1999; Ye et al., 2021). Spontaneous, age-dependent accumulation of Aβ plaques, hyperphosphorylated tau, synaptic and neuronal loss, reactive gliosis, together with cognitive deficits, have been documented in the brain of aged tree shrews (Fan et al., 2018; Li et al., 2024b; Yamashita et al., 2010; Yamashita et al., 2012), phenomena seen in primates but not in rodents (Paspalas et al., 2018; Yamashita et al., 2012). After hippocampal infusion of Aβ42 oligomers, tree shrews develop robust AD-like pathology accompanied by spatial-memory deficits (Lin et al., 2016; Wang et al., 2020b), phenotypes that closely resemble early-stage human AD (Coughlan et al., 2018). These convergent lines of evidence position the tree shrew as a powerful model for studying AD and brain aging. However, as a relatively new model, it remains underexploited owing to the limited availability of standardized neuroanatomical data, especially the cytoarchitecture and connectivity of the EC. Previous publications have provisionally delineated the entorhinal region without detailed anatomical descriptions (Skeen and Hall, 1977; Wong and Kaas, 2009; Zhou

and Ni, 2016), impeding EC-focused AD research in this species.

In this study, leveraging the high-resolution images recently published by our group (Zhang et al., 2025) that detail the distribution of parvalbumin (PV), calbindin (CB) and calretinin (CR) alongside Nissl and neuronal nuclei (NeuN) in sagittal, coronal and horizontal planes, we provide a refined parcellation and laminar description of the tree shrew EC. Using this comprehensive cyto- and chemoarchitectonic dataset, we first delineated the precise boundaries between EC and adjacent structures, then segregated it into medial and lateral subdivisions based on cytoarchitecture and PV/CB/CR immunoreactivity. Multi-channel immunofluorescence and anterograde/retrograde tracing subsequently validated key architectonic borders and layers, each distinguished by distinct chemoarchitectonic and connectional signatures. The resultant map shows an EC architecture intermediate between rodents and primates, consistent with the tree shrew's phylogenetic position (Fan et al., 2013; Fan et al., 2019; Xu et al., 2012; Ye et al., 2021) and with the proposed gradual evolution of place codes across mammals (Mao et al., 2021; O'keefe, 1976; O'keefe et al., 1998).

By integrating cyto-, chemo- and connectional data, the present work delivers the first comprehensive cytoarchitectonic and connectional map of EC in this tree shrew species. This framework provides an essential anatomical foundation for future neural-tracing and electrophysiological investigations and enhances the utility of the tree shrew as a naturalistic model for early-stage AD, in which EC pathology is among the earliest detectable changes.

Materials and methods

Subjects

The experiments were conducted at the Kunming Institute of Zoology, Chinese Academy of Sciences (Kunming, China) in compliance with the guidelines for the care and use of laboratory animals. The study received approval from the Institutional

Animal Care and Use Committee of the Kunming Institute of Zoology (IACUC-TE-2021-06-001). The majority of the cytoarchitectonic data were obtained from a published resource (Zhang et al., 2025), and in this study additional immunostaining and tracing data were collected from 34 adult Chinese tree shrews, including 27 males and 7 females, aged 14–37 months and weighting 120–160g. The animals were housed under standard laboratory conditions (temperature: 20–26°C, relative humidity: 40–60%) with a 12-h light/dark cycle. Food and water were provided *ad libitum*.

Western blot analysis

The primary antibodies used have been verified in western blot analyses for their affinity and specificity (Supplementary Figure S1). Animals were euthanized using CO_2 and fresh brain tissue was collected without perfusion and immediately frozen at −80°C. Proteins were then extracted using radio immunoprecipitation assay lysis buffer (Beyotime, China, Cat # P0013B) supplemented with phenylmethylsulfonyl fluoride (Beyotime, China, Cat # ST507). The extracted protein samples were combined with sodium dodecyl sulfate-polyacrylamide gel electrophoresis (SDS-PAGE) loading buffer and boiled at 99°C for 15 min to denature the proteins. The denatured samples were then loaded onto an SDS-PAGE gel consisting of a 4% stacking gel and a 12.5% resolving gel for separation and transferred to polyvinylidene difluoride membranes. The membranes were blocked in a 5% skimmed milk solution in PBST buffer (Phosphate-buffered saline with Tween-20) at room temperature for 1 h. The blocking solution was then discarded, and the membranes were incubated with primary antibodies diluted 1:1000 overnight at 4°C. Following primary antibody incubation, the membranes were washed with PBST buffer for 5–10 min, 3–5 times. The membranes were then incubated with horseradish peroxidase (HRP)-conjugated goat anti-rabbit IgG (H+L) antibody and HRP-conjugated goat anti-mouse IgG (H+L) antibody (Beyotime, China, Cat # A0208 & A0216) diluted 1:1000 at room temperature for 2 h. Finally, the membranes were again washed with PBST buffer and developed using an enhanced chemiluminescence kit (Uelandy, China, Cat # S6009L) with a GeneGnome XRQ Chemiluminescent Imaging System (Syngene, UK).

Neural tracing

The procedure for stereotaxic injection in tree shrews has been described (Li et al., 2023). Tree shrews were anesthetized with isoflurane (airflow: 0.8–1.0 L/min, 0.5–3% isoflurane mixed with oxygen, adjusted according to physiological monitoring, RWD Life Science, China). Body temperature was maintained at approximately 38 °C using a heating pad underneath the body with a closed-loop controller connected to a rectal temperature probe. Upon induction of anesthesia, Metacam (2 mg/mL, 1 mg/kg) and Baytril (50 mg/mL, 5 mg/kg) were injected subcutaneously, and the animal's head was fixed in a stereotaxic frame (RWD Life Science, China) with a custom-designed gas mask. Local anesthetic (2% Lidocaine, 200 μL) was applied under the skin before making the incision. When necessary, the temporalis muscle was gently detached from the skull and slightly moved, such that holes could be drilled in the skull above the target regions.

Viruses or neural tracers diluted in sterile phosphate-buffered saline (PBS, pH 7.2) were injected using a sharp 5 μL syringe (Hamilton, USA) mounted to the stereotaxic frame (needle opening directed caudally), at an infusion speed of 10 μL /h using a micro pump (KD Scientific, USA). For each animal, only one single injection was made in the left hemisphere, using bregma as a reference for infusion coordinates. For anterograde tracing to map the spread of presubicular neuronal terminals in the EC, mixed adeno-associated virus (AAVs) expressing enhanced green fluorescent protein (AAV-CMV-eGFP, labeling neuron soma and main fibers, Table 1) and tdTomato conjugated synaptophysin (AAV-hSyn-SYP-tdTomato, specifically labeling fiber terminals) were injected into the dorsal or the ventral portion of presubiculum (dorsal: anteroposterior (AP) 7.5 mm, mediolateral (ML) 6.0 mm, dorsoventral (DV) 6.0 mm; ventral: AP 4.5 mm, ML 4.5 mm, DV 11.0 mm). For transsynaptic anterograde tracing in the hippocampus to label the layer V neuron somata in the EC, AAV-hSyn-Cre was injected into the dorsal CA1 and subiculum (dorsal: AP 4.5 mm, ML 5.0 mm, DV 4.0 mm). For retrograde labeling of hippocampus-projecting neurons in the EC, Alexa488 conjugated cholera toxin subunit B (CTB) was injected into the dorsal hippocampus

aiming at both the stratum lacunosum-moleculare of CA1 and the molecular layer of the dentate gyrus (AP 4.5 mm, ML 5.2 mm, DV 4.5 mm). For retrograde labeling of projecting layer V and VI neurons in the EC, Alexa555 conjugated CTB was injected into the nucleus accumbens (AP −4.3 mm, ML 1.5 mm, DV 7.1 mm), amygdala (AP −0.3 mm, ML 4.5 mm, DV 11.5 mm), retrosplenial cortex (AP 4.9 mm, ML 2.5 mm, DV 3.2 mm) (Ohara et al., 2018; Ohara et al., 2021b; Sürmeli et al., 2015), secondary visual cortex (AP 4.1 mm, ML 5.2 mm, DV 2.2 mm) (Lu et al., 2022), or laterodorsal thalamic nucleus (AP 2.2 mm, ML 3.0 mm, DV 6.0 mm) (Aggleton et al., 1986).

For each injection, the needle was first lowered into the brain up to a point directly below the intended injection site and then retracted 0.1 mm. The injection started 1 min after the needle was positioned. After the injection, the needle was left in place for 10 min to allow absorption. When the injections were completed, the skull was cleaned with saline solution, and the skin was sutured. The animals received post-operative care, including soft food, analgesics, and antibiotics for three days, followed by a recovery period with access to free food and water until euthanasia.

Histological preparation

Animals were euthanized using CO_2 and perfused transcardially with 0.9% saline, followed by 4% paraformaldehyde (PFA) in 0.1 mol/L phosphate buffer. Brains were removed from the skull and further fixed overnight in 4% PFA, and sequentially cryoprotected in 20% and 30% sucrose solutions at 4°C for 1–2 weeks until sectioning. The brains were then sectioned on a cryostat (DAKEWE, China, CT520) along the sagittal or coronal planes at a thickness of 40 μm. The brain sections were collected in PBS in 24-well plates and subsequently stained for Nissl, or immunofluorescence when needed.

Nissl staining

Nissl staining was performed for delineation purposes. Brain sections were mounted on microscope slides (CITOGLAS, China) and soaked in distilled water for 2 min. They were then dehydrated through a graded series of ethanol solutions (70%, 80%, 90%,

100%, 100%, and 100%), cleared in xylene, and rehydrated in reverse order in the same set of ethanol baths before being soaked in a solution containing 70% ethanol and 0.5% acetic acid (HAc-EtOH solution) for 5 min, followed by staining with 0.1% cresyl violet solution (Sigma-Aldrich, CAS: 10510-54-0, Cat # C5042-10g) for 5–10 min. Staining was differentiated by dipping the sections in HAc-EtOH solution. Finally, the sections were dehydrated in ethanol baths, cleared in xylene, and cover-slipped with neutral balsam.

Immunofluorescence

Immuno-fluorescence experiments were conducted to visualize neurons expressing specific protein markers. As previously described (Zhang et al., 2025), free-floating brain sections were first blocked with 3% normal goat serum (NGS, Beyotime, China, Cat # C0265) in PBS on a shaker set at 80 r/min for 1 h at room temperature. Sections were then incubated with primary antibodies (Table 2) diluted in PBS containing 3% NGS and 0.5% Triton X-100 (dilutions: CB, CR, 1:5000; NeuN, Purkinje-cell protein 4 (PCP4), 1:1000; Cre 1:2000) on a shaker at 4°C overnight. After three washes in PBS (10-min each), the sections were incubated with fluorescent dye-conjugated secondary antibodies (Table 3) diluted in PBS with 3% NGS and 0.5% Triton X-100 (dilution 1:500) on a shaker at room temperature for 2 h. Following another three washes in PBS (10-min each), the sections were mounted on microscope slides and cover-slipped with anti-fade mounting medium.

Digital photomicrography

Nissl-stained brain sections were imaged using a bright-field microscope equipped with a 10×, 0.4 NA objective (RRID: SCR_020343) (Olympus, BX61, Japan). Images were captured in arrays of fields of view (FOVs) at a resolution of 0.69 μm per pixel, then reconstructed and corrected for shading artifacts using OlyVIA v 3.2 (Build 21633, RRID: SCR_016167) (Olympus, Japan). Fluorescence microscopic images of brain sections were captured using a Confocal Tissue Cytometer equipped with a 10×, 0.3 NA objective (TissueGnostics, TissueFAXS PLUS, Austria). Images were acquired in

arrays of FOVs at a resolution of 0.65 μm per pixel, and reconstructed using TissueFAXS Viewer v 7.1 (Build 6245.0119) (TissueGnostics, Austria). The fluorescent images were acquired in monochrome, and color maps were applied to the images post-acquisition. Post hoc linear brightness and contrast adjustment were applied uniformly to the image under analysis.

Quantitative analyses

Unfolded flat map and areal sizes: The medial and lateral subdivisions of the EC were marked onto the line drawings of series of coronal sections spaced 120 μm, and the sections were then aligned with each other along the course of the rhinal sulcus (rs). The interval between each line was maintained in the flat representation and the surface line was stretched to create the unfolded flat map. The dorsal boundary was the border between the EC on the one hand, and the perirhinal cortex (PER) at rostral levels and the postrhinal cortex (POR) at caudal levels on the other hand. The anterior boundary was the border between the EC and the piriform cortex (PIR) dorsally, and the periamygdaloid cortical area (PAA) ventrally. The medial boundary was the border between the EC and the parasubiculum (PaS). The area of EC subregions was then measured from the lines in the unfolded maps. Note that for the caudal extreme of the medial EC division (MEC), where the deep layers are not present in the coronal sections, the unfolded map was supplemented by data from sagittal sections spaced 240 μm.

PV-immunoreactive (-ir) somata and neuropil density: Brains from the published dataset (Zhang et al., 2025) were analyzed: sagittal sections (T031, T046, T072) for the MEC and coronal sections (T054, T071, T098) for the lateral EC division (LEC). Sections were sampled every 240–720 μm, spanning the entire mediolateral (MEC) or anteroposterior (LEC) extent. For each section, MEC or LEC was manually divided into three equally sized proximal, middle and distal bands relative to the rs, following prior work (Kobro-Flatmoen and Witter, 2019). Regions of interest (ROIs) were

outlined by hand, and their area (in mm^2) and mean PV fluorescence intensity were measured in ImageJ (RRID: SCR_003070) (Schneider et al., 2012). Relative PV intensity was expressed as the ratio of ROI fluorescence to that of the neocortex. PV-ir somata density was calculated as the number of labeled neurons per mm^2 of the ROI.

CTB-CB co-localization: Brains from four retrograde-tracing experiments were analyzed. Sections were sampled every 240–480 μm across the entire EC exhibiting CTB signals. For each section, layers II and III of both MEC and LEC were manually delineated and labeled somata in each region were counted. The co-localization ratio was defined as the percentage of CTB-CB double positive neurons among all retrogradely labeled neurons in that region.

Statistics

Results are presented as mean ± standard error of the mean (SEM). Independent and related samples were compared using the *t*-test and the paired *t*-test, respectively. One-way analysis of variance (ANOVA) for repeated measures was applied to compare EC subregions proximal and distal to the rs. Tukey corrections were applied for multiple comparisons to reduce the likelihood of false positives. Significance was set to $P < 0.05$ and was given for two-tailed tests. Statistical analyses were performed using GraphPad Prism v 9 (RRID:SCR_002798) (GraphPad, USA).

Results

Location of the tree shrew entorhinal cortex

The general topographical position of the tree shrew EC is outlined here; precise cytoarchitectonic boundaries with adjacent areas are defined in the subsequent section. In the tree shrew, EC occupies the ventrocaudal pole of the cerebral hemisphere, forming a cup-shaped sheet that drapes over the lateral, caudal, and medial surfaces (Figure 1A). Relative to the rat, the tree-shrew EC is positioned slightly more ventrally, and located partially in the piriform lobe. Aligning to the stereotaxic atlas (Zhou and Ni, 2016), its rostro-caudal extent spans coronal planes 3.8–8.8 mm posterior to Bregma; medio-laterally it measures 1.6–9.2 mm from the midline, and dorso-ventrally it lies 8.0–13.0 mm below the dorsal cortical surface. These dimensions correspond to a surface area slightly over 23 mm^2 (Figure 1A iv), comparable to the EC in rats (~21 mm^2) (Naumann et al., 2016; Ray and Brecht, 2016).

The tree shrew EC borders the same group of cortical structures described in rodents, monkeys, and humans (Amaral et al., 1987; Boccara et al., 2015; De Gois Morais et al., 2020; Insausti et al., 1995; Piguet et al., 2018; Skeen and Hall, 1977; Van Groen, 2001), although their precise spatial relationships differ across species at various anatomical levels. Similar to rats, the dorsal border of tree shrew EC runs largely along the rs, which is deep and sharply incised rostrally and becomes progressively less discernible caudally. Along the sulcus, the EC is surrounded by the PER rostrolaterally, and by the POR caudally (Figure 1Ai). The PER lines the fundus and both banks of the rs at rostral levels, and is confined to the fundus and dorsal bank at caudal levels. Moving caudally, the superficial layers of POR lie in the fundus of the rs, whereas its deep layers ascend dorsally above the sulcus. Medially, the PaS borders the EC along nearly its entire dorsoventral extent (Figure 1Aii). The dorsal edge of the PaS curves laterally to insinuate itself between the POR and EC. Consequently, the medial half of POR faces PaS rather than EC. Whereas this lateral extension of PaS is highly variable in rats (Boccara et al., 2015; Tang et al., 2016), it is remarkably consistent across individual tree shrews. Anteriorly, the EC is flanked laterally by the PIR and medially by the periamygdaloid cortex and/or the cortical nucleus of the amygdala (Figure 1Aiii). To ease the description in this paper, we will refer to both these areas together as the PAA.

To indicate the relative areal extents, we generated an unfolded two-dimensional map of the EC based on coronally and sagittally sectioned brains (Figure 1Aiv; see methods for details).

Layers of the tree shrew entorhinal cortex

Although the definition of entorhinal layers has evolved over time and differs among species, we adopted the scheme originally proposed by Ramón y Cajal, and updated to align with most recent rodent and primate literature (Boccara et al., 2015; Kobro-Flatmoen and Witter, 2019; Ohara et al., 2021b). Consistent with other mammals, the tree shrew EC comprises six layers, with four cellular layers (layers II, III, V and VI) sandwiched between two plexiform layers (layer I and IV) and the innermost white matter (WM) (Figure 1B).

Superficial layers: Layer I is the outermost layer with very low number of scattered neurons. In the rostrolateral part of the EC, which is largely coincident with the descriptions of the typical LEC in rodents, layer II is characterized by a sheet of very densely packed but somewhat discontinuous outer layer (IIa) that is composed of strongly stained large neurons in Nissl and NeuN stains. A very narrow, relatively acellular band separates layer IIa from the inner layer (IIb) in much of the region. Layer IIb is a narrow and less cell-dense band of medium-sized neurons often arranged in clusters (Figure 1B, top panel). Note that layer IIb was originally defined as the superficial layer III by Cajal, who emphasized that layer II is rather narrow and dominated by large neurons (Kobro-Flatmoen and Witter, 2019). This definition is still used in a number of recent studies in primates (De Gois Morais et al., 2020; Insausti et al., 2017; Piguet et al., 2018). Moving caudally, in the region that largely coincides with classical rodent MEC, the two sublayers merge into a single, homogeneous layer II composed of intermingled medium and large neurons that stain densely for Nissl and NeuN, which is sharply delimited from neighboring layers I and III (Figure 1B, bottom panel). In some animals, a very narrow, acellular band is present between layer II and

III of MEC. Layer III of the EC is wide and contains loosely arranged, medium-sized pyramidal neurons.

Deep layers: Layer IV (lamina dissecans) is a cell-sparse zone that separates the superficial and deep layers of the EC. It is generally more conspicuous adjacent to the rs. The wide cellular band between layer IV and the WM can be divided into two equally sized layers: the superficial layer containing loosely arranged medium-to-large pyramidal cells, and the deep layer with tightly arranged smaller neurons with more intense NeuN labeling (Figure 1B). In rodents and bats, these two layers have been designated layers Va and Vb, with a thin layer VI blending into the underlying WM (Boccara et al., 2015; Jacobsen et al., 2023; Sürmeli et al., 2015; Van Strien et al., 2009). However, our forthcoming staining and tracing data indicate that the superficial layer is layer V without further stratification (more in line with a recent report in the macaque monkey (Ohara et al., 2021b), whereas the compact deep layer corresponds to a distinct layer VI that is clearly separated from the WM. Scattered neurons within the WM become increasingly numerous toward the dorsal and medial borders of the EC with the PaS (Figure 1B).

Boundaries of the tree shrew entorhinal cortex

The resource images are presented as triplets of sections stained for (i) Nissl, (ii) NeuN & CB, and (iii) PV & CR. These stains reveal cytoarchitectonic details and the chemoarchitectonic signatures of the three calcium binding proteins (CaBPs) (Zhang et al., 2025). Thus, boundaries within the EC, and between EC and adjacent structures were therefore defined by integrating cytoarchitectonic criteria with the distribution patterns of PV, CB and CR. To visualize the boundaries and subregions of the EC in detail, we show representative series of tree shrew brain sections in coronal (Figures 2, S2–S7), sagittal (Figures 3, S8–S15) and horizontal (Figures 4, S16–S21) planes spanning the entire EC from the resource dataset. Section levels are referenced to the closest matching plane in the tree shrew brain atlas (Zhou and

Ni, 2016). Precise case identifiers are listed in Supplementary Table S1.

Dorsal border with PER and POR: As in rodents (Beaudin et al., 2013; Burwell, 2001), the dorsal margin of the EC is formed by PER rostrolaterally and POR caudally, with the boundary running approximately along the rs (Figure 1A). Rostrally, PER occupies the fundus and both banks of the sulcus (Figures S3B–F). Caudally, the rs becomes shallower and its ventral bank is progressively occupied by EC (Figures 2B–F, S6B–F). POR, situated caudally to PER, lies along the dorsal bank of the rs and abuts the EC dorsally (Supplementary Figure S7B–F). Cytoarchitectonically, both PER and POR can be distinguished from the EC by (i) narrower layer I, (ii) poorly differentiated, blended layers II/III consisting of small, lightly stained neurons, and (iii) absence of the lamina dissecans (panels B and C in Figures 2, S5, S6, S14, S17 and S18). Chemoarchitectonically, distribution patterns of PV, CB and CR in the tree shrew PER and POR closely resemble those in rats (Barinka et al., 2012; Boccara et al., 2015; Miettinen et al., 1997; Salaj et al., 2021). Layer IV neurons of PER and POR are strongly CR-ir, contrasting with the intense CR labeling of layer V in the adjacent EC (panel F in Figures 2, 4, S12, S13, S14 and S15). In addition, PER and POR exhibit low PV and strong CB expression, particularly in superficial layers. However, due to the regional variations in PV and CB expression within EC, these markers reliably delimit PER/POR only at dorsocaudal levels (panels D and E in Figures S7, S12, S13, S14 and S17), not at lateral or rostral levels (panels D and E in Figures 2, 4, S3–S6, S15, S18–S21).

Medial border with PaS: Across most of its dorsoventral extent, EC is bordered medially by PaS, which is characterized by the virtual fusion of layers II and III. PV, CB and CR profiles are grossly similar in PaS and adjacent EC, but EC displays a more laminated PV pattern in superficial layers, and PaS exhibits a distinct CR-ir sublayer immediately beneath the pia surface (Figures 4E, F). In addition, the dorsal tip of PaS curves laterally around the mediodorsal end of MEC (Supplementary Figure S16), showing prominent CB labeling not observed at ventral levels (Figures 3D, S12D and S13D).

Anterior border with PIR and PAA: This border is indicated by the reduction of laminar organization. The PIR flanks much of the EC along its lateral-to-medial axis and has a typical trilaminar structure with a densely packed and heavily Nissl-positive layer II and a loosely arranged layer III. The medially bordering transitional PAA shows a rudimentary trilaminar organization, in which layer II neurons become progressively dispersed and merge with layer III. The transition from EC to PIR/PAA is marked by the abrupt loss of the strong CR-ir band in EC layer V (panel F in Figures 3, S8–S14, S19–S21).

Medial and lateral divisions of the tree shrew entorhinal cortex

In rodents, primates, and other mammals, the EC has been parcellated into multiple cytoarchitectonic subregions (Amaral et al., 1987; De Gois Morais et al., 2020; Gatome et al., 2010; Insausti et al., 1997; Insausti et al., 1995; Piguet et al., 2018; Uva et al., 2004; Van Groen, 2001; Woźnicka et al., 2006). A simpler, functionally grounded scheme partitions the EC into a rostrolateral (LEC) and a caudomedial (MEC) region (Cappaert et al., 2015; Kobro-Flatmoen and Witter, 2019; Witter et al., 2017), distinguished by their reciprocal connectivity with the hippocampus and parahippocampal cortices (Canto et al., 2008; Jacobsen et al., 2023; Kerr et al., 2007; Suzuki and Amaral, 1994; Witter, 2006;2007; Witter and Amaral, 1991;2021). Guided by the principle that anatomical connectivity constrains cognitive function, we here delineate the tree shrew EC into MEC and LEC using cytoarchitectonic criteria, supplemented by chemoarchitectonic features.

Medial entorhinal cortex: The tree shrew MEC occupies the caudal and medial portion of EC, covering 10.56 ± 0.14 mm^2 of the surface in sagittal sections (delineation detailed below). Medially it adjoins the PaS and laterally it borders the LEC. Dorsally, MEC meets the POR laterally and PaS medially; ventrally, it transitions into LEC (Figure 1A). As in rodents, the tree shrew MEC exhibits an overall highly organized laminar cytoarchitecture (Boccara et al., 2015). A cell-

sparse lamina dissecans (layer IV) separates superficial layers II–III from deep layers V–VI. NeuN or Nissl staining reveals layer II as a compact band of mixed medium- and large-sized, heavily stained neurons. Besides its regular appearance, layer II is also characterized by the presence of cell clusters that protrude into layer I, making a wart-like appearance at the layer I–II border (Figures 4B, C and S5B, C), matching descriptions in rodents (Kitamura et al., 2014; Naumann et al., 2016; Ray et al., 2014). Layer III contains medium-sized pyramids that are homogeneously distributed along the entire extent of MEC. Layer V is populated by medium-sized neurons that are loosely arranged at the border with the lamina dissecans, whereas in the deep part of the layer, these cells tend to be somewhat more tightly arranged. Layer VI comprises densely packed smaller neurons with stronger NeuN expression (Figure 1B, bottom panel). The deep layers V and VI show a clear columnar arrangement (Figures S17B, C and S18B, C), comparable to observations in other species (Boccara et al., 2015; De Gois Morais et al., 2020; Gatome et al., 2010; Insausti et al., 2017; Insausti et al., 1995; Jacobsen et al., 2023; Piguet et al., 2018; Uva et al., 2004; Van Groen, 2001). Along the dorsoventral axis, the part of MEC adjacent to PaS is often thicker than the region close to LEC in sagittal sections (Figures S10B–E).

The lateral entorhinal cortex: The LEC lies rostral to MEC, and is slightly larger (12.69 ± 0.47 mm^2, *t*-test, $t = 3.782$, $P = 0.013$, df = 5; delineation detailed below). Dorsolaterally, it borders the PER and the rostral end of POR; ventrally, it adjoins the PIR laterally and the PAA medially (Figure 1A). The lamination of LEC is less organized (Figure 1B), such that most of the features characterized for MEC change rather abruptly at the border with LEC. A narrow transition zone with attenuated layers II and III marks the MEC-LEC border (Figures 3B, C), before the characteristic splitting of layer II into densely packed heavily stained large IIa neurons and less densely packed lightly stained medium-sized IIb neurons. Layer III of LEC also contains loosely arranged neurons but the inter-neuronal spacing is irregular compared with the homogeneously distributed layer III neurons in MEC (Figure 1B). In addition, layer III neurons tend to form clumps in the ventral portion

(Supplementary Figure S11C). Layer IV is rudimentary, so that layer III often abuts layer V. Layer V comprises loosely arranged medium to large pyramids (panels B and C in Figures 3, 4). Layer VI neurons are smaller and denser than those in layer V, but are less compact than the counterpart in MEC (Figure 1B). The columnar organization typical in MEC deep layers breaks down in LEC (Supplementary Figure S19B, C). Ventrally, deep layers diminish gradually toward its rostral and medial end, while layer III expands and contains increasing number of clustered NeuN-dense neurons in its deep portion, and layer II sublayers fuses in parallel (panels B and C in Figures 3, S11–S13). Medially, the LEC is progressively replaced by PAA (panels B and C in Figures S2, S3, S8–S11).

Chemoarchitectonic distinctions: Stains of CaBPs sharpen the MEC-LEC boundary. As detailed patterns will follow, here we outline the key differences. PV immunoreactivity is intense in MEC layers II–III but moderate to weak in LEC (Figure 3E). Conversely, CB labels numerous neurons and dense plexuses in LEC layers II–III, whereas MEC shows fewer CB+ cells and fibers, especially in layer III (Figure 3D, 4D). CR densely fills layer V in LEC, labeling both pyramids and plexuses, whereas MEC layer V exhibits restricted CR positivity confined largely to dorsolateral levels (Figure 3F, 4F). In addition, CR staining strongly labels the outermost thin portion of layer I, parallel to the pia surface of LEC at ventral levels; yet this labeling is absent in MEC (Figure 2F, 3F).

Validation of the MEC-LEC boundary by presubicular connectivity: Across rodent and primate species, presubicular projections selectively target MEC, avoiding LEC (Caballero-Bleda and Witter, 1993; Witter and Amaral, 2021). To validate the morphologically defined MEC-LEC border in the tree shrew brain, we injected mixed AAVs expressing eGFP (cell bodies) and tdTomato conjugated synaptophysin (fiber terminals) into dorsal or ventral presubiculum (PrS). Dorsal injections produced dense, laminarly restricted terminal fields in dorsal MEC. Fiber labeling peaked in layer III, with additional labeling in layer II concentrated at the I-II border (Figure 5A–E), matching rodent and monkey data (Caballero-Bleda and

Witter, 1993; Witter and Amaral, 2021). More ventral PrS injections resulted in terminal fields that shifted ventrally within MEC, always stopping sharply at the cytoarchitectonically defined MEC-LEC border. Ventral injections additionally labeled adjacent subiculum (Figure 5F–H), whose projections in rodents and primates target deep EC layers (Cappaert et al., 2015; Witter and Amaral, 2021). As expected, deep layers of both ventral MEC and LEC were highlighted, possibly by subicular terminals, whereas ventral PrS terminals remained restricted to superficial MEC layers and halted at the MEC-LEC boundary (Figure 5I–J). Thus, the hodological boundary defined by PrS projections coincides exactly with the cytoarchitectonically delineated MEC-LEC border in the tree shrew, consistent with other species (Kobro-Flatmoen and Witter, 2019; Witter et al., 2017).

Regional and laminar distribution of CaBP-selective neurons

Parvalbumin: PV is expressed in a subset of fast-spiking γ-aminobutyric acid-ergic (GABAergic) inhibitory interneurons in the brain (Kawaguchi et al., 1987). In rats, PV-ir interneurons constitute ~50 % of the entorhinal interneuron population (Miettinen et al., 1996; Wouterlood et al., 1995). Layer I of tree shrew EC lacks PV-ir somata, matching observations in rodents, but differing from the caudal primate EC, where small PV-ir neurons are present (Miettinen et al., 1996; Smaluhn et al., 2000; Tuñón et al., 1992; Uva et al., 2004; Wouterlood et al., 1995). Similar to rats, PV-ir somata are present in all cellular layers of the tree shrew EC, with a clear superficial > deep and MEC > LEC gradient (Figure 6A, B). In the MEC, dense PV-ir neuropil occupy layers II–III and ascend almost perpendicularly into layer I, whereas its deep layers show moderate immunoreactivity (Figure 6A). In the LEC, PV signals with moderate intensity are largely restricted to layers II and III (Figure 6B). Besides the laminar organization, the PV-immunoreactivity is also graded along the dorsoventral axis. In superficial layers of both MEC and LEC, neuropil density and soma number decline progressively with increasing distance from the rs (Figure 6C–H), mirroring observations in other species (Kobro-Flatmoen and Witter,

2019).

Calbindin: The CB-ir population in the EC comprises both excitatory pyramidal cells and inhibitory interneurons. In rats, the majority (> 80%) of CB-ir neurons are glutamatergic (Peterson et al., 1996). Pyramidal neurons are confined to superficial layers, whereas interneurons are distributed across all layers (Kobro-Flatmoen and Witter, 2019). The laminar pattern in tree shrews closely resembles that described in rats (Boccara et al., 2015). Layer I contains very few scattered CB-ir neurons (Figures S3D, S4D), similar to primates (Mikkonen et al., 1997; Suzuki and Porteros, 2002). In the MEC, layer II harbors a moderate density of irregularly arranged CB-ir neurons. A dorsal-to-ventral gradient increases CB-ir neuron density in layer II (Figure 3D). In addition, a small subset of CB-ir neurons form wart-like clusters (diameter: 158.423 ± 3.117 μm, n = 75), extending dendrites into layer I (Figure 7A–C), resembling but less frequent than the CB-ir clusters reported in rodents (Kitamura et al., 2014; Naumann et al., 2016; Ray et al., 2014). These clusters of smaller CB+ neurons are sparsely present (frequency: 12.5 ± 0.5 per animal) at both dorsal (Figures S17D) and ventral levels (Figures S20D) without difference (dorsal: 6.5 ± 0.6; ventral: 6.0 ± 0.3; paired *t*-test, t = 0.696, *P* = 0.518, n = 6 animals). Layer III is almost devoid of CB-ir somata, except for its most superficial portion, which contains irregularly distributed neurons, as in rodents (Boccara et al., 2015; Fujimaru and Kosaka, 1996). In LEC, layers IIb and III contain numerous CB-ir neurons, whereas layer IIa, is largely negative (Figure 7D, E). This layer is populated by large neurons that likely project to the dentate gyrus (DG) in line with data in rodents, bats and monkey (Jacobsen et al., 2023; Lee et al., 2021; Ohara et al., 2019; Ohara et al., 2021b) and in the tree shrew as we show below. Deep layers of EC contain only scattered CB-ir neurons without a mediolateral gradient. Neuropil labeling is dense in LEC (Figures 3D, 4D, 7A), but sparse in MEC, particularly in the deep portion of layer III, which is virtually label-free. Moderate fiber labeling is present in deep portion of layer I and layer V (Figure 7A), similar to rats and monkeys (Kobro-Flatmoen and Witter, 2019; Ohara et al., 2021b; Suzuki

and Porteros, 2002). The abrupt transition of CB-ir neuropil at the MEC-LEC border in layer III provides a reliable chemoarchitectonic landmark (Figure 4D).

Calretinin: The CR-ir population in the EC also comprises both excitatory and inhibitory neurons. Different from CB, the CR-ir excitatory neurons are confined to deep layers, whereas the interneurons, which comprise of one-fifth to a quarter of the entorhinal inhibitory neurons, are present in all cellular layers (Miettinen et al., 1997; Pothuizen et al., 2004). Layer I contains only occasional CR-ir neurons (Figures 8A, S9F), but displays a dense band of horizontally oriented CR-ir neuropil immediately beneath the pia surface in ventral LEC (Figures 3F, 8A, S9F), consistent with descriptions in rats, marmosets and humans (Miettinen et al., 1997; Mikkonen et al., 1997; Pothuizen et al., 2004; Seress et al., 1993; Wouterlood et al., 2000). This plexus reflects direct olfactory bulb (OB) input in rats (Wouterlood and Hrtig, 1995) and presumably also in tree shrews (Skeen and Hall, 1977). A dorsocaudal patch of LEC (16.25 ± 1.39%, n = 4 animals) lacks this plexus, comparable to—or slightly larger than—the gap described in rat (Price, 1973). Layers II and III contain scattered small CR-ir neurons whose processes run largely perpendicular to the pia surface (Figure 8B, C), closely resemble those bipolar GABA interneurons reported in rats and marmosets (Miettinen et al., 1997; Mikkonen et al., 1997; Pothuizen et al., 2004). Interestingly, these neurons do not express NeuN (Figure 8D). No medio-lateral gradient is evident for CR-ir somata in these layers, but neuropil labeling increases from MEC to LEC. While layers II and III of MEC appears nearly devoid of a CR-labeled plexus, the labeling in LEC is moderate and becomes dense in the ventromedial expansion of layer III (Figures 3F, S12F, S13F), as reported in rats and humans (Miettinen et al., 1997; Wouterlood et al., 2000). Layer V is distinguished by a dense population of medial-to-large CR-ir putative pyramidal neurons and their processes, most prominently in LEC. Labeling is strongest in dorsal LEC, and diminishes progressively away from this region (Figures S6F, S18F). Neuropil labeling in layer V parallels somatic density. Comparable patterns occur across species, although labeling intensity varies: layer V pyramidal neurons are lightly

stained in rats (Miettinen et al., 1997), moderately in tree shrews (Figure 8E, F) and marmosets (Pothuizen et al., 2004), but intensely labelled in humans (Mikkonen et al., 1997). Layer VI contains scattered CR-ir neurons, and neuropil labeling increases from MEC to LEC (Figures 3F, S16F), as in superficial layers. Distribution of CR-ir somata in layer VI is similar to rats and marmosets (Miettinen et al., 1997; Pothuizen et al., 2004), but different from humans, where a substantial population of CR-ir pyramidal neurons is present (Mikkonen et al., 1997).

Laminar organization of entorhinal projection neurons

Superficial layers: In both rodents and primates, layer II of the EC contains two distinct projection neuron populations, CB-expressing pyramidal neurons, and reelin-expressing stellate/fan cells in the medial/lateral subdivisions (Ohara et al., 2021b; Varga et al., 2010). Stellate and fan cells innervate the dentate gyrus and CA3/CA2 via the perforant path (Cappaert et al., 2015), whereas pyramidal cells target CA1, and a broad range of telencephalic structures (Ohara et al., 2019). In rodents, these two populations of neurons can also be distinguished by selective expressions of Single-minded homolog 1 (SIM1) and Wolfram syndrome 1 (WFS1), respectively (Kitamura et al., 2014; Lee et al., 2021). In the tree shrew, however, none of the commonly used reelin/SIM1/WFS1 antibodies tested yielded specific labeling (Supplementary Table S2).

To map hippocampal-projecting neurons in the superficial layers, we therefore injected the retrograde tracer CTB unilaterally into the dorsal hippocampus (Figures 9A, S22A). Retrogradely labeled somata were densely distributed in layers II and III of EC, and sparsely present in layer VI and WM (Figure 9B, S22B), confirming that the superficial layers provide the major entorhinal inputs to the hippocampus in tree shews, similar to other species (Jacobsen et al., 2023; Van Groen et al., 2003; Witter and Amaral, 1991). Although layer Va neurons have been reported to project to hippocampal CA1 in mice (Tsoi et al., 2022), we observed no such projection in

615 tree shrews, as evidenced by the absence of CTB labeling in layer V, similar to rats
616 (Ohara et al., 2019). Within MEC, the majority (> 80%) of retrogradely labeled layer
617 II somata were CB-negative; these cells were interspersed among scattered CB-ir
618 neurons without clear laminar organization and excluded from dense CB-ir clusters
619 (Figure 9C, S22B). In LEC, CTB-positive neurons and CB-ir neurons were largely
620 non-overlapping but confined to sublayers IIa and IIb, respectively (Figure 9D),
621 parallelling observations in other species (Kobro-Flatmoen and Witter, 2019; Ohara
622 et al., 2021b; Witter et al., 2017). The proportion of retrogradely labeled layer II
623 neurons co-expressing CB was significantly higher in MEC than in LEC (Figure 9E,
624 G), mirroring rodent findings that CB-expressing, hippocampus-projecting layer II
625 neurons reside primarily in MEC but rarely in LEC (Ohara et al., 2019). In layer III,
626 this trend was reversed (Figure 9F, H).

627

628 **Deep layers:** In both rodents and primates, layer V of the EC is conventionally
629 subdivided into layer Va and layer Vb. Deep Vb neurons are selectively innervated
630 by hippocampal outputs originating in CA1 and the subiculum, whereas superficial
631 Va neurons predominantly project to diverse cortical and subcortical targets (Ohara
632 et al., 2018; Ohara et al., 2021b; Sürmeli et al., 2015). In rats, Va appears as a loosely
633 arranged band of large neurons along the lamina dissecans, whereas Vb is a broader,
634 denser tier of smaller neurons (Boccara et al., 2015). In the tree shrew EC, co-
635 staining of CR/NeuN and retrogradely labeled somata by CTB injection into
636 laterodorsal thalamic nucleus confirms that the inner most, compact band of CR-
637 negative neurons belong to layer VI (Supplementary Figure S23) (Aggleton et al.,
638 1986), whereas the overlying, CR-positive band of neurons layer V. A thin, CR-
639 negative fringe of large neurons immediately beneath layer IV further hints at a
640 superficial (Vs) and deep (Vd) sub-division—Vs thick in MEC, Vd thick in LEC
641 (Figure 8E–F). To test whether this split mirrors Va/Vb in other species, we stained
642 for Etv1, a Va marker in mice (Sürmeli et al., 2015; Tsoi et al., 2022), and PCP4, a
643 robust Vb marker in both rodents and primates (Ohara et al., 2021a; Ohara et al.,

2018; Ohara et al., 2023; Ohara et al., 2021b). Etv1 yielded only diffuse, non-specific signal in layer V of both MEC and LEC (Supplementary Figure S24 A–C), contrasting sharply with the mouse-like pattern in adjacent subiculum (Sürmeli et al., 2015; Tsoi et al., 2022). PCP4, while faithfully outlining superficial layers as in rats and monkeys (Ohara et al., 2018; Ohara et al., 2021b), was evenly distributed across the entire depth of layer V (Supplementary Figure S24D–H), rather than being confined to a Vb-equivalent sublayer. The absence of specific Etv1 and the uniform PCP4 expression in layer V therefore argue against a rodent-like Va/Vb partition in tree shrews.

To resolve this chemoarchitectonic ambiguity in layer V, we first injected AAV1-hSyn-Cre unilaterally into dorsal CA1/subiculum to anterogradely and transsynaptically label EC neurons receiving hippocampal projections (Zingg et al., 2017; Zingg et al., 2022; Zingg et al., 2020). Cre-ir somata formed a dense band throughout MEC layer V, with only sparse labelling in superficial MEC and LEC (Figure 10A–C), aligning with the established preference of hippocampal back-projections for deep EC layers (Ohara et al., 2018; Sürmeli et al., 2015). The absence of retrograde transport is verified by the lack of layer-V-to-CA1 projections in tree shrews (Supplementary Figure S25). Within MEC, Cre+ neurons occupied the full superficial-to-deep extent of layer V (Figure 10D) and overlapped minimally with sparse CR-ir neurons. In LEC, the fewer Cre-labeled neurons were scattered throughout layer V yet frequently co-localized with CR-ir neurons (Figure 10E–I). These distribution and colocalization patterns indicate that hippocampal innervation of layer V aligns with PCP4 rather than CR expression.

To further test for sublamination, we injected CTB into the retrosplenial cortex, nucleus accumbens and amygdala, which are established layer-Va targets in rodents and primates (Ohara et al., 2018; Ohara et al., 2021b; Sürmeli et al., 2015), to retrogradely label telencephalic-output neurons in EC layer V (Figure 11). CTB+ somata were confined to layer V, with only few neurons into layer VI, confirming that the principal output neurons reside in layer V, as in other species (Munoz and

673 Insausti, 2005). Within layer V, CTB+ neurons are sparse and evenly scattered
674 across the entire depth of layer V in both MEC and LEC at dorsal and ventral levels,
675 revealing no Va/Vb stratification (Figure 11B–D, I–K, P–R), in line with recent
676 monkey data (Ohara et al., 2021b; Witter and Amaral, 2021). As seen with
677 anterograde transsynaptic tracing, CTB-labeled cells preferentially colocalized with
678 CR in LEC (Figure 11 L–N, S–U), but not in MEC (Figure 11E–G). Thus, retrograde
679 tracing corroborates that CR-defined sublayers fail to align with connectional
680 identity and that tree-shrew layer V lacks overt laminar organization.

681 Finally, we performed a dual tracing experiment: AAV-Cre was injected into CA1
682 to label hippocampal-recipient neurons in MEC layer V, and CTB was delivered
683 into secondary visual cortex (V2) to tag telencephalic-projecting neurons in the
684 same animal (Lu et al., 2022). Cre expression was restricted to CA1 and subiculum,
685 while CTB was confined to deep layers at the V2/temporal-cortex boundary (Figure
686 12A). Both labeled populations, though sparse, occupied the entire depth of MEC
687 layer V without stratification (Figure 12B), and intermingled with partial overlap
688 (Figure 12C), revealing only loose segregation—markedly different from the clear
689 Va/Vb split observed in rodents (Ohara et al., 2018; Sürmeli et al., 2015).

690

691 ## Discussion

692 Here we deliver the first comprehensive cyto- and chemoarchitectonic map of the tree
693 shrew (*Tupaia belangeri chinensis*) EC, parcel it into medial and lateral subdivisions,
694 and define the laminar origin and termination of its hippocampal and telencephalic
695 projections. The resulting atlas provides an essential, detailed anatomical reference for
696 future structural, functional and translational studies in this emerging model species,
697 and substantially extends a previous description in *Tupaia glis* (Skeen and Hall, 1977).

698 **Translating tree shrew entorhinal architecture into early-stage AD models**

699 Neurofibrillary pathology first emerges in the EC (Igarashi, 2023; Kobro-Flatmoen et

al., 2021; Setti and Reed, 2022). Although the tree shrew hippocampus was characterized over two decades ago (Keuker et al., 2003), the EC remained uncharted, restricting previous AD modeling to the hippocampus (Lin et al., 2016; Wang et al., 2020b) and preventing examination of the earliest entorhinal changes that initiate cognitive decline (Li et al., 2023; Li et al., 2024b). Our cyto- and chemoarchitectonic atlas, combined with connectional validation, now closes this gap. Precisely delineated MEC and LEC borders, and laminar map of afferent and efferent neurons provide stereotaxic coordinates for targeted delivery of human AD-derived tau and/or Aβ oligomers, ensuring that experimentally induced pathology begins in the same layers where spontaneous tangles first arise. Merging this anatomical framework with the species' natural age-related pathology (Li et al., 2024b) will allow researchers to model the earliest EC-to-hippocampus transsynaptic propagation cascade in a cost-effective, ethically favorable manner that bridges mechanistic rodent work and primate validation. This advance is expected to accelerate pre-clinical screening of therapies aimed at interrupting AD before cortical memory networks collapse.

Subdivisions of the entorhinal cortex

The EC has traditionally been divided into two cytoarchitectonically defined subfields (Brodmann, 1909), but over the years more complex division-schemes have been proposed. In rodents this has resulted in five or six cytoarchitectonic subfields (Insausti et al., 1997; Uva et al., 2004; Van Groen, 2001), based on cytoarchitectonic differentiations. In primates, increased regional and laminar complexity has expanded the partition to seven or eight areas (Amaral et al., 1987; De Gois Morais et al., 2020; Insausti et al., 1995; Piguet et al., 2018). Although architectural parcellation scheme provides reliable anatomical landmarks in the EC (Witter et al., 2017), it offers no direct insight into function and does not translate into an obvious evolutionary sequence—e.g., which rodent EC subfield corresponds to which primate counterpart.

An alternative is to return to the simple division of the EC into medial (MEC) and lateral

(LEC) sectors on the basis of connectivity with the hippocampal and parahippocampal structures (Canto et al., 2008; Jacobsen et al., 2023; Kerr et al., 2007; Suzuki and Amaral, 1994; Witter, 2006;2007; Witter and Amaral, 1991;2021). This connection-based scheme is increasingly adopted because it links structure to function and aligns subregions across species regardless of morphology or topographic position in the brain. In rodents, medial and lateral subdivisions of EC harbor distinct functional cell types that differentially support spatial navigation and episodic memory (Knierim et al., 2014; Nilssen et al., 2019; Rowland et al., 2016; Sugar and Moser, 2019; Wang et al., 2020a). Human functional connectivity magnetic resonance imaging likewise reveals a parallel posteromedial-anterolateral partition sensitive to spatial versus non-spatial information that aligns with the MEC/LEC dichotomy observed in non-human species (Maass et al., 2015; Navarro Schroder et al., 2015; Syversen et al., 2024; Syversen et al., 2021; Yeung et al., 2017). Guided by this conserved bipartite organization (Cappaert et al., 2015; Kobro-Flatmoen and Witter, 2019; Witter et al., 2017), we deliberately restricted our three shrew parcellation to medial and lateral portions, verified by chemoarchitecture and connectivity, and avoided additional subfields whose homology would be ambiguous.

Conservation and divergence of entorhinal lamination from rodents to primates

Across mammals, the EC retains six cytoarchitectonic layers (Boccara et al., 2015; Kobro-Flatmoen and Witter, 2019; Ohara et al., 2018; Ohara et al., 2021b), and consistent expression of the three major CaBPs (Hof et al., 1999). Yet, within this conserved framework, species-specific specializations are evident, in both superficial and deep layers. The tree shrew EC is size-comparable to the rat EC, yet it exhibits an intermediate phenotype between rodents and primates.

Olfactory input in layer I: The OB projects directly to EC, but the target territory differs sharply: in rats it covers almost the entire LEC surface except a narrow dorsal strip (Price, 1973), whereas in macaques it is restricted to the anterior “olfactory field”

of LEC (Carmichael et al., 1994; Insausti et al., 2002; Turner et al., 1978). CR-ir neuropil in layer I is a reliable proxy for OB input in rats, as CR signals colocalize with OB fibers, and disappear after OB lesions (Wouterlood and Hrtig, 1995). In tree shrews, OB fibers have been reported to innervate most, if not all, of the LEC (Skeen and Hall, 1977). We find three lines of evidence that the same CR-neuropil relationship applies in *Tupaia belangeri chinensis*: (i) OB fibers and CR-labelling (Supplementary Figure S13F) both run immediately beneath the pia in PIR and LEC; (ii) the rostro-caudal decline in OB fiber density matches the rostro-caudal decline in CR intensity in layer Ia (Supplementary Figure S13F); (iii) PER and MEC, which lack OB input (Price, 1973; Skeen and Hall, 1977), are virtually CR-negative in layer I (Figures 2F). In the current study, we found that the dorsocaudal 16.25 % of tree shrew LEC lacks CR-ir neuropil (Figures 4F, S6F), indicating an OB-recipient territory smaller than in rats but far larger than in macaques, an intermediate condition expected from the species' phylogenetic position.

Organization of CB-ir neurons in layer II: In mice and to a somewhat lesser extent in rats, layer II pyramidal neurons in MEC are aggregated into arrays of densely packed CB-ir clusters, alternating with the reelin expressing larger stellate neurons that project to DG, CA2 and CA3 (Kitamura et al., 2014; Naumann et al., 2016; Ray et al., 2014). In contrast, monkey MEC layer II lacks such clusters; instead, it is largely stratified into a superficial tier (IIa) of stellate neurons and a deeper tier (IIb) enriched in CB-ir pyramidal neurons (Ohara et al., 2021b; Suzuki and Porteros, 2002). In the tree shrew MEC layer II, only scattered CB-ir clusters are present (Figure 7A–C), comparable in size to those in rats (158 μm vs 145 μm) (Naumann et al., 2016). The majority of CB-ir neurons are dispersed among hippocampus-projecting cells in a "salt-and-pepper" distribution (Figure 9). This intermediate distribution pattern of stellate and pyramidal neurons in tree shrew MEC layer II suggests a transitional architecture between rodents and monkeys in the organization of EC.

Stratification of deep layers: CR staining reveals that layer V pyramidal neurons are lightly labeled in rats (Miettinen et al., 1997) but intensely stained in humans

(Mikkonen et al., 1997); Tree shrews (Figure 8) and marmosets (Pothuizen et al., 2004) exhibit intermediate labeling intensities. More importantly, CR-defined sub-laminae in tree shrew layer V do not segregate hippocampal-recipient from telencephalic-output neurons (Figures 10, 11). The two populations intermingle (Figure 12) as in the monkey LEC, unlike the clearer Va/Vb segregation seen in rodents (Ohara et al., 2018; Ohara et al., 2021b; Sürmeli et al., 2015). A similar intermediate phenotype is seen in layer VI. In rodents this layer is thin, poorly differentiated, and merges imperceptibly with layer V (Boccara et al., 2015; Insausti et al., 1997), whereas in primates it is thick, subdivided into several distinct sub-laminae and sharply demarcated from layer V (Amaral et al., 1987; De Gois Morais et al., 2020; Ohara et al., 2021b; Piguet et al., 2018). Tree shrew layer VI is clearly separated from layer V yet lacks further internal stratification (Figure 1B), again occupying the intermediate position. Collectively, these features reveal a cytoarchitecture intermediate between rodent and primate patterns, mirroring the phylogenetic position of tree shrews as a close outgroup to primates (Fan et al., 2013; Fan et al., 2019; Xu et al., 2012; Ye et al., 2021).

Changes in MEC organization may have functional consequences

The entorhinal-hippocampal system is indispensable for episodic memory, binding personally experienced events to specific spatial contexts (Tulving, 2002). Highly processed sensory and mnemonic signals reach the hippocampus via the superficial layers (II&III) of EC, which integrate multimodal input from widespread cortical and subcortical structures (Canto et al., 2008; Nilssen et al., 2025; Vandrey et al., 2020; Witter et al., 2017). This feed-forward pathway is continuously sculpted by feedback signals from the hippocampus, targeting the deep layers (V&VI) of EC (Ohara et al., 2018; Sürmeli et al., 2015). The deep layers, in turn, generate diffuse projections to superficial EC layers (Witter and Amaral, 2021; Witter et al., 2017), thereby closing a recurrent circuit that can gate the gain, timing, and routing of various signals before they ever reach the hippocampus (Tukker et al., 2022).

Within the MEC, the rodent brain deploys a constellation of specialized cell types, including grid cells (Hafting et al., 2005; Ouchi and Fujisawa, 2024), aperiodic spatial cells (Fyhn et al., 2004), head direction cells (Sargolini et al., 2006), border cells (Solstad et al., 2008), object-vector cells (Hoydal et al., 2019), and neurons representing various self-motion signals (Kropff et al., 2015; Mallory et al., 2021). These cells collectively translate landmark-based cues into a metric representation of space (Long and Lu, 2022; Moser et al., 2017). The hippocampus integrates these inputs to generate place-cell maps that serve as the scaffold for episodic memory (Duan et al., 2025; Sugar and Moser, 2019), and in the meanwhile sends feedback to MEC deep layers to maintain the excitability of the network (Bonnevie et al., 2013).

Yet species comparisons reveal striking variations in how this scaffold is built. In freely moving monkeys, although hippocampal place-related activity has been reported across various navigational tasks (Courellis et al., 2019; Hazama and Tamura, 2019; Ludvig et al., 2004), hippocampal neurons seldom exhibit the pure, single-variable place tuning seen in rodents; instead, they multiplex position with head direction, spatial view, facing location and/or other spatial variables (Mao et al., 2021; Piza et al., 2024). Our preliminary recordings from tree shrews reveal a graded transition: hippocampal neurons exhibit stronger spatial tuning than monkeys but more frequent multiplexed selectivity than rats, hinting at an evolutionary continuum from rodents to primates.

This transitional phenotype raises a mechanistic question: does it emerge from gradual re-wiring within MEC superficial layers gating cortical information into the hippocampus, or from maturation of deep-layer feedback loops that sculpt superficial-layer computations before signals reach the hippocampus (Cappaert et al., 2015; Witter et al., 2017)? A subtle shift in the stellate-pyramidal balance within layer II/III could potentially alter the integration of cortical information and eventually reshape the hippocampal spatial codes. Conversely, an expansion or specialization of hippocampal feedback to deep layers might recursively refine superficial-layer computations (Tukker et al., 2022). However, critical evidence is lacking. Definitive answers will require comparative studies that pair immunofluorescence and viral tracing with

multicell patch-clamp recordings and opto- or chemogenetic perturbations of the EC microcircuit across rodents, tree shrews, and monkeys, to dissect the anatomical and functional links among layers and cell types. Such work promises not only to clarify how entorhinal microcircuits evolve, but also to explain why and how spatial codes are differently represented in rodents and primates.

Acknowledgements

We would like to thank the Institutional Center for Shared Technologies and Facilities of Kunming Institute of Zoology, Chinese Academy of Sciences for providing us with Tissue FAXS Cytometry. And we are grateful to Guo-Lan Ma for her technical support. The authors also express their gratitude to the staff members of the National Research Facility for Phenotypic & Genetic Analysis of Model Animals (Primate Facility) (https://cstr.cn/31137.02.NPRC), for providing technical support and assistance in data collection and analysis.

Supplementary Data

Supplementary data to this article can be found online.

Competing Interests

The authors declare no competing financial interests.

Author Contributions

L.L. and M.P.W. conceived and designed the study. Y.F.Y., C.D., X.F.G., R.Z. and C.J.L. performed the tracing experiments. R.Z. and J.L.L. validated the antibodies. J.X.J. and H.Y.Y. collected the image data. Y.F.Y., J.L.L. and L.L. analyzed the data and made the figures. L.L., X.C. and M.P.W. wrote the manuscript. All authors contributed to reviewing and editing the manuscript.

References

Aggleton JP, Desimone R, Mishkin M. 1986. The origin, course, and termination of the hippocampothalamic projections in the macaque. *The Journal of Comparative Neurology*, **243**(3): 409–421.

Alexandra Lopes P & Guil-Guerrero JL. 2025. Beyond Transgenic Mice: Emerging Models and Translational Strategies in Alzheimer's Disease. *International Journal of Molecular Sciences*, **26**(12): 5541.

Amaral DG, Insausti R, Cowan WM. 1987. The entorhinal cortex of the monkey: I. Cytoarchitectonic organization. *The Journal of Comparative Neurology*, **264**(3): 326–355.

Arnold SE, Hyman BT, Flory J, et al. 1991. The topographical and neuroanatomical distribution of neurofibrillary tangles and neuritic plaques in the cerebral cortex of patients with Alzheimer's disease. *Cerebral Cortex*, **1**(1): 103–116.

Barinka F, Salaj M, Rybář J, et al. 2012. Calretinin, parvalbumin and calbindin immunoreactive interneurons in perirhinal cortex and temporal area Te3V of the rat brain: qualitative and quantitative analyses. *Brain Research*, **1436**: 68–80.

Beaudin SA, Singh T, Agster KL, et al. 2013. Borders and comparative cytoarchitecture of the perirhinal and postrhinal cortices in an F1 hybrid mouse. *Cerebral Cortex*, **23**(2): 460–476.

Boccara CN, Kjonigsen LJ, Hammer IM, et al. 2015. A three-plane architectonic atlas of the rat hippocampal region. *Hippocampus*, **25**(7): 838–857.

Bonnevie T, Dunn B, Fyhn M, et al. 2013. Grid cells require excitatory drive from the

hippocampus. *Nature Neuroscience*, **16**(3): 309–317.

Braak H & Braak E. 1991. Neuropathological stageing of Alzheimer-related changes. *Acta neuropathologica*, **82**(4): 239–259.

Brodmann K. 1909. Vergleichende Lokalisationslehre der Grosshirnrinde in ihren Prinzipien dargestellt auf Grund des Zellenbaues. Lepzig: J.A. Barth.

Burwell RD. 2001. Borders and cytoarchitecture of the perirhinal and postrhinal cortices in the rat. *The Journal of Comparative Neurology*, **437**(1): 17–41.

Caballero-Bleda M & Witter MP. 1993. Regional and laminar organization of projections from the presubiculum and parasubiculum to the entorhinal cortex: an anterograde tracing study in the rat. *The Journal of Comparative Neurology*, **328**(1): 115–129.

Canto CB, Wouterlood FG, Witter MP. 2008. What does the anatomical organization of the entorhinal cortex tell us? *Neural Plasticity*, **2008**: 381243.

Cappaert NL, Van Strien NM, Witter MP. 2015. Hippocampal Formation. *In*: Paxinos G. The Rat Nervous System. Academic Press, 511–573.

Carmichael ST, Clugnet MC, Price JL. 1994. Central olfactory connections in the macaque monkey. *The Journal of Comparative Neurology*, **346**(3): 403–434.

Casanova MF. 2010. The role of the entorhinal cortex in paraphrenia. *Current Psychiatry Reports*, **12**(3): 202–207.

Coughlan G, Laczo J, Hort J, et al. 2018. Spatial navigation deficits - overlooked cognitive marker for preclinical Alzheimer disease? *Nature Reviews Neurology*, **14**(8): 496–506.

911 Courellis HS, Nummela SU, Metke M, et al. 2019. Spatial encoding in primate
912 hippocampus during free navigation. *PLoS Biology*, **17**(12): e3000546.
913 De Calignon A, Polydoro M, Suárez-Calvet M, et al. 2012. Propagation of tau pathology
914 in a model of early Alzheimer's disease. *Neuron*, **73**(4): 685–697.
915 De Gois Morais PLA, De Lima RRM, Rios-Florez JA, et al. 2020. Cytoarchitecture and
916 myeloarchitecture of the entorhinal cortex of the common marmoset monkey (*Callithrix*
917 *jacchus*). *The Journal of Comparative Neurology*, **528**(8): 1307–1320.
918 Duan YL, Hu SY, Ge XF, et al. 2025. Object-translocation induces event coding in the
919 rat hippocampus. *Communications Biology*, **8**(1): 797.
920 Eichenbaum H. 2017. On the Integration of Space, Time, and Memory. *Neuron*, **95**(5):
921 1007–1018.
922 Fan Y, Huang ZY, Cao CC, et al. 2013. Genome of the Chinese tree shrew. *Nature*
923 *Communication*, **4**: 1426.
924 Fan Y, Luo R, Su LY, et al. 2018. Does the genetic feature of the Chinese tree shrew
925 (*Tupaia belangeri chinensis*) support Its potential as a viable model for Alzheimer's
926 disease research? *Journal of Alzheimer's Disease : JAD*, **61**(3): 1015–1028.
927 Fan Y, Ye MS, Zhang JY, et al. 2019. Chromosomal level assembly and population
928 sequencing of the Chinese tree shrew genome. *Zoological Research*, **40**(6): 506–521.
929 Fu H, Rodriguez GA, Herman M, et al. 2017. Tau Pathology Induces Excitatory Neuron
930 Loss, Grid Cell Dysfunction, and Spatial Memory Deficits Reminiscent of Early
931 Alzheimer's Disease. *Neuron*, **93**(3): 533–541 e535.
932 Fujimaru Y & Kosaka T. 1996. The distribution of two calcium binding proteins,

933 calbindin D-28K and parvalbumin, in the entorhinal cortex of the adult mouse.
934 *Neuroscience Research*, **24**(4): 329–343.
935 Fyhn M, Molden S, Witter MP, et al. 2004. Spatial representation in the entorhinal
936 cortex. *Science*, **305**(5688): 1258–1264.
937 Gatome CW, Slomianka L, Mwangi DK, et al. 2010. The entorhinal cortex of the
938 Megachiroptera: a comparative study of Wahlberg's epauletted fruit bat and the straw-
939 coloured fruit bat. *Brain Structure & Function*, **214**(4): 375–393.
940 Hafting T, Fyhn M, Molden S, et al. 2005. Microstructure of a spatial map in the
941 entorhinal cortex. *Nature*, **436**(7052): 801–806.
942 Hazama Y & Tamura R. 2019. Effects of self-locomotion on the activity of place cells
943 in the hippocampus of a freely behaving monkey. *Neuroscience Letters*, **701**: 32–37.
944 Hof PR, Glezer, Ii, Condé F, et al. 1999. Cellular distribution of the calcium-binding
945 proteins parvalbumin, calbindin, and calretinin in the neocortex of mammals:
946 phylogenetic and developmental patterns. *Journal of Chemical Neuroanatomy*, **16**(2):
947 77–116.
948 Hoydal OA, Skytoen ER, Andersson SO, et al. 2019. Object-vector coding in the medial
949 entorhinal cortex. *Nature*, **568**(7752): 400–404.
950 Igarashi KM. 2023. Entorhinal cortex dysfunction in Alzheimer's disease. *Trends in*
951 *Neurosciences*, **46**(2): 124–136.
952 Insausti R, Amaral DG, Cowan WM. 1987a. The entorhinal cortex of the monkey: II.
953 Cortical afferents. *The Journal of Comparative Neurology*, **264**(3): 356–395.
954 Insausti R, Amaral DG, Cowan WM. 1987b. The entorhinal cortex of the monkey: III.

955 Subcortical afferents. *The Journal of Comparative Neurology*, **264**(3): 396–408.
956 Insausti R, Herrero MT, Witter MP. 1997. Entorhinal cortex of the rat: cytoarchitectonic
957 subdivisions and the origin and distribution of cortical efferents. *Hippocampus*, **7**(2):
958 146–183.
959 Insausti R, Marcos P, Arroyo-Jiménez MM, et al. 2002. Comparative aspects of the
960 olfactory portion of the entorhinal cortex and its projection to the hippocampus in
961 rodents, nonhuman primates, and the human brain. *Brain Research Bulletin* **57**(3-4):
962 557–560.
963 Insausti R, Muñoz-López M, Insausti AM, et al. 2017. The Human Periallocortex: Layer
964 Pattern in Presubiculum, Parasubiculum and Entorhinal Cortex. A Review. *Frontiers in*
965 *Neuroanatomy*, **11**: 84.
966 Insausti R, Tuñón T, Sobreviela T, et al. 1995. The human entorhinal cortex: a
967 cytoarchitectonic analysis. *The Journal of Comparative Neurology*, **355**(2): 171–198.
968 Jacobsen B, Kleven H, Gatome W, et al. 2023. Organization of projections from the
969 entorhinal cortex to the hippocampal formation of the Egyptian fruit bat *Rousettus*
970 *aegyptiacus*. *Hippocampus*, **33**(8): 889–905.
971 Jun H, Bramian A, Soma S, et al. 2020. Disrupted Place Cell Remapping and Impaired
972 Grid Cells in a Knockin Model of Alzheimer's Disease. *Neuron*, **107**(6): 1095–1112
973 e1096.
974 Karimani F, Asgari Taei A, Abolghasemi-Dehaghani MR, et al. 2024. Impairment of
975 entorhinal cortex network activity in Alzheimer's disease. *Frontiers in Aging*
976 *Neuroscience*, **16**: 1402573.

977 Kawaguchi Y, Katsumaru H, Kosaka T, et al. 1987. Fast spiking cells in rat
978 hippocampus (CA1 region) contain the calcium-binding protein parvalbumin. *Brain*
979 *Research*, **416**(2): 369–374.
980 Kerr KM, Agster KL, Furtak SC, et al. 2007. Functional neuroanatomy of the
981 parahippocampal region: the lateral and medial entorhinal areas. *Hippocampus*, **17**(9):
982 697–708.
983 Keuker JI, Rochford CD, Witter MP, et al. 2003. A cytoarchitectonic study of the
984 hippocampal formation of the tree shrew (*Tupaia belangeri*). *Journal of Chemical*
985 *Neuroanatomy*, **26**(1): 1–15.
986 Kitamura T, Pignatelli M, Suh J, et al. 2014. Island cells control temporal association
987 memory. *Science*, **343**(6173): 896–901.
988 Knierim JJ, Neunuebel JP, Deshmukh SS. 2014. Functional correlates of the lateral
989 and medial entorhinal cortex: objects, path integration and local-global reference
990 frames. *Philosophical transactions of the Royal Society of London. Series B, Biological*
991 *sciences*, **369**(1635): 20130369.
992 Kobro-Flatmoen A, Lagartos-Donate MJ, Aman Y, et al. 2021. Re-emphasizing early
993 Alzheimer's disease pathology starting in select entorhinal neurons, with a special
994 focus on mitophagy. *Ageing Research Reviews*, **67**: 101307.
995 Kobro-Flatmoen A & Witter MP. 2019. Neuronal chemo-architecture of the entorhinal
996 cortex: A comparative review. *The European Journal of Neuroscience* **50**(10): 3627–
997 3662.
998 Kropff E, Carmichael JE, Moser MB, et al. 2015. Speed cells in the medial entorhinal

cortex. *Nature*, **523**(7561): 419–424.

Kulason S, Tward DJ, Brown T, et al. 2019. Cortical thickness atrophy in the transentorhinal cortex in mild cognitive impairment. *NeuroImage. Clinical*, **21**: 101617.

Kulason S, Xu E, Tward DJ, et al. 2020. Entorhinal and Transentorhinal Atrophy in Preclinical Alzheimer's Disease. *Frontiers in Neuroscience*, **14**: 804.

Lee JY, Jun H, Soma S, et al. 2021. Dopamine facilitates associative memory encoding in the entorhinal cortex. *Nature*, **598**(7880): 321–326.

Li CJ, Hui YQ, Zhang R, et al. 2023. A comparison of behavioral paradigms assessing spatial memory in tree shrews. *Cerebral Cortex*, **33**(19): 10303–10321.

Li H, Mei L, Nie X, et al. 2024a. The Tree Shrew Model of Parkinson Disease: A Cost-Effective Alternative to Nonhuman Primate Models. *Laboratory Investigation; A Journal of Technical Methods and Pathology*, **104**(11): 102145.

Li H, Xiang BL, Li X, et al. 2024b. Cognitive Deficits and Alzheimer's Disease-Like Pathologies in the Aged Chinese Tree Shrew. *Molecular Neurobiology*, **61**(4): 1892–1906.

Li K, Qian L, Zhang C, et al. 2025. The entorhinal cortex and cognitive impairment in schizophrenia: A comprehensive review. *Progress in Neuro-psychopharmacology & Biological Psychiatry*, **136**: 111218.

Lin N, Xiong LL, Zhang RP, et al. 2016. Injection of Abeta1-40 into hippocampus induced cognitive lesion associated with neuronal apoptosis and multiple gene expressions in the tree shrew. *Apoptosis : An International Journal on Programmed Cell Death*, **21**(5): 621–640.

Long JL & Lu L. 2022. Dynamic coding in the hippocampus during navigation. *Zoological Research*, **43**(6): 1023–1025.

Lu J, Zhang Z, Yin X, et al. 2022. An entorhinal-visual cortical circuit regulates depression-like behaviors. *Molecular Psychiatry*, **27**(9): 3807–3820.

Ludvig N, Tang HM, Gohil BC, et al. 2004. Detecting location-specific neuronal firing rate increases in the hippocampus of freely-moving monkeys. *Brain Research*, **1014**(1-2): 97–109.

Maass A, Berron D, Libby LA, et al. 2015. Functional subregions of the human entorhinal cortex. *Elife*, **4**.

Mallory CS, Hardcastle K, Campbell MG, et al. 2021. Mouse entorhinal cortex encodes a diverse repertoire of self-motion signals. *Nature Communication*, **12**(1): 671.

Mao D, Avila E, Caziot B, et al. 2021. Spatial modulation of hippocampal activity in freely moving macaques. *Neuron*, **109**(21): 3521–3534 e3526.

Miettinen M, Koivisto E, Riekkinen P, et al. 1996. Coexistence of parvalbumin and GABA in nonpyramidal neurons of the rat entorhinal cortex. *Brain Research*, **706**(1): 113–122.

Miettinen M, Pitkänen A, Miettinen R. 1997. Distribution of calretinin-immunoreactivity in the rat entorhinal cortex: coexistence with GABA. *The Journal of Comparative Neurology*, **378**(3): 363–378.

Mikkonen M, Soininen H, Pitkänen A. 1997. Distribution of parvalbumin-, calretinin-, and calbindin-D28k-immunoreactive neurons and fibers in the human entorhinal cortex. *The Journal of Comparative Neurology*, **388**(1): 64–88.

1043 Moser EI, Moser MB, Mcnaughton BL. 2017. Spatial representation in the hippocampal
1044 formation: a history. *Nature Neuroscience*, **20**(11): 1448–1464.
1045 Munoz M & Insausti R. 2005. Cortical efferents of the entorhinal cortex and the
1046 adjacent parahippocampal region in the monkey (*Macaca fascicularis*). *The European*
1047 *journal of neuroscience*, **22**(6): 1368–1388.
1048 Naumann RK, Ray S, Prokop S, et al. 2016. Conserved size and periodicity of
1049 pyramidal patches in layer 2 of medial/caudal entorhinal cortex. *The Journal of*
1050 *Comparative Neurology*, **524**(4): 783–806.
1051 Navarro Schroder T, Haak KV, Zaragoza Jimenez NI, et al. 2015. Functional
1052 topography of the human entorhinal cortex. *Elife*, **4**.
1053 Nilssen ES, Doan TP, Nigro MJ, et al. 2019. Neurons and networks in the entorhinal
1054 cortex: A reappraisal of the lateral and medial entorhinal subdivisions mediating
1055 parallel cortical pathways. *Hippocampus*, **29**(12): 1238–1254.
1056 Nilssen ES, Jacobsen B, Doan TP, et al. 2025. Long-range inhibitory axons from
1057 medial entorhinal cortex target lateral entorhinal neurons projecting to the hippocampal
1058 formation. eLife Sciences Publications, Ltd.
1059 O'keefe J. 1976. Place units in the hippocampus of the freely moving rat. *Experimental*
1060 *Neurology*, **51**(1): 78–109.
1061 O'keefe J, Burgess N, Donnett JG, et al. 1998. Place cells, navigational accuracy, and
1062 the human hippocampus. *Philosophical Transactions of the Royal Society of London.*
1063 *Series B, Biological Sciences*, **353**(1373): 1333–1340.
1064 Ohara S, Blankvoort S, Nair RR, et al. 2021a. Local projections of layer Vb-to-Va are

more prominent in lateral than in medial entorhinal cortex. *Elife*, **10**: e67262.

Ohara S, Gianatti M, Itou K, et al. 2019. Entorhinal Layer II Calbindin-Expressing Neurons Originate Widespread Telencephalic and Intrinsic Projections. *Frontiers in Systems Neuroscience*, **13**: 54.

Ohara S, Onodera M, Simonsen Ø W, et al. 2018. Intrinsic Projections of Layer Vb Neurons to Layers Va, III, and II in the Lateral and Medial Entorhinal Cortex of the Rat. *Cell Reports*, **24**(1): 107–116.

Ohara S, Rannap M, Tsutsui KI, et al. 2023. Hippocampal-medial entorhinal circuit is differently organized along the dorsoventral axis in rodents. *Cell Reports*, **42**(1): 112001.

Ohara S, Yoshino R, Kimura K, et al. 2021b. Laminar Organization of the Entorhinal Cortex in Macaque Monkeys Based on Cell-Type-Specific Markers and Connectivity. *Frontiers in Neural Circuits*, **15**: 790116.

Olajide OJ, Suvanto ME, Chapman CA. 2021. Molecular mechanisms of neurodegeneration in the entorhinal cortex that underlie its selective vulnerability during the pathogenesis of Alzheimer's disease. *Biology Open*, **10**(1).

Ouchi A & Fujisawa S. 2024. Predictive grid coding in the medial entorhinal cortex. *Science*, **385**(6710): 776–784.

Paspalas CD, Carlyle BC, Leslie S, et al. 2018. The aged rhesus macaque manifests Braak stage III/IV Alzheimer's-like pathology. *Alzheimer's & Dementia : the Journal of the Alzheimer's Association*, **14**(5): 680–691.

Pawlik M, Fuchs E, Walker LC, et al. 1999. Primate-like amyloid-beta sequence but no

cerebral amyloidosis in aged tree shrews. *Neurobiology of Aging*, **20**(1): 47–51.

Peterson DA, Lucidi-Phillipi CA, Murphy DP, et al. 1996. Fibroblast growth factor-2 protects entorhinal layer II glutamatergic neurons from axotomy-induced death. *The Journal of Neuroscience : the Official Journal of the Society for Neuroscience*, **16**(3): 886–898.

Pickett EK, Henstridge CM, Allison E, et al. 2017. Spread of tau down neural circuits precedes synapse and neuronal loss in the rTgTauEC mouse model of early Alzheimer's disease. *Synapse*, **71**(6).

Pignataro A & Middei S. 2017. Trans-Synaptic Spread of Amyloid-β in Alzheimer's Disease: Paths to β-Amyloidosis. *Neural Plasticity*, **2017**: 5281829.

Piguet O, Chareyron LJ, Banta Lavenex P, et al. 2018. Stereological analysis of the rhesus monkey entorhinal cortex. *The Journal of Comparative Neurology*, **526**(13): 2115–2132.

Piza DB, Corrigan BW, Gulli RA, et al. 2024. Primacy of vision shapes behavioral strategies and neural substrates of spatial navigation in marmoset hippocampus. *Nature Communication*, **15**(1): 4053.

Pothuizen HH, Feldon J, Jongen-Relo AL. 2004. Co-expression of calretinin and gamma-aminobutyric acid in neurons of the entorhinal cortex of the common marmoset monkey. *Hippocampus*, **14**(5): 615–627.

Price JL. 1973. An autoradiographic study of complementary laminar patterns of termination of afferent fibers to the olfactory cortex. *The Journal of Comparative Neurology*, **150**(1): 87–108.

1109 Ramón Y Cajal S. 1902. Sobre un ganglio especial de la corteza esfeno-occipital. *Trab*
1110 *del Lab de Invest Biol Univ Madrid*, **1**: 189–206.
1111 Ray S & Brecht M. 2016. Structural development and dorsoventral maturation of the
1112 medial entorhinal cortex. *Elife*, **5**: e13343.
1113 Ray S, Naumann R, Burgalossi A, et al. 2014. Grid-layout and theta-modulation of
1114 layer 2 pyramidal neurons in medial entorhinal cortex. *Science*, **343**(6173): 891–896.
1115 Rowland DC, Roudi Y, Moser MB, et al. 2016. Ten Years of Grid Cells. *Annual Review*
1116 *of Neuroscience*, **39**: 19–40.
1117 Salaj M, Barinka F, Kubová H, et al. 2021. Differences in expression of calcium binding
1118 proteins in the perirhinal and retrosplenial cortex of the rat. *Physiological Research /*
1119 *Academia Scientiarum Bohemoslovaca*, **70**(2): 273–285.
1120 Sargolini F, Fyhn M, Hafting T, et al. 2006. Conjunctive representation of position,
1121 direction, and velocity in entorhinal cortex. *Science*, **312**(5774): 758–762.
1122 Savier E, Sedigh-Sarvestani M, Wimmer R, et al. 2021. A bright future for the tree
1123 shrew in neuroscience research: Summary from the inaugural Tree Shrew Users
1124 Meeting. *Zoological Research*, **42**(4): 478–481.
1125 Schneider CA, Rasband WS, Eliceiri KW. 2012. NIH Image to ImageJ: 25 years of
1126 image analysis. *Nature Methods*, **9**(7): 671–675.
1127 Seress L, Nitsch R, Leranth C. 1993. Calretinin immunoreactivity in the monkey
1128 hippocampal formation--I. Light and electron microscopic characteristics and co-
1129 localization with other calcium-binding proteins. *Neuroscience*, **55**(3): 775–796.
1130 Setti SE & Reed MN. 2022. Network activity changes in the pathophysiology of

Alzheimer's disease: the role of aging and early entorhinal cortex dysfunction. *Metabolic Brain Disease*, **37**(2): 289–298.

Skeen LC & Hall WC. 1977. Efferent projections of the main and the accessory olfactory bulb in the tree shrew (*Tupaia glis*). *The Journal of Comparative Neurology*, **172**(1): 1–35.

Smaluhn N, Plaschke M, Leranth C, et al. 2000. The transentorhinal cortex of the African green monkey: a combined light- and electron-microscopic study of calcium-binding protein containing neurons. *Anatomy and Embryology*, **202**(2): 143–158.

Solstad T, Boccara CN, Kropff E, et al. 2008. Representation of geometric borders in the entorhinal cortex. *Science*, **322**(5909): 1865–1868.

Sugar J & Moser MB. 2019. Episodic memory: Neuronal codes for what, where, and when. *Hippocampus*, **29**(12): 1190–1205.

Sürmeli G, Marcu DC, Mcclure C, et al. 2015. Molecularly Defined Circuitry Reveals Input-Output Segregation in Deep Layers of the Medial Entorhinal Cortex. *Neuron*, **88**(5): 1040–1053.

Suzuki WA & Amaral DG. 1994. Topographic organization of the reciprocal connections between the monkey entorhinal cortex and the perirhinal and parahippocampal cortices. *The Journal of Neuroscience : the Official Journal of the Society for Neuroscience*, **14**(3 Pt 2): 1856–1877.

Suzuki WA & Porteros A. 2002. Distribution of calbindin D-28k in the entorhinal, perirhinal, and parahippocampal cortices of the macaque monkey. *The Journal of Comparative Neurology*, **451**(4): 392–412.

1153 Syversen IF, Reznik D, Witter MP, et al. 2024. A combined DTI-fMRI approach for
1154 optimizing the delineation of posteromedial versus anterolateral entorhinal cortex.
1155 *Hippocampus*, **34**(11): 659–672.
1156 Syversen IF, Witter MP, Kobro-Flatmoen A, et al. 2021. Structural connectivity-based
1157 segmentation of the human entorhinal cortex. *NeuroImage*, **245**: 118723.
1158 Tang Q, Burgalossi A, Ebbesen CL, et al. 2016. Functional Architecture of the Rat
1159 Parasubiculum. *The Journal of Neuroscience : the Official Journal of the Society for*
1160 *Neuroscience*, **36**(7): 2289–2301.
1161 Tsoi SY, Öncül M, Svahn E, et al. 2022. Telencephalic outputs from the medial
1162 entorhinal cortex are copied directly to the hippocampus. *Elife*, **11**.
1163 Tukker JJ, Beed P, Brecht M, et al. 2022. Microcircuits for spatial coding in the medial
1164 entorhinal cortex. *Physiological Reviews*, **102**(2): 653–688.
1165 Tulving E. 2002. Episodic memory: from mind to brain. *Annual Review of Psychology*,
1166 **53**: 1–25.
1167 Tuñón T, Insausti R, Ferrer I, et al. 1992. Parvalbumin and calbindin D-28K in the
1168 human entorhinal cortex. An immunohistochemical study. *Brain Research*, **589**(1): 24–
1169 32.
1170 Turner BH, Gupta KC, Mishkin M. 1978. The locus and cytoarchitecture of the
1171 projection areas of the olfactory bulb in Macaca mulatta. *The Journal of Comparative*
1172 *Neurology*, **177**(3): 381–396.
1173 Tward DJ, Sicat CS, Brown T, et al. 2017. Entorhinal and transentorhinal atrophy in
1174 mild cognitive impairment using longitudinal diffeomorphometry. *Alzheimer's &*

Dementia : Diagnosis, Assessment & Disease Monitoring, **9**: 41–50.

Uva L, Grüschke S, Biella G, et al. 2004. Cytoarchitectonic characterization of the parahippocampal region of the guinea pig. *The Journal of Comparative Neurology*, **474**(2): 289–303.

Van Groen T. 2001. Entorhinal cortex of the mouse: cytoarchitectonical organization. *Hippocampus*, **11**(4): 397–407.

Van Groen T, Miettinen P, Kadish I. 2003. The entorhinal cortex of the mouse: organization of the projection to the hippocampal formation. *Hippocampus*, **13**(1): 133–149.

Van Strien NM, Cappaert NL, Witter MP. 2009. The anatomy of memory: an interactive overview of the parahippocampal-hippocampal network. *Nature Reviews. Neuroscience*, **10**(4): 272–282.

Vandrey B, Garden DLF, Ambrozova V, et al. 2020. Fan Cells in Layer 2 of the Lateral Entorhinal Cortex Are Critical for Episodic-like Memory. *Current Biology : CB*, **30**(1): 169–175 e165.

Varga C, Lee SY, Soltesz I. 2010. Target-selective GABAergic control of entorhinal cortex output. *Nature Neuroscience*, **13**(7): 822–824.

Vismer MS, Forcelli PA, Skopin MD, et al. 2015. The piriform, perirhinal, and entorhinal cortex in seizure generation. *Frontiers in Neural Circuits*, **9**: 27.

Wang C, Chen X, Knierim JJ. 2020a. Egocentric and allocentric representations of space in the rodent brain. *Current Opinion in Neurobiology*, **60**: 12–20.

Wang L, Lu J, Zeng Y, et al. 2020b. Improving Alzheimer's disease by altering gut

1197 microbiota in tree shrews with ginsenoside Rg1. *FEMS Microbiology letters*, **367**(4).
1198 Witter MP. 2006. Connections of the subiculum of the rat: topography in relation to
1199 columnar and laminar organization. *Behavioural Brain Research*, **174**(2): 251–264.
1200 Witter MP. 2007. The perforant path: projections from the entorhinal cortex to the
1201 dentate gyrus. *Progress in Brain Research*, **163**: 43–61.
1202 Witter MP & Amaral DG. 1991. Entorhinal cortex of the monkey: V. projections to the
1203 dentate gyrus, hippocampus, and subicular complex. *The Journal of Comparative*
1204 *Neurology*, **307**(3): 437–459.
1205 Witter MP & Amaral DG. 2021. The entorhinal cortex of the monkey: VI. Organization
1206 of projections from the hippocampus, subiculum, presubiculum, and parasubiculum.
1207 *The Journal of Comparative Neurology*, **529**(4): 828–852.
1208 Witter MP, Doan TP, Jacobsen B, et al. 2017. Architecture of the Entorhinal Cortex A
1209 Review of Entorhinal Anatomy in Rodents with Some Comparative Notes. *Frontiers in*
1210 *Systems Neuroscience*, **11**: 46.
1211 Wong P & Kaas JH. 2009. Architectonic subdivisions of neocortex in the tree shrew
1212 (*Tupaia belangeri*). *The Anatomical Record : Advances in Integrative Anatomy and*
1213 *Evolutionary Biology*, **292**(7): 994–1027.
1214 Wouterlood FG, Härtig W, Brückner G, et al. 1995. Parvalbumin-immunoreactive
1215 neurons in the entorhinal cortex of the rat: localization, morphology, connectivity and
1216 ultrastructure. *Journal of Neurocytology*, **24**(2): 135–153.
1217 Wouterlood FG & Hrtig W. 1995. Calretinin-immunoreactivity in mitral cells of the rat
1218 olfactory bulb. *Brain Research*, **682**(1-2): 93–100.

1219 Wouterlood FG, Van Denderen JC, Van Haeften T, et al. 2000. Calretinin in the
1220 entorhinal cortex of the rat: distribution, morphology, ultrastructure of neurons, and co-
1221 localization with gamma-aminobutyric acid and parvalbumin. *The Journal of*
1222 *Comparative Neurology*, **425**(2): 177–192.
1223 Woźnicka A, Malinowska M, Kosmal A. 2006. Cytoarchitectonic organization of the
1224 entorhinal cortex of the canine brain. *Brain Research Reviews*, **52**(2): 346–367.
1225 Xu L, Chen SY, Nie WH, et al. 2012. Evaluating the phylogenetic position of Chinese
1226 tree shrew (*Tupaia belangeri chinensis*) based on complete mitochondrial genome:
1227 implication for using tree shrew as an alternative experimental animal to primates in
1228 biomedical research. *Journal of Genetics and Genomics = Yi Chuan Xue Bao*, **39**(3):
1229 131–137.
1230 Yamashita A, Fuchs E, Taira M, et al. 2010. Amyloid beta (Abeta) protein- and amyloid
1231 precursor protein (APP)-immunoreactive structures in the brains of aged tree shrews.
1232 *Current Aging Science*, **3**(3): 230–238.
1233 Yamashita A, Fuchs E, Taira M, et al. 2012. Somatostatin-immunoreactive senile
1234 plaque-like structures in the frontal cortex and nucleus accumbens of aged tree shrews
1235 and Japanese macaques. *Journal of Medical Primatology*, **41**(3): 147–157.
1236 Yao YG, Lu L, Ni RJ, et al. 2024. Study of tree shrew biology and models: A booming
1237 and prosperous field for biomedical research. *Zoological Research*, **45**(4): 877–909.
1238 Ye MS, Zhang JY, Yu DD, et al. 2021. Comprehensive annotation of the Chinese tree
1239 shrew genome by large-scale RNA sequencing and long-read isoform sequencing.
1240 *Zoological Research*, **42**(6): 692–709.

Yenkoyan KB, Kotova MM, Apukhtin KV, et al. 2025. Experimental modeling of Alzheimer's disease: Translational lessons from cross-taxon analyses. *Alzheimer's & Dementia : the Journal of the Alzheimer's Association*, **21**(5): e70273.

Yeung LK, Olsen RK, Bild-Enkin HEP, et al. 2017. Anterolateral Entorhinal Cortex Volume Predicted by Altered Intra-Item Configural Processing. *The Journal of Neuroscience : the Official Journal of the Society for Neuroscience*, **37**(22): 5527–5538.

Ying J, Keinath AT, Lavoie R, et al. 2022. Disruption of the grid cell network in a mouse model of early Alzheimer's disease. *Nature Communication*, **13**(1): 886.

Zeineh MM, Palomero-Gallagher N, Axer M, et al. 2017. Direct Visualization and Mapping of the Spatial Course of Fiber Tracts at Microscopic Resolution in the Human Hippocampus. *Cerebral Cortex*, **27**(3): 1779–1794.

Zhang R, Long JL, Ye YF, et al. 2025. Distributions of parvalbumin, calbindin-D28k, and calretinin in the cerebrum of Chinese tree shrews (*Tupaia belangeri chinensis*): A high-resolution neuroanatomical resource. *Zoological Research*, **46**(4): 893–911.

Zhou J-N & Ni R-J. 2016. The tree shrew (*Tupaia belangeri chinensis*) brain in stereotaxic coordinates. Singapore: Science Press Beijing, Springer.

Zhou M, Zhang F, Zhao L, et al. 2016. Entorhinal cortex: a good biomarker of mild cognitive impairment and mild Alzheimer's disease. *Reviews in the Neurosciences*, **27**(2): 185–195.

Zingg B, Chou XL, Zhang ZG, et al. 2017. AAV-Mediated Anterograde Transsynaptic Tagging: Mapping Corticocollicular Input-Defined Neural Pathways for Defense Behaviors. *Neuron*, **93**(1): 33–47.

Zingg B, Dong HW, Tao HW, et al. 2022. Application of AAV1 for Anterograde Transsynaptic Circuit Mapping and Input-Dependent Neuronal Cataloging. *Current Protocols*, **2**(1): e339.

Zingg B, Peng B, Huang J, et al. 2020. Synaptic Specificity and Application of Anterograde Transsynaptic AAV for Probing Neural Circuitry. *The Journal of Neuroscience : the Official Journal of the Society for Neuroscience*, **40**(16): 3250–3267.

Tables

Table 1 Reagents for retro- and anterograde tracing experiments

Reagent	Company	Catalogue number	Tilter / Concentration	Injection volume	Survival time
AAV2/9-CMV-eGFP	HanBio	43051525	1.30×10^{12}	0.5–1.0 μl	21 days
AAV2/8-hSyn-SYP-tdTomato	Taitool Bioscience	S0413-8-H50	1.75×10^{12}	0.5–1.0 μl	21 days
AAV1-hSyn-CRE	Brainvta	1-136-S240531	$0.5–1.0\times10^{13}$	1.0 μl	28 days
CTB-488	Brainvta	CTB-488-240906	1.0 μg/μl	1.0 μl	7 days
CTB-555	Brainvta	CTB-555-240924	1.0 μg/μl	1.0–2.0 μl	8 days

Table 2 Primary antibodies for immunofluorescent staining

Immunogen	Host	Type	Producer	Catalogue #	RRID
CB	Mouse	Monoclonal	Swant	300	AB_10000347
CR	Rabbit	Polyclonal	Swant	7697	AB_2619710
NeuN	Mouse	Monoclonal	CST	94403	AB_2904530
NeuN	Rabbit	Polyclonal	Servicebio	GB11138	AB_2868432
Cre	Mouse	Monoclonal	Sigma	MAB3120	AB_2085748
PCP4	Rabbit	Polyclonal	Sigma	HPA005792	AB_1855086
Etv1	Rabbit	Polyclonal	Invitrogen	PA5-77975	AB_2735767

Table 3 Secondary antibodies for immunofluorescent staining

Immunogen	Host	Producer	Catalogue #	Dye conjugated	RRID
Mouse IgG	Goat	Proteintech	SA00009-1	Cy3®	AB_2814746
Rabbit IgG	Goat	Proteintech	SA00009-2	Cy3®	AB_2890957
Mouse IgG	Goat	Proteintech	SA00013-1	DyLight® 488	AB_2810983
Rabbit IgG	Goat	Proteintech	SA00013-2	DyLight® 488	AB_2797132

Figure legends

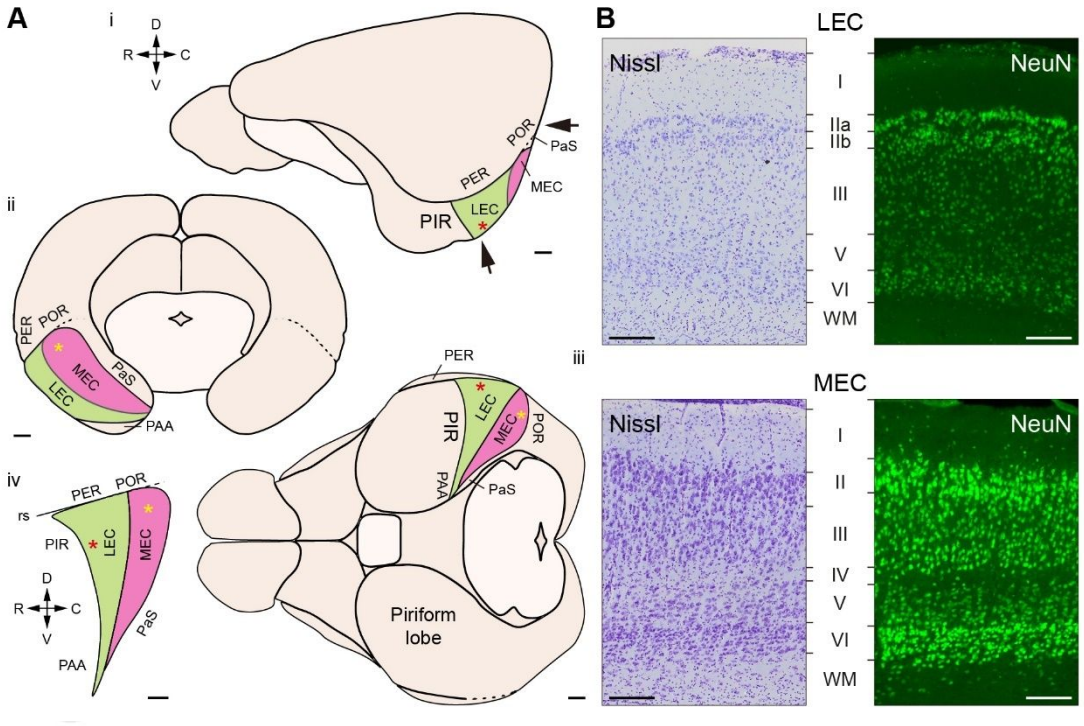

Figure 1. Position and laminar organization of the tree shrew entorhinal cortex

A: Schematic overview. i: Lateral view of the brain showing lateral (pistachio green) and medial (magenta) subdivisions of EC. Arrows indicate viewing angles for ii (posterior) and iii (ventral). iv: Unfolded map of EC reconstructed from serial coronal and sagittal sections; red and yellow asterisks mark locations shown in B. B: Representative sections through LEC (top) and MEC (bottom) stained with Nissl (left)

and NeuN (right); layers numbered with Roman numerals. Abbreviations: C, caudal; D, dorsal; LEC, lateral entorhinal cortex; MEC, medial entorhinal cortex; NeuN, neuronal nuclei; PAA, periamygdaloid cortical area; PaS, parasubiculum; PER, perirhinal cortex; PIR, piriform cortex; POR, postrhinal cortex; R, rostral; rs, rhinal sulcus; V, ventral; WM, white matter. Scale bars: 1 mm (A); 200 μm (B).

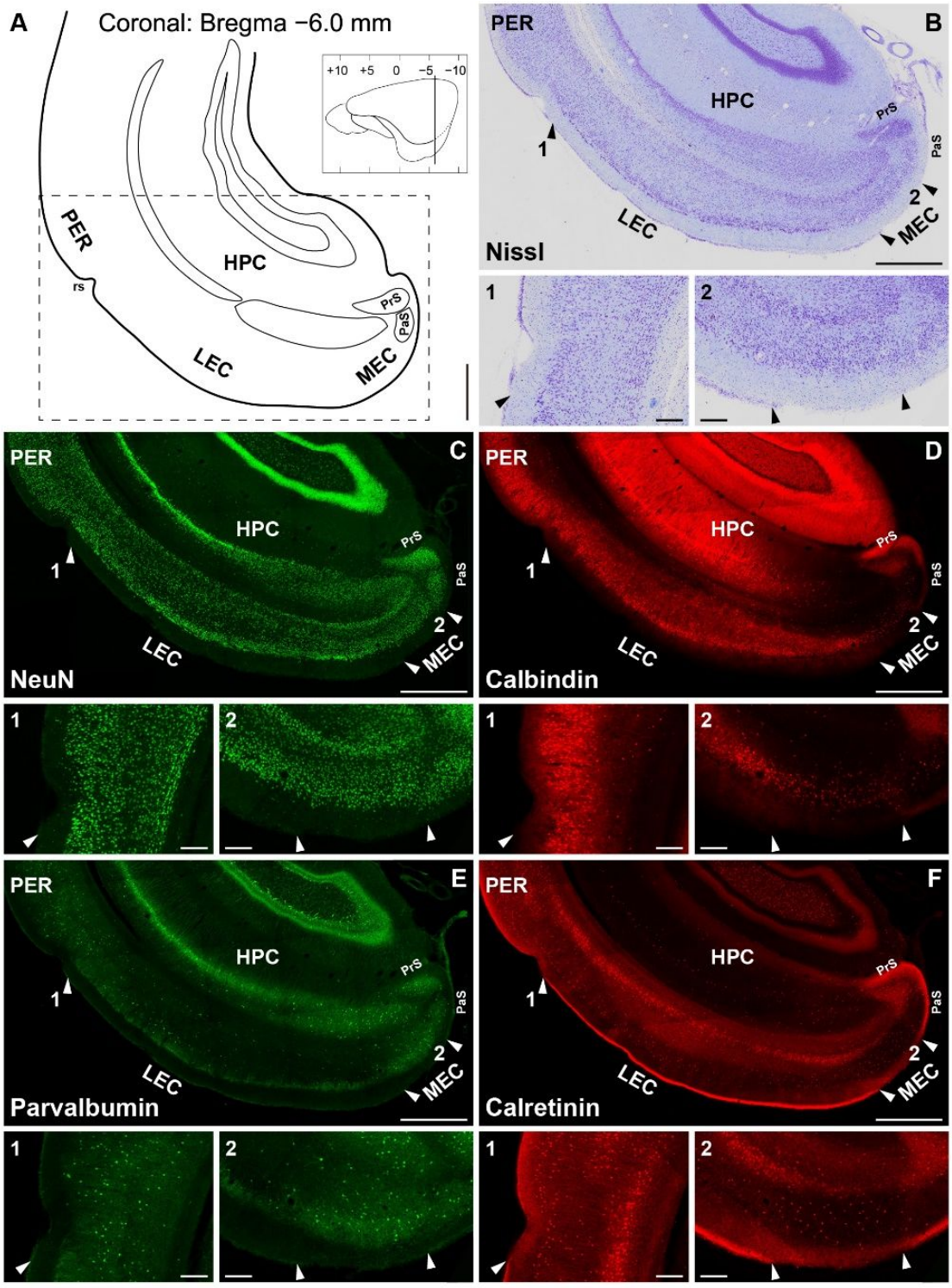

Figure 2. Representative coronal sections of the tree shrew entorhinal cortex

A: Schematic diagram of the parahippocampal region at 6.0 mm posterior to Bregma; boxed area indicates the field shown in B–F. Inset indicates the anteroposterior level. B: Nissl-stained section; arrows delineate regional borders. Numbered insets (bottom) show magnified views of each border (also holds true for C–F). C–F, Adjacent sections immuno-stained for NeuN (C), calbindin (D), parvalbumin (E) and calretinin (F). Abbreviations: HPC, hippocampus; LEC, lateral entorhinal cortex; MEC, medial entorhinal cortex; NeuN, neuronal nuclei; PaS, parasubiculum; PER, perirhinal cortex; PrS, presubiculum; rs, rhinal sulcus. Scale bars: 1 mm (diagram and overview images, left); 200 μm (magnified insets, right).

1328

1329

1330

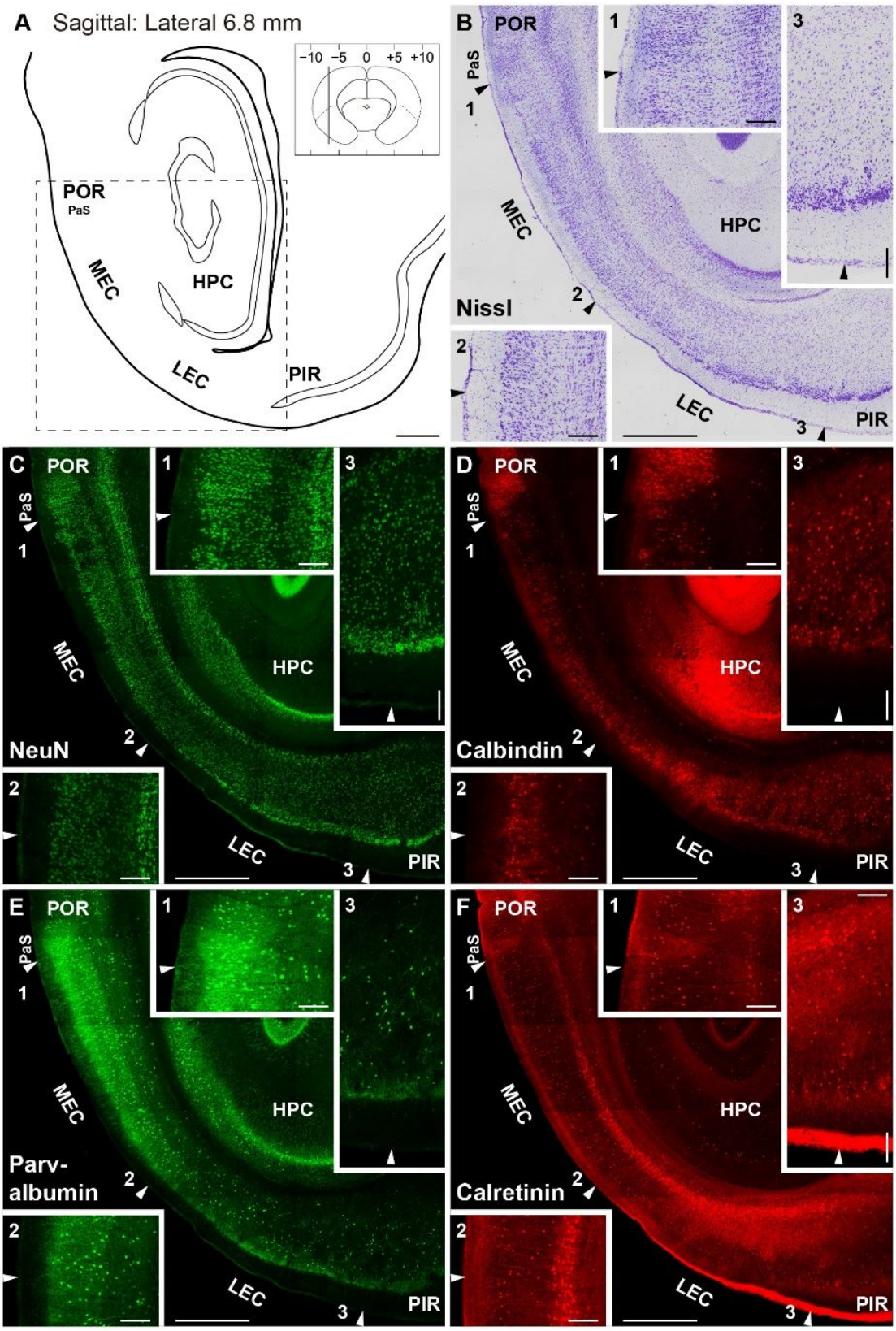

1331

1332

1333

Figure 3. Representative sagittal sections of the tree shrew entorhinal cortex

A: Schematic diagram of the parahippocampal region at 6.8 mm lateral to the midline; boxed area indicates the field shown in in B–F. Inset indicates the mediolateral level. B: Nissl-stained section; arrows delineate regional borders. Numbered insets (bottom left and top right) show magnified views of each border (also holds true for C–F). C–F, Adjacent sections immuno-stained for NeuN (C) & calbindin (D), and parvalbumin (E) & calretinin (F). Abbreviations: HPC, hippocampus; LEC, lateral entorhinal cortex; MEC, medial entorhinal cortex; NeuN, neuronal nuclei; PaS, parasubiculum; PIR, piriform cortex; POR, postrhinal cortex. Scale bars: 1 mm (diagram and overview images, left); 200 μm (magnified insets, right).

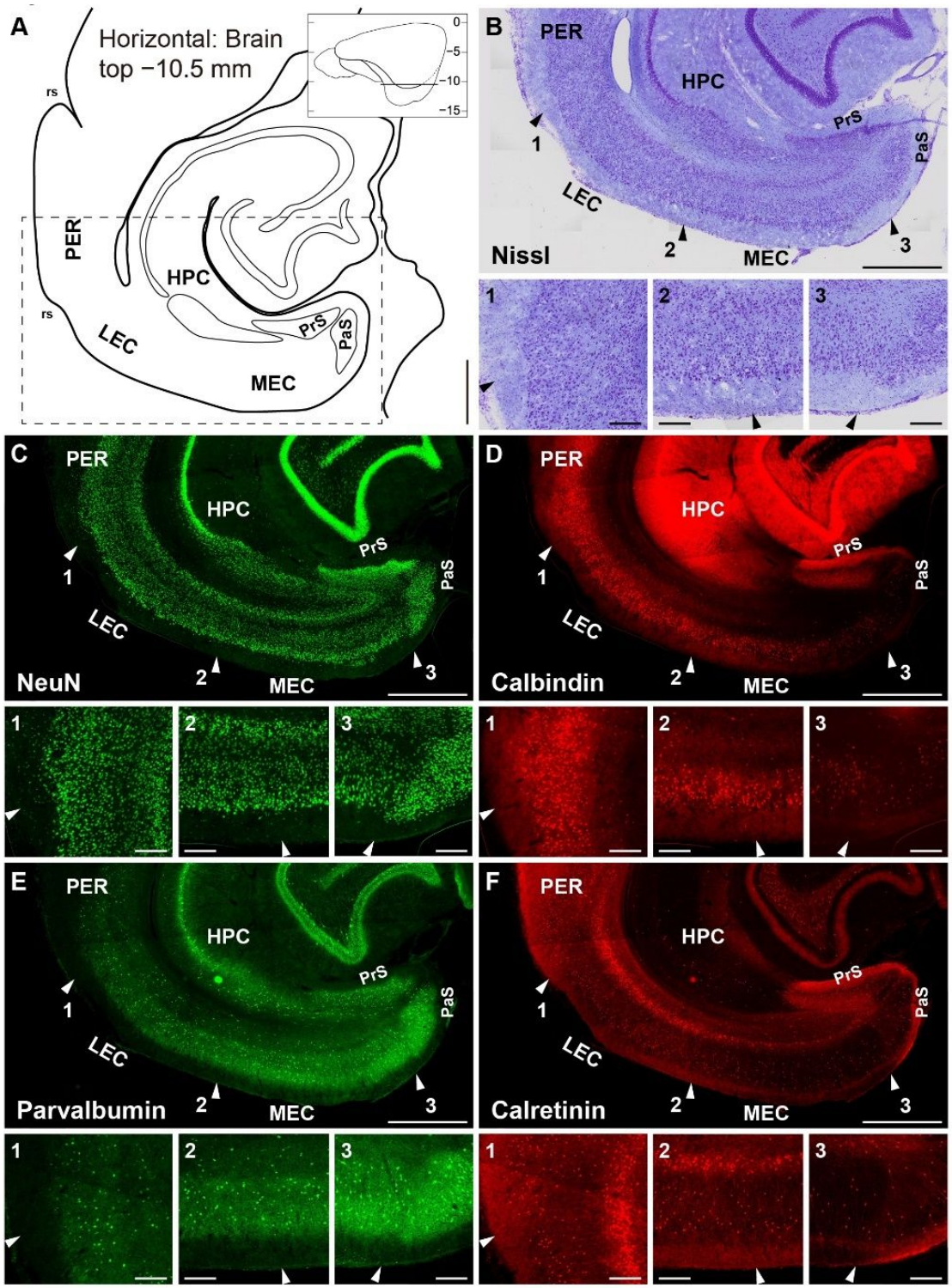

1358

1359

1360

1361

Figure 4. Representative horizontal sections of the tree shrew entorhinal cortex

A: Schematic diagram of the parahippocampal region at 10.5 mm below the dorsal cortical surface; boxed area indicates the field shown in B–F. Inset indicates the dorsoventral level. B: Nissl-stained section; arrows delineate regional borders. Numbered insets (bottom) show magnified views of each border (also holds true for C–F). C–F: Adjacent sections immuno-stained for NeuN (C) & calbindin (D), and parvalbumin (E) & calretinin (F). Abbreviations: HPC, hippocampus; LEC, lateral entorhinal cortex; MEC, medial entorhinal cortex; NeuN, neuronal nuclei; PaS, parasubiculum; PER, perirhinal cortex; PrS, presubiculum; rs, rhinal sulcus. Scale bars: 1 mm (diagram and overview images, left); 200 μm (magnified insets, right).

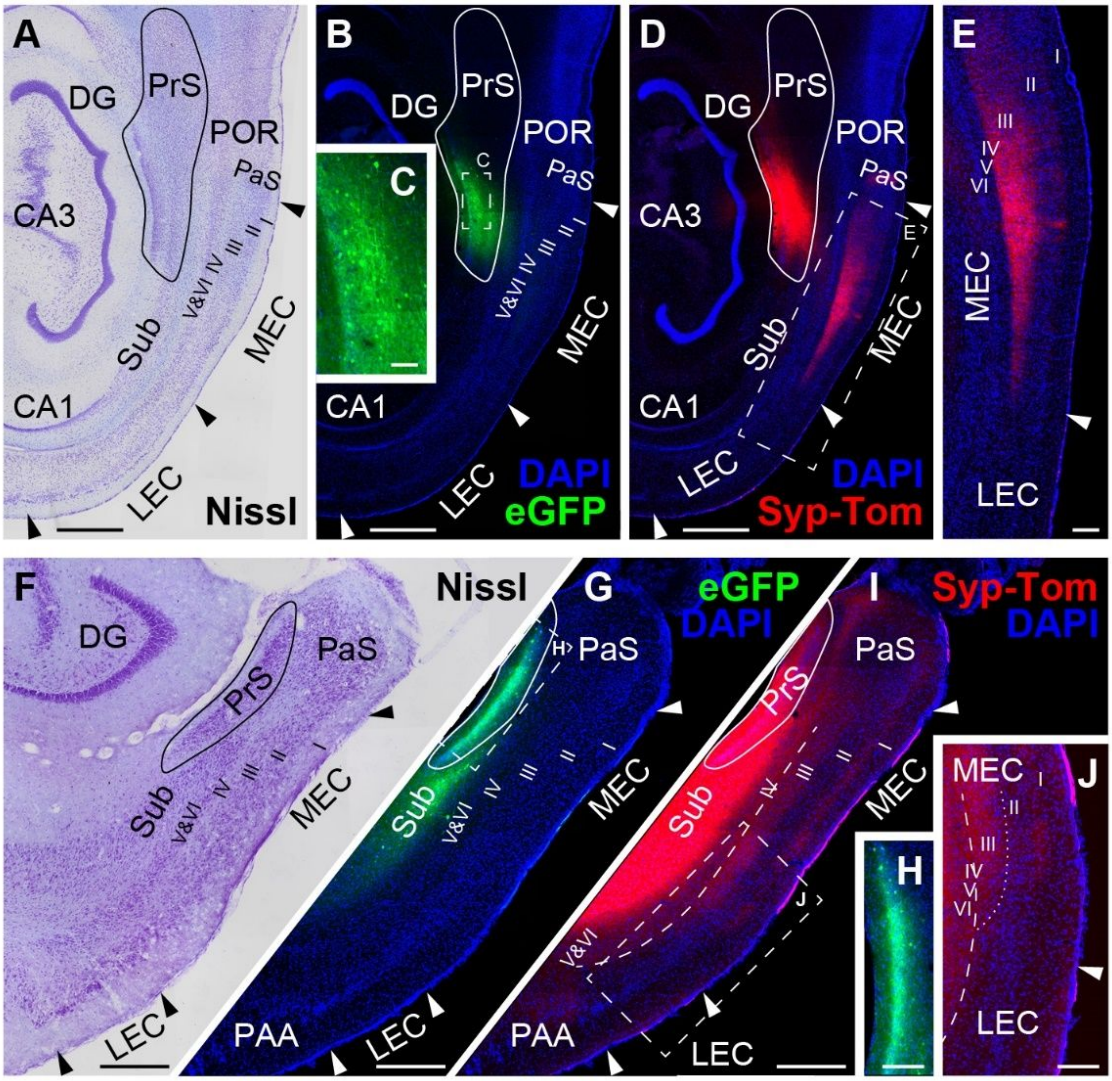

Figure 5. Presubicular projections terminate exclusively in the superficial layers of MEC

A–E: Dorsal-injection experiment. (A) Nissl-stained sagittal section showing the cytoarchitecture of PrS and EC. (B) Adjacent section: eGFP-labeled presubicular cell bodies restricted to dorsomedial PrS. (C) Higher-magnification view of boxed area in B, showing eGFP-positive somata. (D) Anterogradely labeled axon terminals (tdTomato) are confined to MEC layers II–III (Roman numerals). Representative of nine dorsal injections. (E) Magnified view of boxed region in D, illustrating the axonal plexus within MEC. F–J: Ventral-injection experiment. (F) Adjacent Nissl-stained section for anatomical reference. (G) eGFP-expressing neurons in the ventral subiculum and PrS. (H) Higher-magnification view of boxed area in G, showing eGFP-

positive somata. (I) Presubicular terminals remain superficial in MEC; whereas subicular projections target the deep layers of both MEC and LEC. Identical pattern in four ventral injections. Dashed line marks the superficial/deep layer boundary. (J) Magnified view of boxed region in H, displaying the axonal terminals. Dotted line outlines the spread of presubicular terminals in layer III. Abbreviations: DAPI, 4',6-diamidino-2-phenylindole; DG, dentate gyrus; eGFP, enhanced green fluorescent protein; Syp-Tom, synaptophysin-tdTomato; LEC, lateral entorhinal cortex; MEC, medial entorhinal cortex; PAA, periamygdaloid cortical area; PaS, parasubiculum; POR, postrhinal cortex; PrS, presubiculum; Sub, subiculum. Scale bars: 1 mm (A, B, D), 500 μm (F, G, H), 200 μm (E, I, J), 100 μm (C).

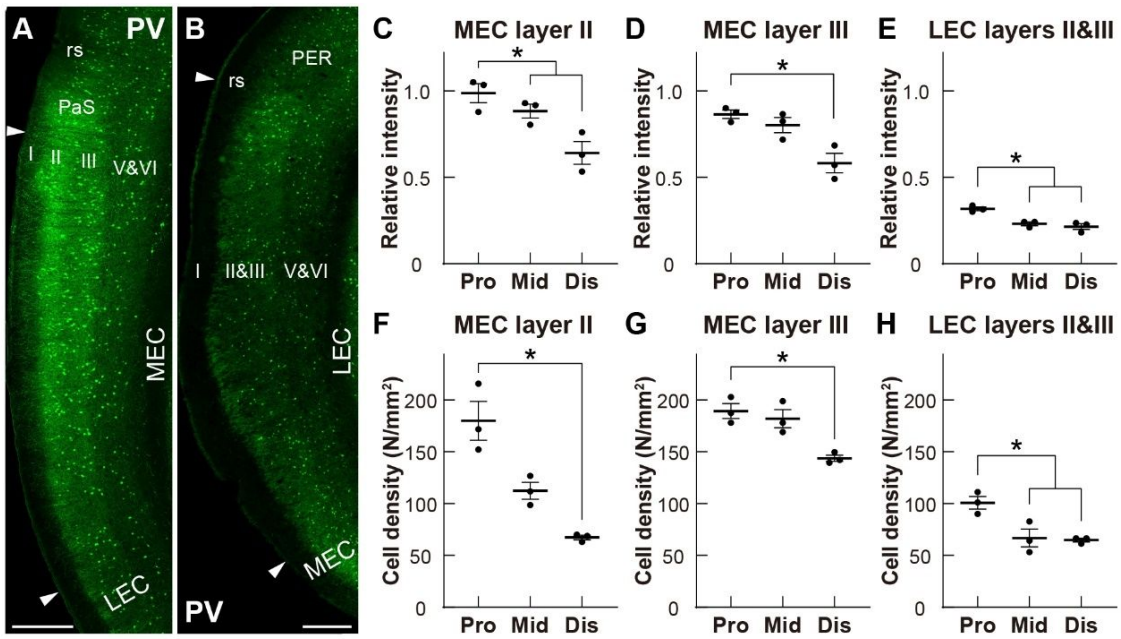

Figure 6. Distance-dependent gradients of PV-ir neuropil and somata relative to the rhinal sulcus.

A, B: Sagittal (A) and coronal (B) sections showing the progressive decline in PV staining across superficial layers (Roman numerals) in MEC and LEC, respectively. Arrows delineate regional borders. Abbreviations: LEC, lateral entorhinal cortex; MEC, medial entorhinal cortex; PaS, parasubiculum; PER, perirhinal cortex; PV, parvalbumin; rs, rhinal sulcus. Scale bars: 500 μm. C–E: PV-ir intensity is highest adjacent to the sulcus and falls distally. Repeated-measures one-way ANOVA with Tukey correction, n = 3 animals. MEC layer II: F = 48.73, $P = 0.012$ (C); layer III: F = 29.52, $P = 0.018$ (D); LEC layers II–III: F = 34.67, $P = 0.018$ (E). Relative intensity = ratio of ROI fluorescence to that of the neocortex. Pro, proximal; Mid, middle; Dis, distal. F–H: Density of PV-ir somata follows the same proximo-distal gradient. MEC layer II: F = 32.85, $P = 0.013$ (F); layer III: F = 24.75, $P = 0.038$ (G); LEC: F = 24.71, $P = 0.036$ (H). *, $P < 0.05$.

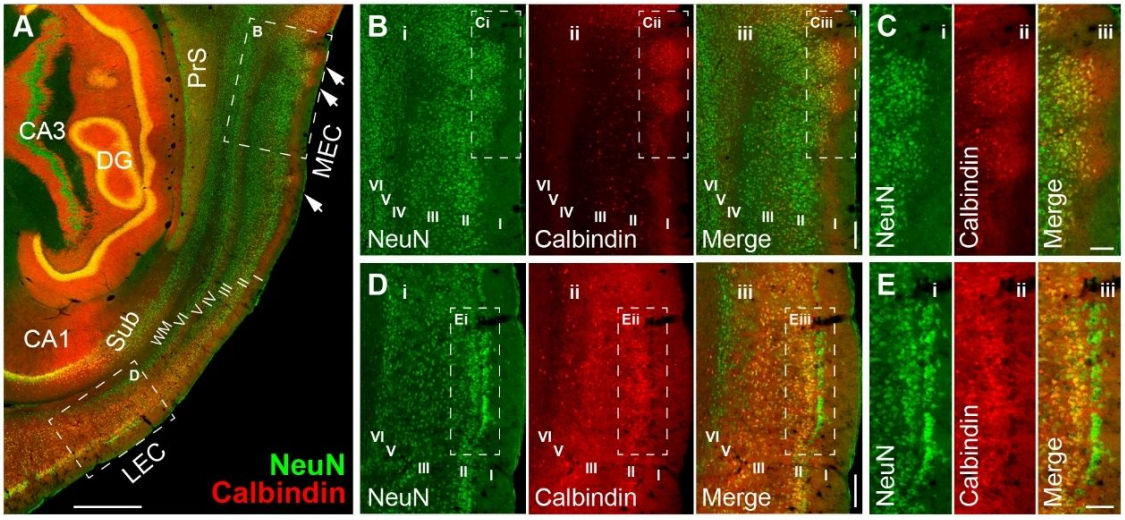

Figure 7. Distribution of CB-ir neurons in the EC.

A: Overview of an EC sagittal section double-labelled for NeuN (green) and calbindin (red). Roman numerals indicate layers; arrows indicate CB-rich clusters in MEC. B: Higher-magnification views of CB-expression patterns in MEC. C: Magnified view of boxed region in B, illustrating CB-ir clusters in MEC. D, E: Magnified view of LEC (D) and its layer II sub-laminae (E). Abbreviations: DG, dentate gyrus, LEC, lateral entorhinal cortex; MEC, medial entorhinal cortex; NeuN, neuronal nuclei; PrS, presubiculum; Sub, subiculum; WM, white matter. Scale bars: 1 mm (A), 200 μm (B, C), 100 μm (D, E).

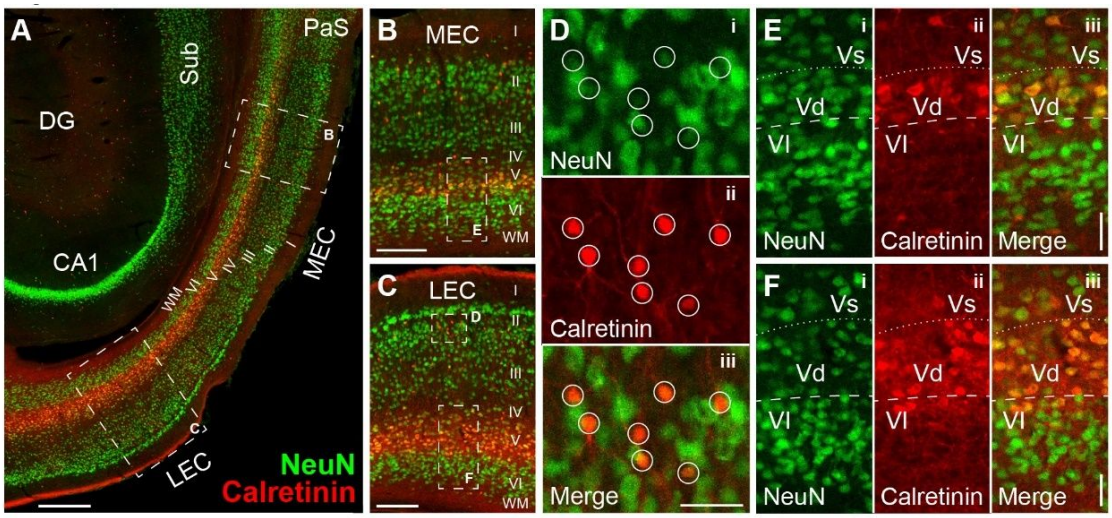

Figure 8. CR expression subdivides entorhinal layer V into superficial and deep sub-laminae.

A: Low-magnification overview of an EC sagittal section double-immunostained for NeuN (green) and calretinin (red). Roman numerals indicate layers. B, C: Higher magnification views of boxed regions in A. D: Enlargement of layer II from C, showing small, vertically oriented CR-ir neurons (circles) that are largely NeuN-negative. E, F: Layer V high power images (dashed line marks layer V/VI border) demonstrating co-localization of CR and NeuN in layer V. Both MEC (E) and LEC (F) exhibit a superficial sub-lamina with weak CR expression (Vs) and a deep sub-lamina with strong CR expression (Vd), marked by dotted line. Abbreviations: DG, dentate gyrus; LEC, lateral entorhinal cortex; MEC, medial entorhinal cortex; NeuN, neuronal nuclei; PaS, parasubiculum; Sub, subiculum; Vd, deep entorhinal layer V; Vs, superficial entorhinal layer V; WM, white matter. Scale bars: 500 μm (A), 200 μm (B, C), 50 μm (D, E, F).

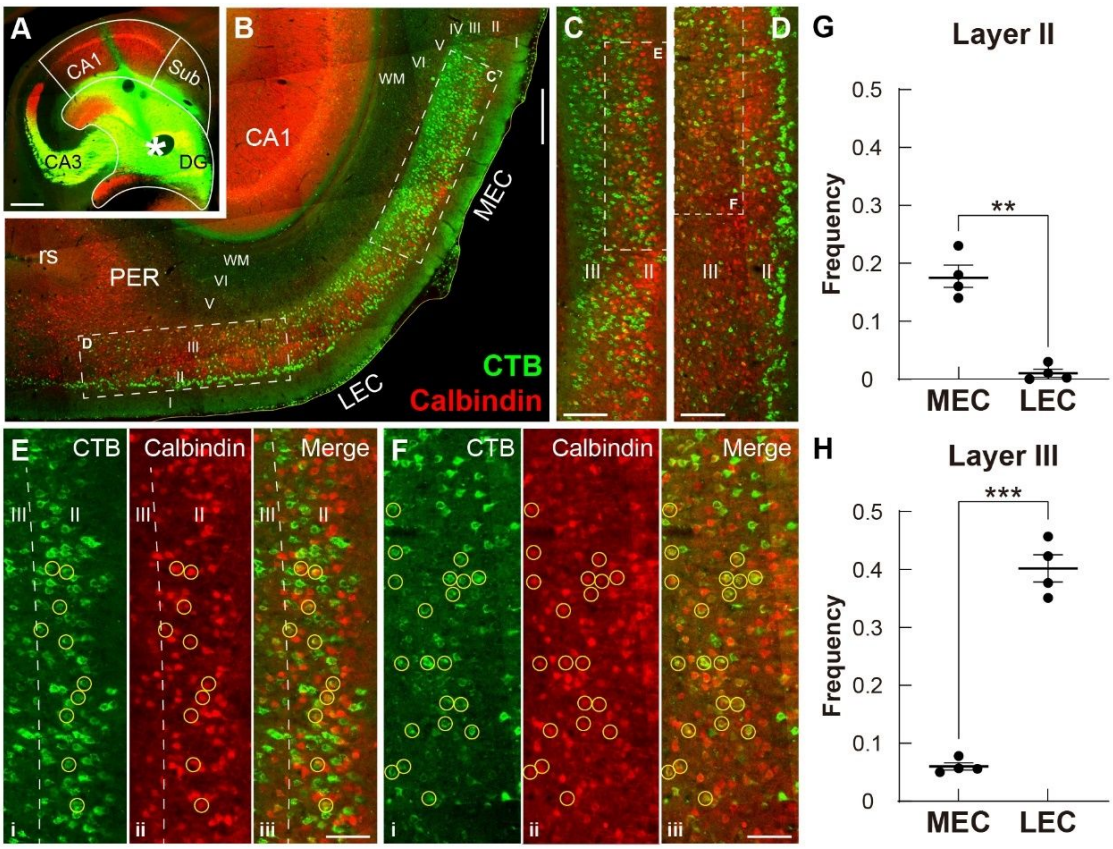

Figure 9. Distribution of hippocampus-projecting neurons in the EC.

A: CTB injection site (star) in dorsal hippocampus; green fluorescence covers CA1, subiculum and DG. B: Sagittal section co-stained for CB showing retrogradely CTB-labelled (green) neurons after injection in A. Note the near absence of labelled somata in deep layers, especially layer V; representative of seven dorsal injections. C, D: Magnified views of boxed regions in B (intensities adjusted). CTB-positive neurons are restricted to superficial MEC (C) and LEC (D). E, F: Further enlargements. Double-labelled neurons (yellow circles) are evident in MEC layer II (E) and LEC layer III (F). Dashed line indicates the layer II/III boundary. G, H: Quantification of double-labelled neurons in layers II and III (mean ± SEM, n = 4 animals, paired *t*-test; layer II: $t = 6.998$, $P = 0.006$; layer III: $t = 18.56$, $P < 0.001$). **, $P < 0.01$; ***, $P < 0.001$. Abbreviations: CTB, cholera toxin subunit B; DG, dentate gyrus; LEC, lateral entorhinal cortex; MEC, medial entorhinal cortex; PER, perirhinal cortex; rs, rhinal sulcus; Sub, subiculum; WM, white matter. Scale bars: 500 μm (A, B), 200 μm (C, D), 100 μm (E, F).

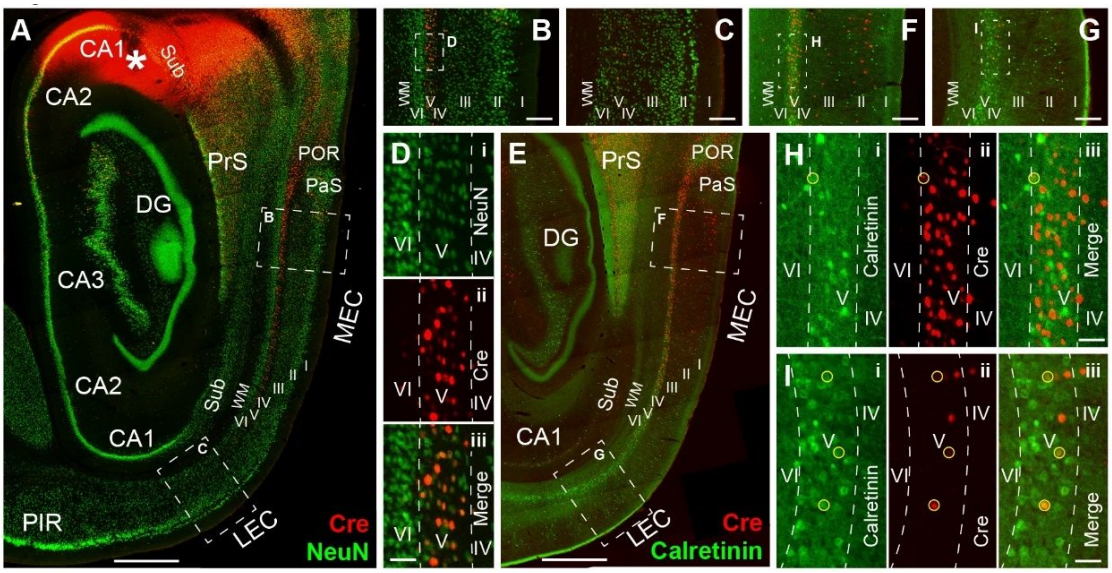

Figure 10. Hippocampal-recipient neurons occupy the full depth of entorhinal layer V.

A: Sagittal section through the EC after AAV-Cre injection into dorsal CA1 (star). Cre-positive neurons (red) are concentrated in layer V of MEC and sparse in superficial layers. NeuN co-stained (green). Roman numerals indicate layers. Results representative of three dorsal injections. B, C: Higher-magnification views of boxed regions in A, illustrating dense Cre-ir somata in MEC layer V (B) and sparse labeling in LEC (C). D: Enlargement of boxed area in B. Dashed lines delimit the layers. Neurons are distributed throughout layer V without sub-laminar clustering. E: Adjacent section co-stained for CR (green). F, G: Higher-magnification views of boxed regions in E (green/red intensities adjusted for visibility). H, I: Enlarged views of boxed regions in F and G. MEC layer V contains numerous Cre+, CR− neurons (H), whereas LEC shows sparse Cr+ cells that frequently co-express CR (I). Yellow circles mark double-labeled somata. Abbreviations: DG, dentate gyrus; LEC, lateral entorhinal cortex; MEC, medial entorhinal cortex; NeuN, neuronal nuclei; PaS, parasubiculum; PIR, piriform cortex; POR, postrhinal cortex; PrS, presubiculum; Sub, subiculum; WM, white matter. Scale bars: 1 mm (A, E), 200 μm (B, C, F, G), 50 μm (D, H, I).

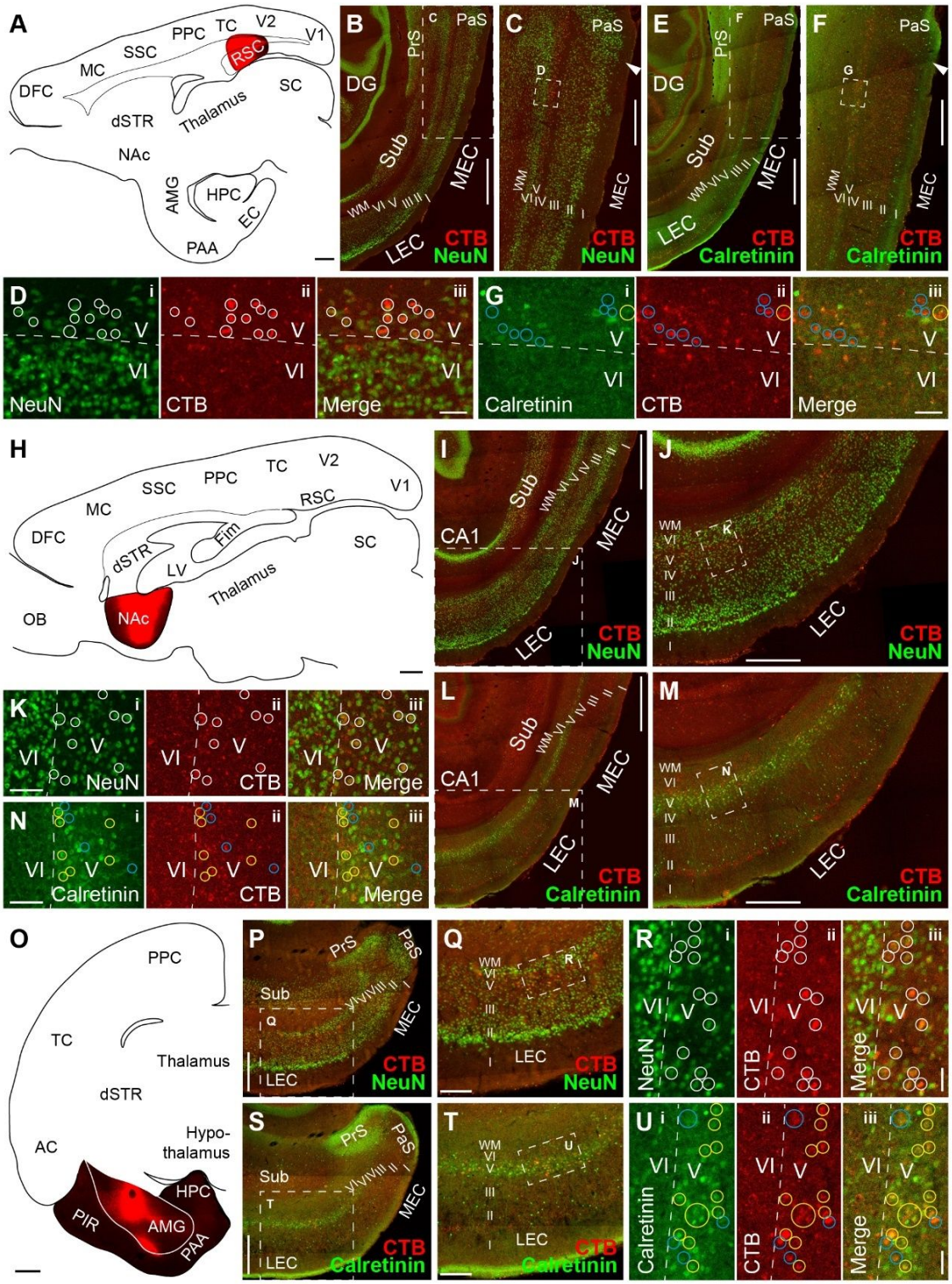

1509

1510 **Figure 11. Telencephalon-projecting neurons distributed throughout entorhinal**

1511 **layer V without sub-laminar segregation.**

1512 A: CTB injection in retrosplenial cortex. B: NeuN-co-stained section showing CTB+

1513 neurons in the EC, mainly dorsal MEC. C: Magnification of boxed region in B, CTB-

labeling is limited to layer V. D: Further enlargement of the boxed area in C; CTB+ cells (circles) occupy the entire depth of layer V without sub-laminar clustering. E–G: Consecutive section co-stained for CR; sparse CR expression in dorsal MEC yields predominantly CTB+/CR− neurons (blue circles). Data representative of two experiments H: CTB injection site in nucleus accumbens. I: NeuN-co-stained sagittal section showing CTB-labeled neurons in ventral EC, concentrated in the LEC. J: Higher-magnification view of boxed region in I, labeling is restricted to layer V. K: Enlargement of boxed region in J; dashed line marks layer V/VI border. CTB+ somata (circles) span the full thickness of layer V. L–M: Consecutive section co-stained for CR. In the LEC, CR+/CTB+ neurons (yellow circles) intermingle with CTB+ only cells (blue circles) throughout layer V, confirming absence of sub-laminar segregation. Data representative of two experiments. O–U: As H–N, but after CTB injection in amygdala; CTB+ somata remain confined to layer V of ventral LEC and distribute evenly across the layer. Data representative of two experiments. For all panels: Roman numerals indicate layers in EC. Note: Autofluorescence in LEC layer IIa (panels E, L, M, T) can mask the red channel; the signal shown does not represent genuine CTB labeling. Abbreviations: AC, auditory cortex; AMG, amygdala; CTB, cholera toxin subunit B; DFC, dorsal frontal cortex; DG, dentate gyrus; dSTR, dorsal striatum; EC, entorhinal cortex; Fim, fimbria of the hippocampus; HPC, hippocampus; LEC, lateral entorhinal cortex; LV, lateral ventricle; MC, motor cortex; MEC, medial entorhinal cortex; NAc, nucleus accumbens; NeuN, neuronal nuclei; OB, olfactory bulb; PAA, periamygdaloid cortical area; PaS, parasubiculum; PIR, piriform cortex; PrS, presubiculum; PPC, Posterior parietal cortex; RSC, retrosplenial cortex; SC, superior colliculus; SSC, somatosensory cortex; Sub, subiculum; TC, temporal cortex; V1, primary visual cortex; V2, secondary visual cortex; WM, white matter. Scale bars: 1 mm (A, B, E, H, I, L, O), 500 μm (C, F, J, M, P, S), 200 μm (Q, T), 100 μm (D, G, K, N), 50 μm (R, U).

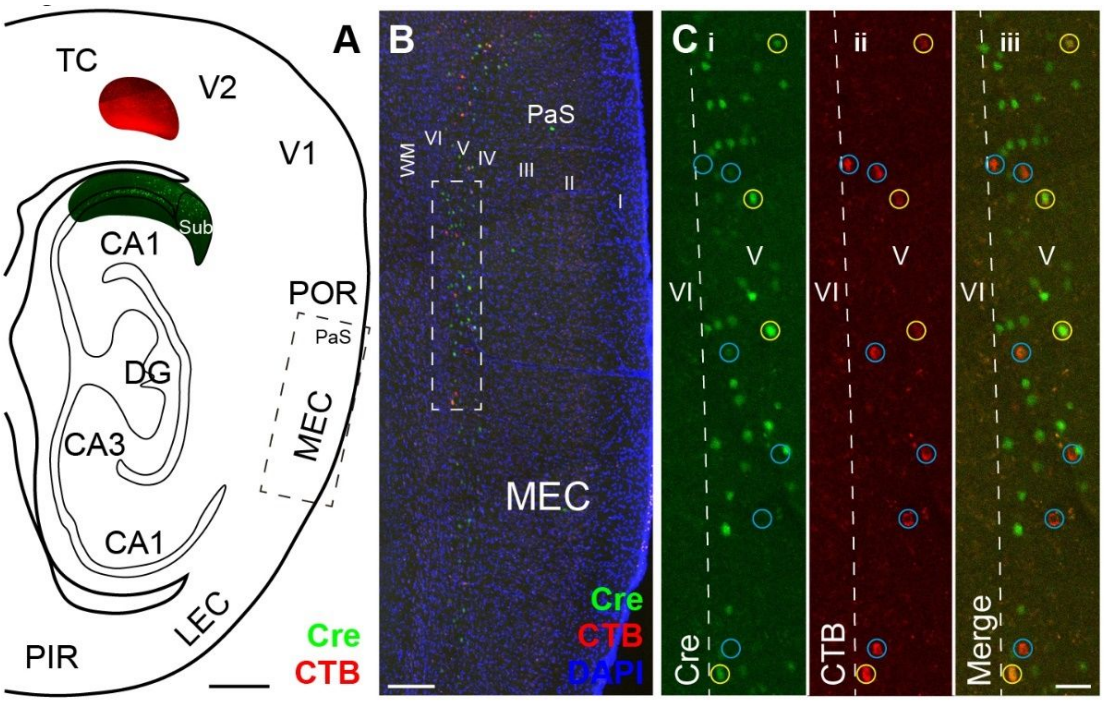

Figure 12. Hippocampal-recipient and telencephalon-projecting neurons are intermingled within entorhinal layer V.

A: Dual-tracer strategy: CTB (red) was injected into secondary visual cortex (deep layers, at the border with temporal cortex); AAV-Cre (green) was delivered to dorsal CA1 and subiculum. B: Sagittal section through MEC showing sparse Cre+ (green) and CTB+ (red) somata scattered throughout layer V; no sub-laminar segregation is evident. Roman numerals denote cortical layers. C: Higher-magnification view of boxed region in B; CTB+ neurons (yellow and blue circles) intermix freely with Cre+ neurons with partial overlap (yellow circles). Abbreviations: CTB, cholera toxin subunit B; DG, dentate gyrus; LEC, lateral entorhinal cortex; MEC, medial entorhinal cortex; PaS, parasubiculum; PIR, piriform cortex; Sub, subiculum; TC, temporal cortex; V1, primary visual cortex; V2, secondary visual cortex; WM, white matter. Scale bars: 1 mm (A), 200 μm (B), 50 μm (C).

Supplementary tables

Supplementary Table S1 List of resource sections included in the figures

Figures	Anatomical level	TS ID	Nissl	NeuN&CB	PV&CR
Fig. 2	AP 6.0 mm	T098	P3S16	P3S17	P3S18
Fig. 3	ML 6.8 mm	T031	P4S1	P4S2	P4S3
Fig. 4	DV 10.5 mm	T116	P5S10	P5S11	P5S12
Fig. S2	AP 3.9 mm	T073	P13S7	P13S8	P13S9
Fig. S3	AP 4.6 mm	T015	P6S7	P6S8	P6S9
Fig. S4	AP 5.8 mm	T015	P5S1	P5S2	P5S3
Fig. S5	AP 6.4 mm	T073	P15S19	P15S20	P15S21
Fig. S6	AP 7.3 mm	T054	P4S4	P4S5	P4S3
Fig. S7	AP 7.9 mm	T098	P2S7	P2S8	P2S9
Fig. S8	ML 2.0 mm	T031	P8S7	P8S8	P8S9
Fig. S9	ML 3.0 mm	T072	P7S7	P7S8	P7S9
Fig. S10	ML 4.3 mm	T031	P6S16	P6S17	P6S18
Fig. S11	ML 5.1 mm	T031	P5S19	P5S20	P5S21
Fig. S12	ML 6.3 mm	T031	P4S13	P4S14	P4S15
Fig. S13	ML 7.2 mm	T031	P3S16	P3S17	P3S18
Fig. S14	ML 7.7 mm	T046	P2S19	P2S20	P2S21
Fig. S15	ML 8.1 mm	T046	P2S4	P2S5	P2S6
Fig. S16	DV 7.7 mm	T116	P8S10	P8S11	P8S12
Fig. S17	DV 8.6 mm	T070	P9S7	P9S8	P9S9
Fig. S18	DV 10.0 mm	T116	P6S1	P6S2	P6S3
Fig. S19	DV 10.9 mm	T070	P11S19	P11S20	P11S21
Fig. S20	DV 11.5 mm	T070	P12S7	P12S8	P12S9
Fig. S21	DV 12.5 mm	T070	P13S7	P13S8	P13S9

Abbreviations: AP, anteroposterior; CB, calbindin; CR, calretinin; DV, dorsoventral; ID, identification; ML, mediolateral; NeuN, neuronal nuclei; PV, parvalbumin; TS, tree shrew.

Supplementary Table S2 Antibodies tested but not validated for immunofluorescence in tree shrew brain

Immunogen	Host	Type	Producer	Catalogue #	RRID	Observation
Ctip2	Rat	Monoclonal	Abcam	ab18465	AB_2064130	No specific signal in tree shrew
NeuN	Mouse	Monoclonal	Abcam	ab104224	AB_10711040	WB-positive but no IF signal in tree shrew
Reelin	Mouse	Monoclonal	MBL	D223-3	AB_843523	No specific signal
Reelin	Mouse	Monoclonal	MBL	D351-3	AB_2815002	No specific signal
Reelin	Mouse	Monoclonal	Millipore	MAB5364	AB_2179313	IF-positive in mouse; no signal in tree shrew
Reelin	Mouse	Monoclonal	Millipore	MAB5366	AB_2285132	No specific signal
Reelin	Mouse	Monoclonal	Abcam	ab78540	AB_1603148	IF-positive in mouse and rat; no signal in tree shrew
Reelin	Mouse	Monoclonal	Santa Cruz	sc-25346	AB_628210	No specific signal
Reelin	Rabbit	Polyclonal	Proteintech	20689-1-AP	AB_2878724	No specific signal
Reelin	Rabbit	Polyclonal	Biorbyt	orb11331	AB_10750301	No specific signal
Reelin	Goat	Polyclonal	R&D	AF3820-sp	AB_2847134	No specific signal

SIM1	Rabbit	Polyclonal	Invitrogen	PA5-121467	AB_2915039	WB-positive but no IF signal in tree shrew
WFS1	Rabbit	Polyclonal	Proteintech	26995-1-AP	AB_2880717	IF-positive in rat and tree shrew. Entorhinal WFS1 signal overlaps with CB in rat but not in tree shrew

Abbreviations: CB, calbindin; IF, immunofluorescence; NeuN, neuronal nuclei; SIM1, Single-minded homolog 1; WB, western blot; WFS1, Wolfram syndrome 1.

Note: Lack of validation may reflect batch- or vial-specific variation rather than inherent antibody performance.

Supplementary figure legends

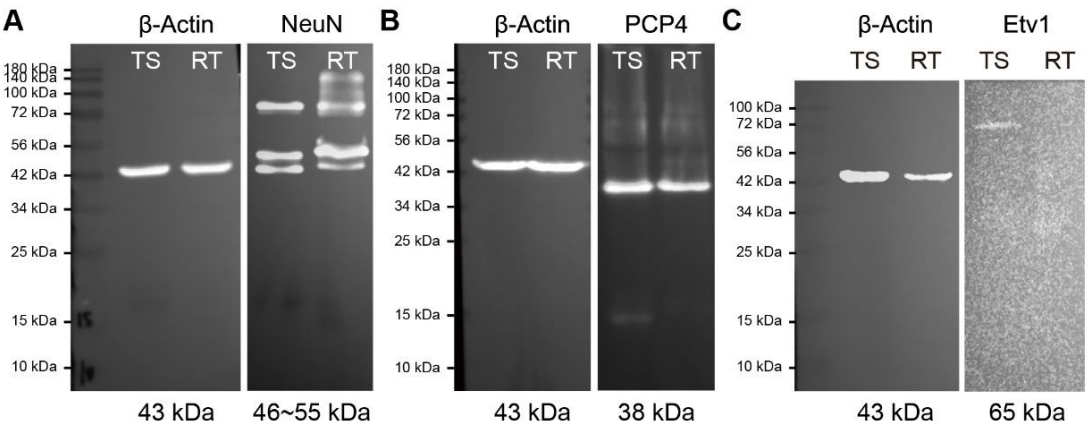

Supplementary Figure S1. Validation of primary antibody specificity by Western blot

Western blots of tree shrew (TS) and rat (RT) brain lysates probed for β-Actin (loading control), NeuN (A), PCP4 (B) and Etv1(C). Predicted molecular weights (kDa) are indicated. As noted in the manufacturer's datasheet, the monoclonal NeuN antibody detects the predicted band along with two additional high-molecular-weight non-specific bands in both species. Nonetheless, immunofluorescence labelling with this antibody yields neuronal-specific staining patterns identical to those obtained with the polyclonal NeuN antibody used in the resource images (Zhang et al., 2025). Etv1 was expressed at very low levels; a weak band was detected in tree shrew hippocampal lysate, but not in rat sample, likely due to limited protein loading (see β-Actin loading control). Abbreviations: Etv1, ETS variant 1; NeuN, neuronal nuclei; PCP4, Purkinje-cell protein 4.

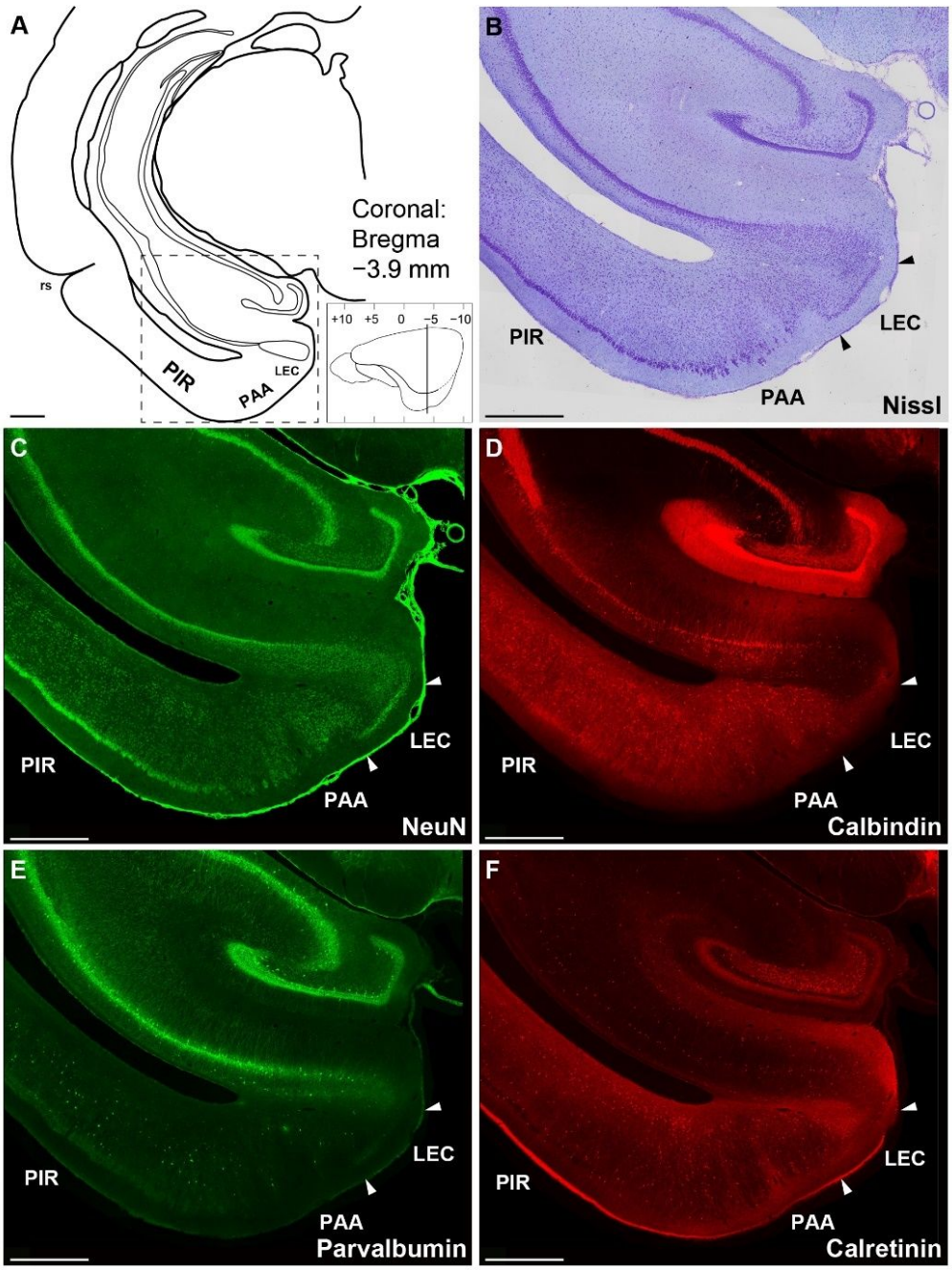

Supplementary Figure S2. Coronal sections through the tree shrew EC at 3.9 mm posterior to Bregma

A: Schematic diagram; boxed area indicates the field shown in B–F. Inset indicates the anteroposterior level. B: Nissl-stained section; arrows denote regional borders. C–F, Adjacent sections immunostained for NeuN (C) & calbindin (D), and parvalbumin (E) & calretinin (F). Abbreviations: EC, entorhinal cortex; LEC, lateral entorhinal cortex; NeuN, neuronal nuclei; PAA, periamygdaloid cortical area; PIR, piriform cortex; rs, rhinal sulcus. Scale bars: 1 mm.

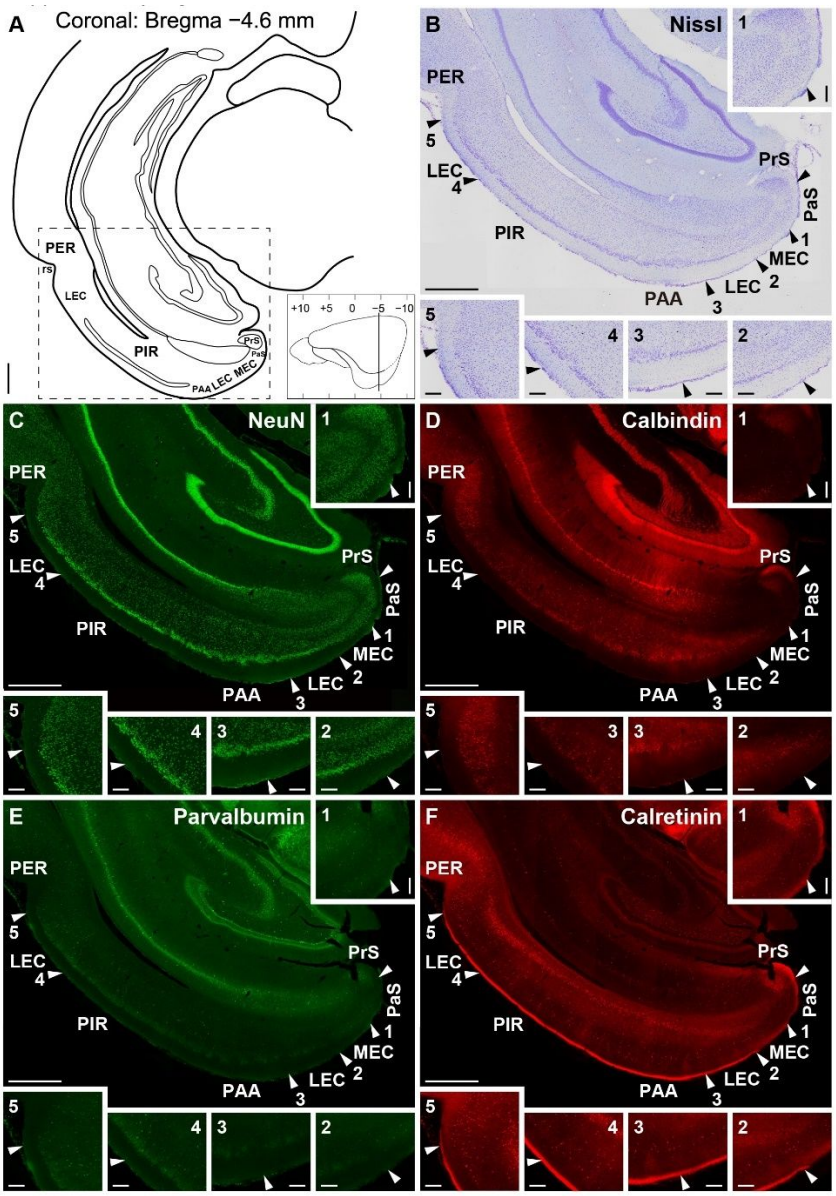

Supplementary Figure S3. Coronal sections through the tree shrew EC at 4.6 mm posterior to Bregma

A: Schematic diagram; boxed area indicates the field shown in B–F. Inset indicates the anteroposterior level. B: Nissl-stained section; arrows denote regional borders. C–F, Adjacent sections immunostained for NeuN (C) & calbindin (D), and parvalbumin (E) & calretinin (F). Abbreviations: EC, entorhinal cortex; LEC, lateral entorhinal cortex; MEC, medial entorhinal cortex; NeuN, neuronal nuclei; PAA, periamygdaloid cortical area; PaS, parasubiculum; PER, perirhinal cortex; PIR, piriform cortex; PrS, presubiculum; rs, rhinal sulcus. Scale bars: 1 mm (diagram and overview images, left); 200 μm (magnified insets, right).

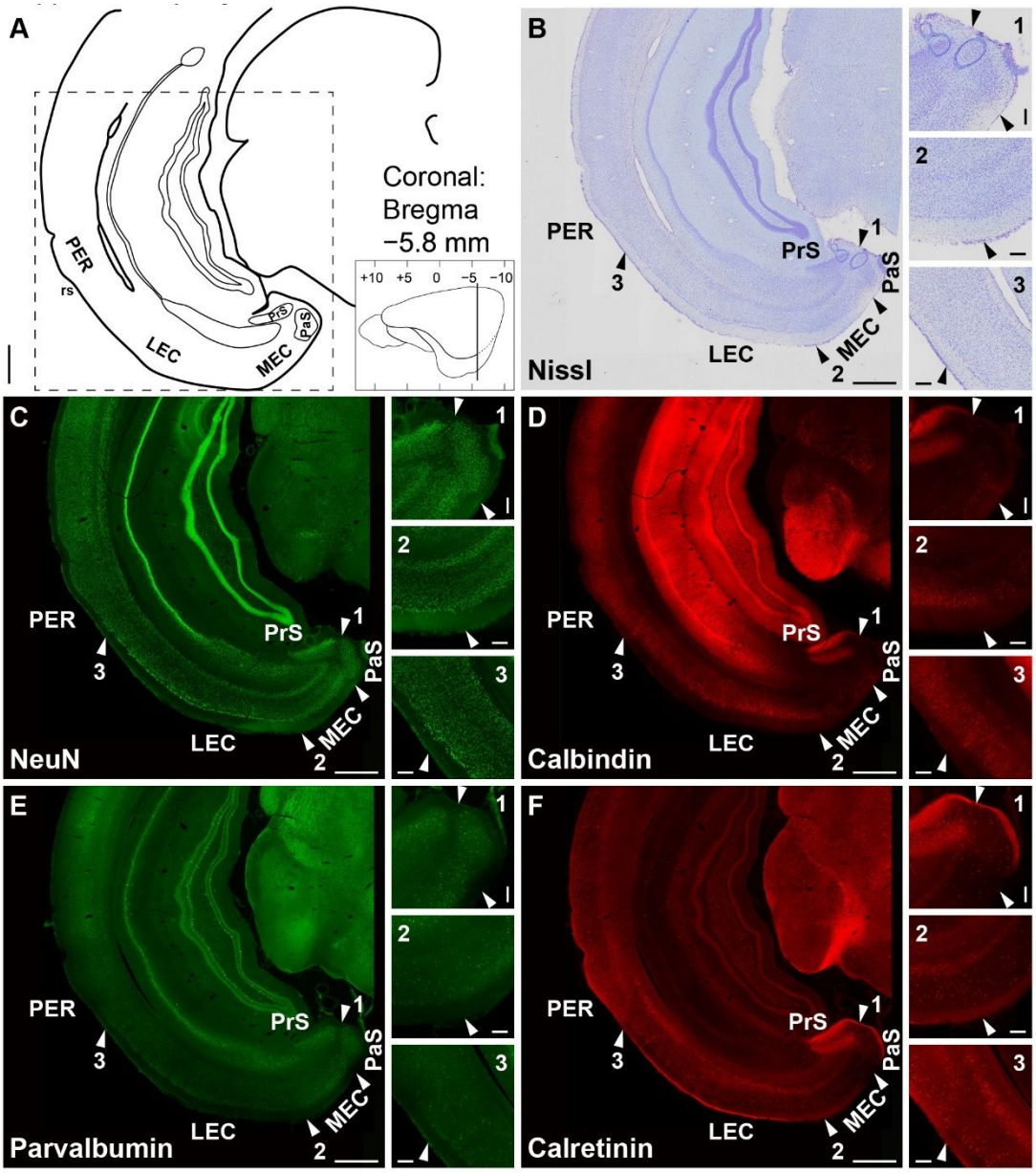

Supplementary Figure S4. Coronal sections through the tree shrew EC at 5.8 mm posterior to Bregma

A: Schematic diagram; boxed area indicates the field shown in B–F. Inset indicates the anteroposterior level. B: Nissl-stained section; arrows denote regional borders. C–F, Adjacent sections immunostained for NeuN (C) & calbindin (D), and parvalbumin (E) & calretinin (F). Abbreviations: EC, entorhinal cortex; LEC, lateral entorhinal cortex; MEC, medial entorhinal cortex; NeuN, neuronal nuclei; PaS, parasubiculum; PER, perirhinal cortex; PrS, presubiculum; rs, rhinal sulcus. Scale bars: 1 mm (diagram and overview images, left); 200 μm (magnified insets, right).

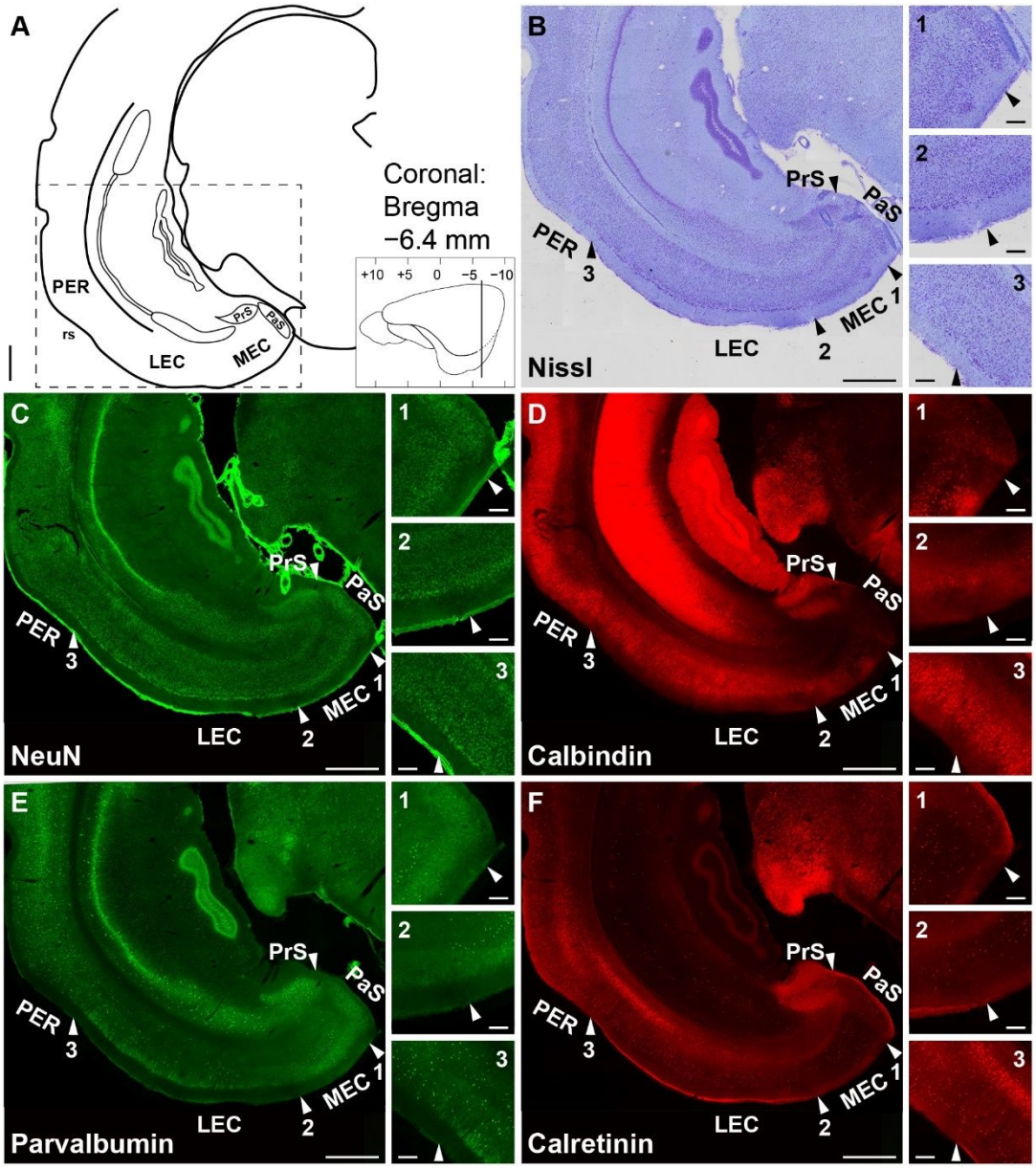

1635

1636 **Supplementary Figure S5. Coronal sections through the tree shrew EC at 6.4 mm**
1637 **posterior to Bregma**

1638 A: Schematic diagram; boxed area indicates the field shown in B–F. Inset indicates the
1639 anteroposterior level. B: Nissl-stained section; arrows denote regional borders. C–F,
1640 Adjacent sections immunostained for NeuN (C) & calbindin (D), and parvalbumin (E)
1641 & calretinin (F). Abbreviations: EC, entorhinal cortex; LEC, lateral entorhinal cortex;
1642 MEC, medial entorhinal cortex; NeuN, neuronal nuclei; PaS, parasubiculum; PER,
1643 perirhinal cortex; PrS, presubiculum; rs, rhinal sulcus. Scale bars: 1 mm (diagram and
1644 overview images, left); 200 μm (magnified insets, right).

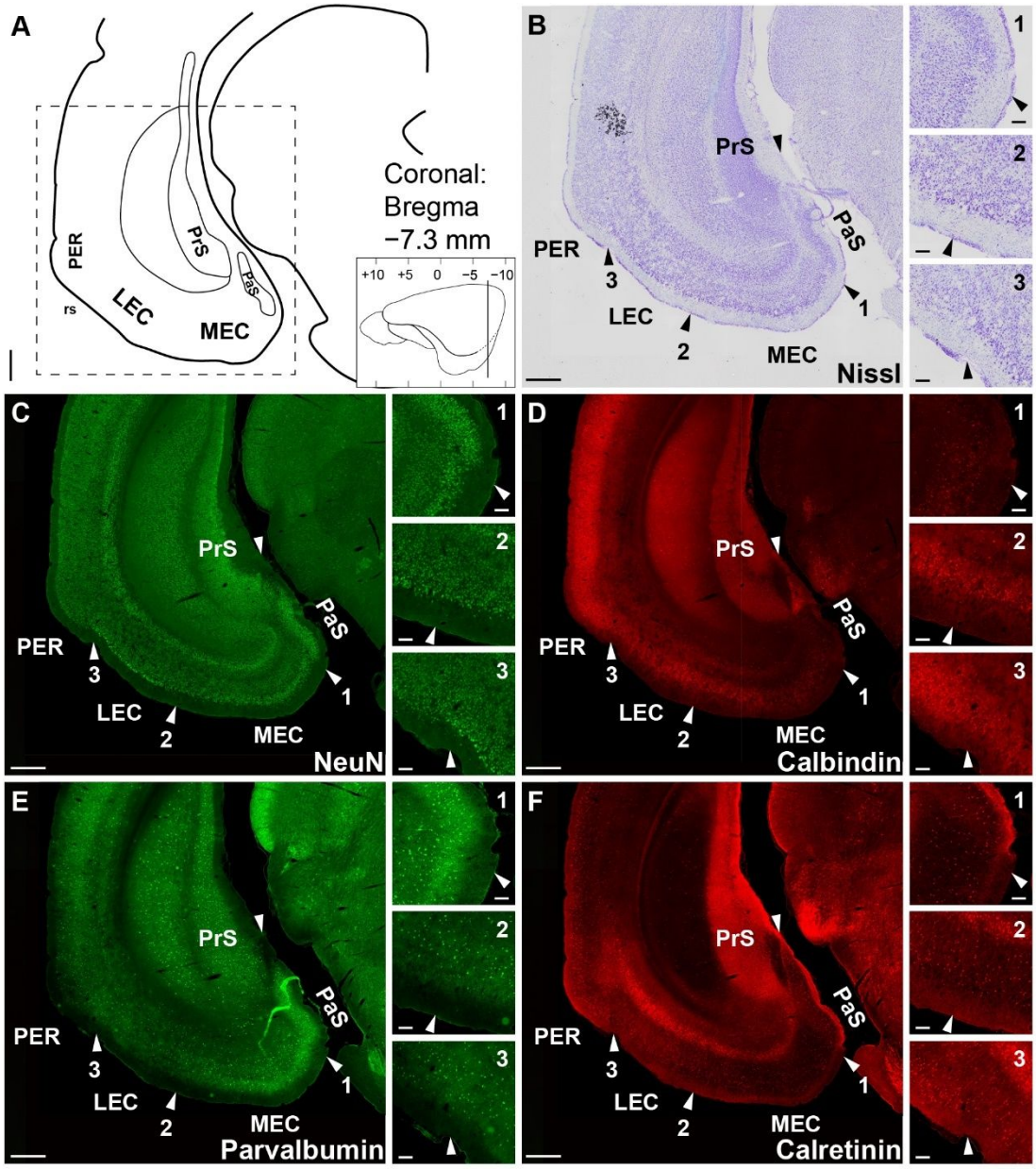

Supplementary Figure S6. Coronal sections through the tree shrew EC at 7.3 mm posterior to Bregma

A: Schematic diagram; boxed area indicates the field shown in B–F. Inset indicates the anteroposterior level. B: Nissl-stained section; arrows denote regional borders. C–F, Adjacent sections immunostained for NeuN (C) & calbindin (D), and parvalbumin (E) & calretinin (F). Abbreviations: EC, entorhinal cortex; LEC, lateral entorhinal cortex; MEC, medial entorhinal cortex; NeuN, neuronal nuclei; PaS, parasubiculum; PER, perirhinal cortex; PrS, presubiculum; rs, rhinal sulcus. Scale bars: 1 mm (diagram and overview images, left); 200 μm (magnified insets, right).

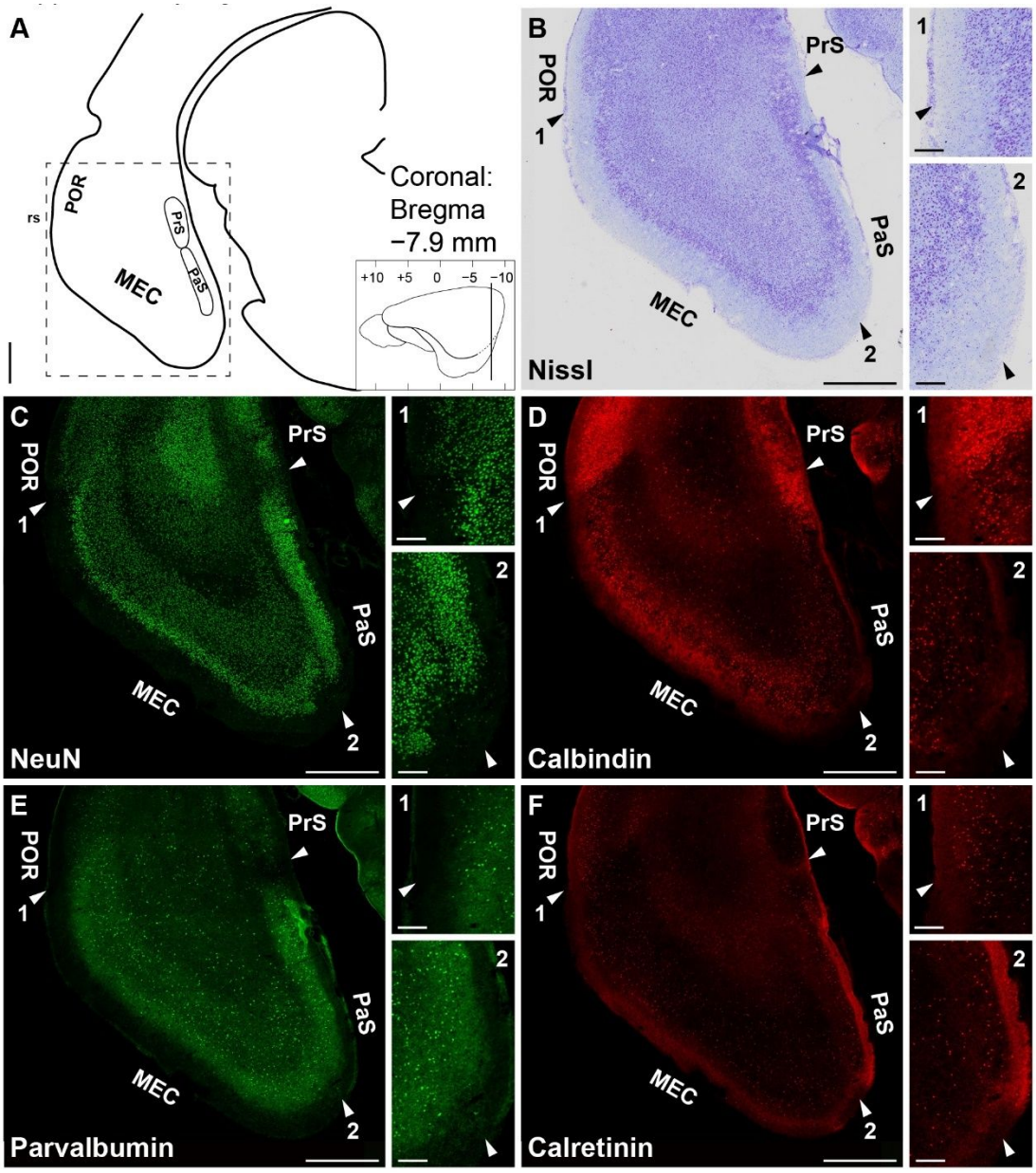

Supplementary Figure S7. Coronal sections through the tree shrew EC at 7.9 mm posterior to Bregma

A: Schematic diagram; boxed area indicates the field shown in B–F. Inset indicates the anteroposterior level. B: Nissl-stained section; arrows denote regional borders. C–F, Adjacent sections immunostained for NeuN (C) & calbindin (D), and parvalbumin (E) & calretinin (F). Abbreviations: EC, entorhinal cortex; MEC, medial entorhinal cortex; NeuN, neuronal nuclei; PaS, parasubiculum; POR, postrhinal cortex; PrS, presubiculum; rs, rhinal sulcus. Scale bars: 1 mm (diagram and overview images, left); 200 μm (magnified insets, right).

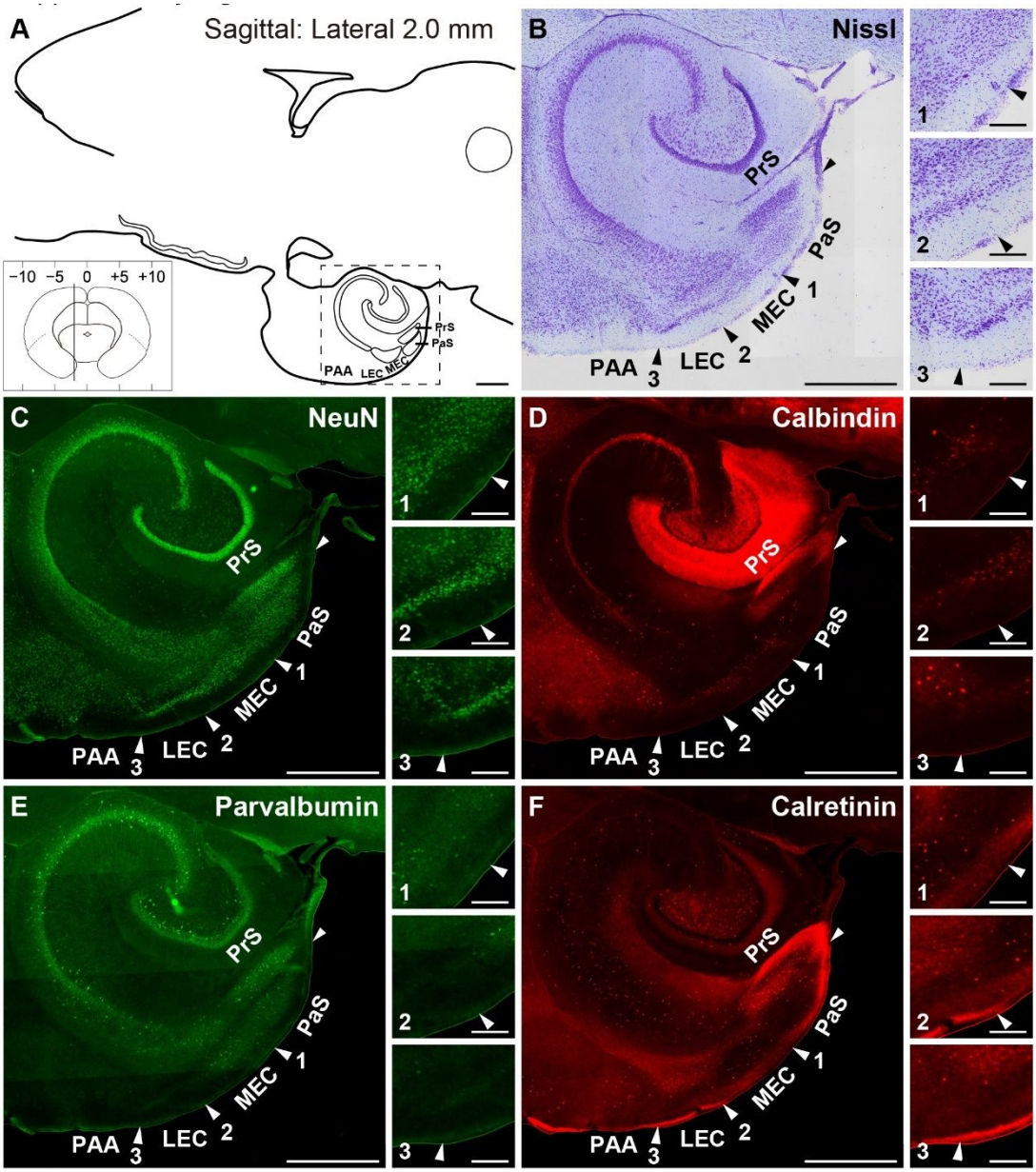

Supplementary Figure S8. Sagittal sections through the tree shrew EC at 2.0 mm lateral to the midline

A: Schematic diagram; boxed area indicates the field shown in B–F. Inset indicates the mediolateral level. B: Nissl-stained section; arrows denote regional borders. C–F, Adjacent sections immunostained for NeuN (C) & calbindin (D), and parvalbumin (E) & calretinin (F). Abbreviations: EC, entorhinal cortex; LEC, lateral entorhinal cortex; MEC, medial entorhinal cortex; NeuN, neuronal nuclei; PAA, periamygdaloid cortical area; PaS, parasubiculum; PrS, presubiculum. Scale bars: 1 mm (diagram and overview images, left); 200 μm (magnified insets, right).

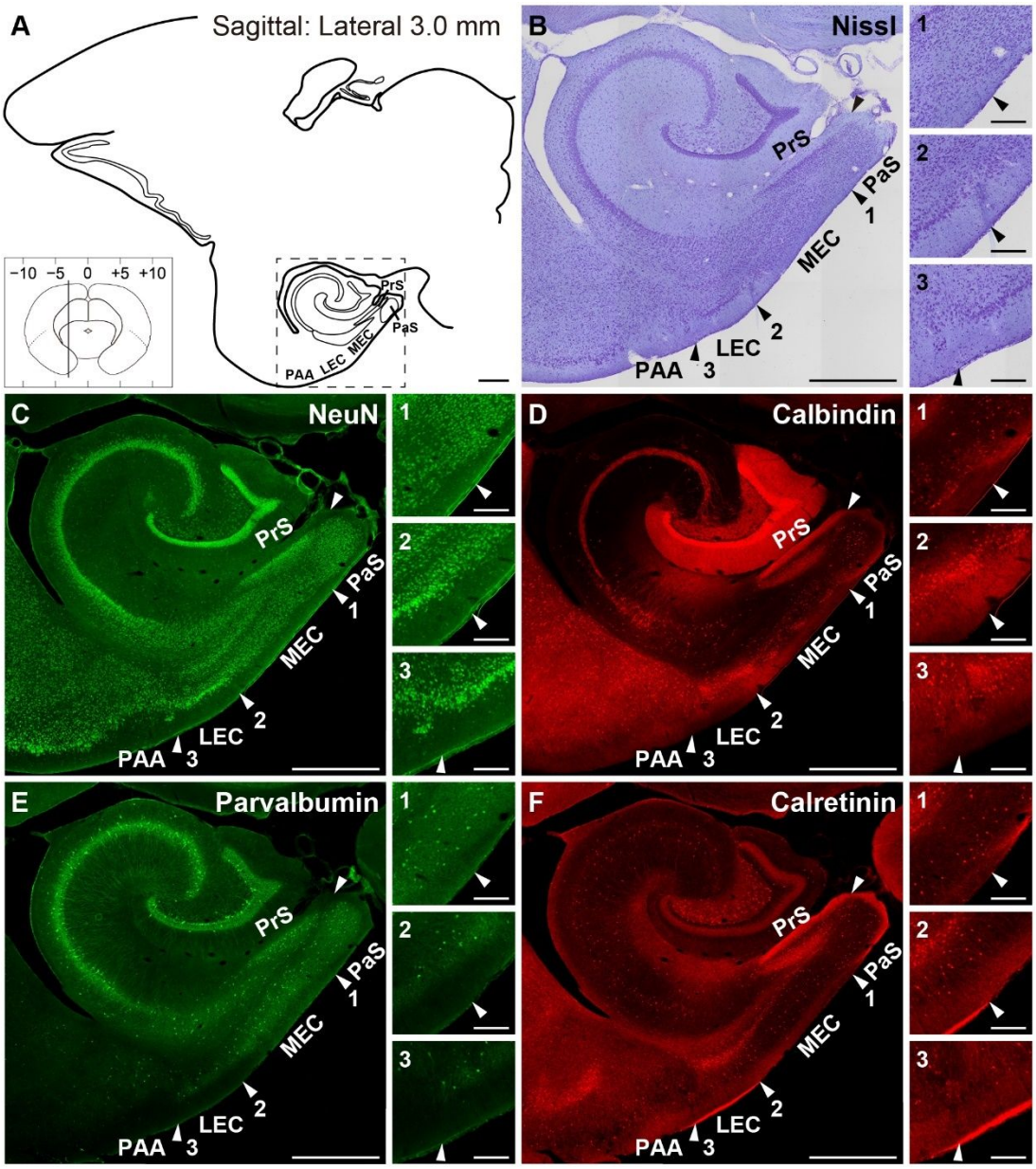

Supplementary Figure S9. Sagittal sections through the tree shrew EC at 3.0 mm lateral to the midline

A: Schematic diagram; boxed area indicates the field shown in B–F. Inset indicates the mediolateral level. B: Nissl-stained section; arrows denote regional borders. C–F, Adjacent sections immunostained for NeuN (C) & calbindin (D), and parvalbumin (E) & calretinin (F). Abbreviations: EC, entorhinal cortex; LEC, lateral entorhinal cortex; MEC, medial entorhinal cortex; NeuN, neuronal nuclei; PAA, periamygdaloid cortical area; PaS, parasubiculum; PrS, presubiculum. Scale bars: 1 mm (diagram and overview images, left); 200 μm (magnified insets, right).

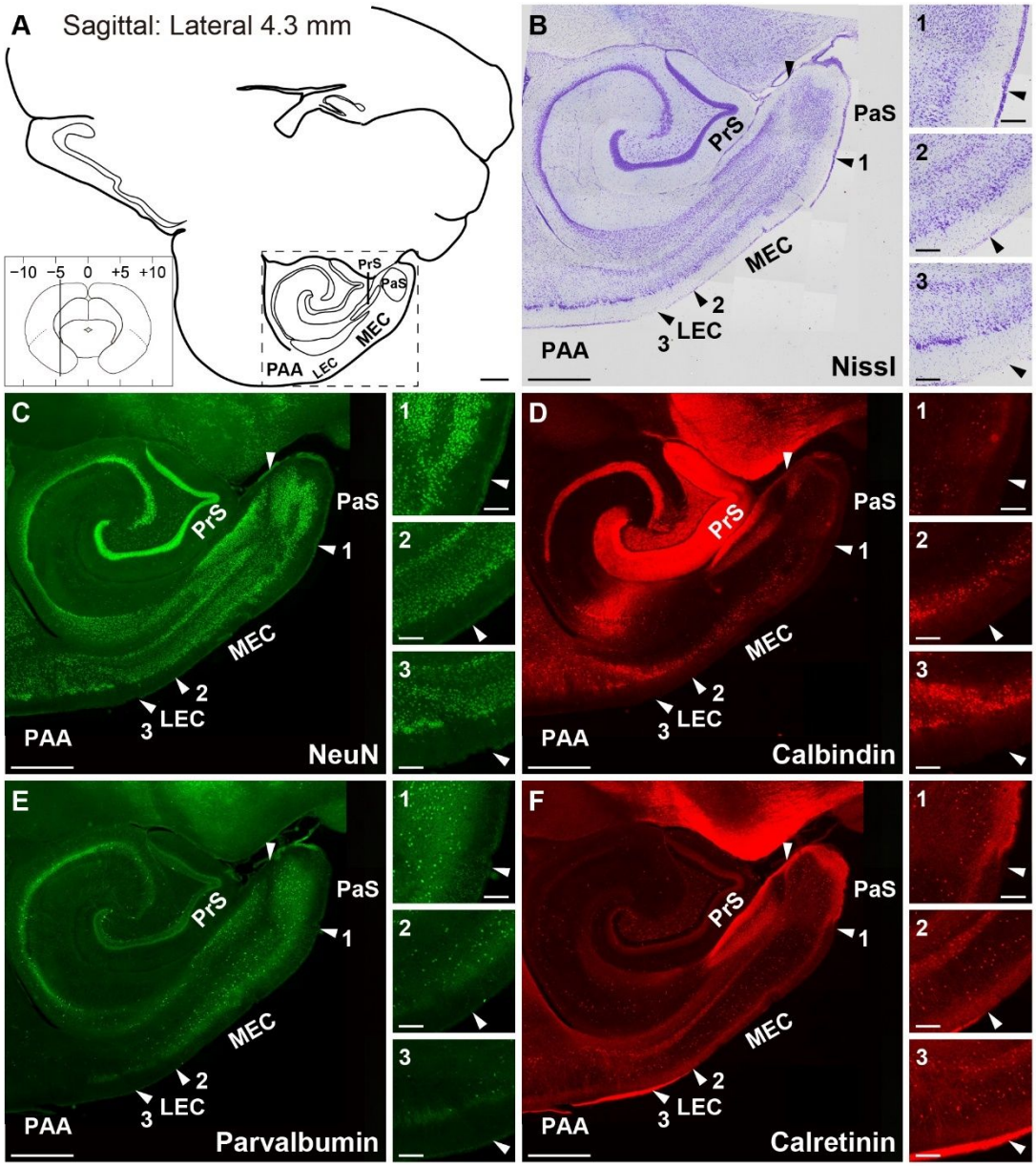

Supplementary Figure S10. Sagittal sections through the tree shrew EC at 4.3 mm lateral to the midline

A: Schematic diagram; boxed area indicates the field shown in B–F. Inset indicates the mediolateral level. B: Nissl-stained section; arrows denote regional borders. C–F, Adjacent sections immunostained for NeuN (C) & calbindin (D), and parvalbumin (E) & calretinin (F). Abbreviations: EC, entorhinal cortex; LEC, lateral entorhinal cortex; MEC, medial entorhinal cortex; NeuN, neuronal nuclei; PAA, periamygdaloid cortical area; PaS, parasubiculum; PrS, presubiculum. Scale bars: 1 mm (diagram and overview images, left); 200 μm (magnified insets, right).

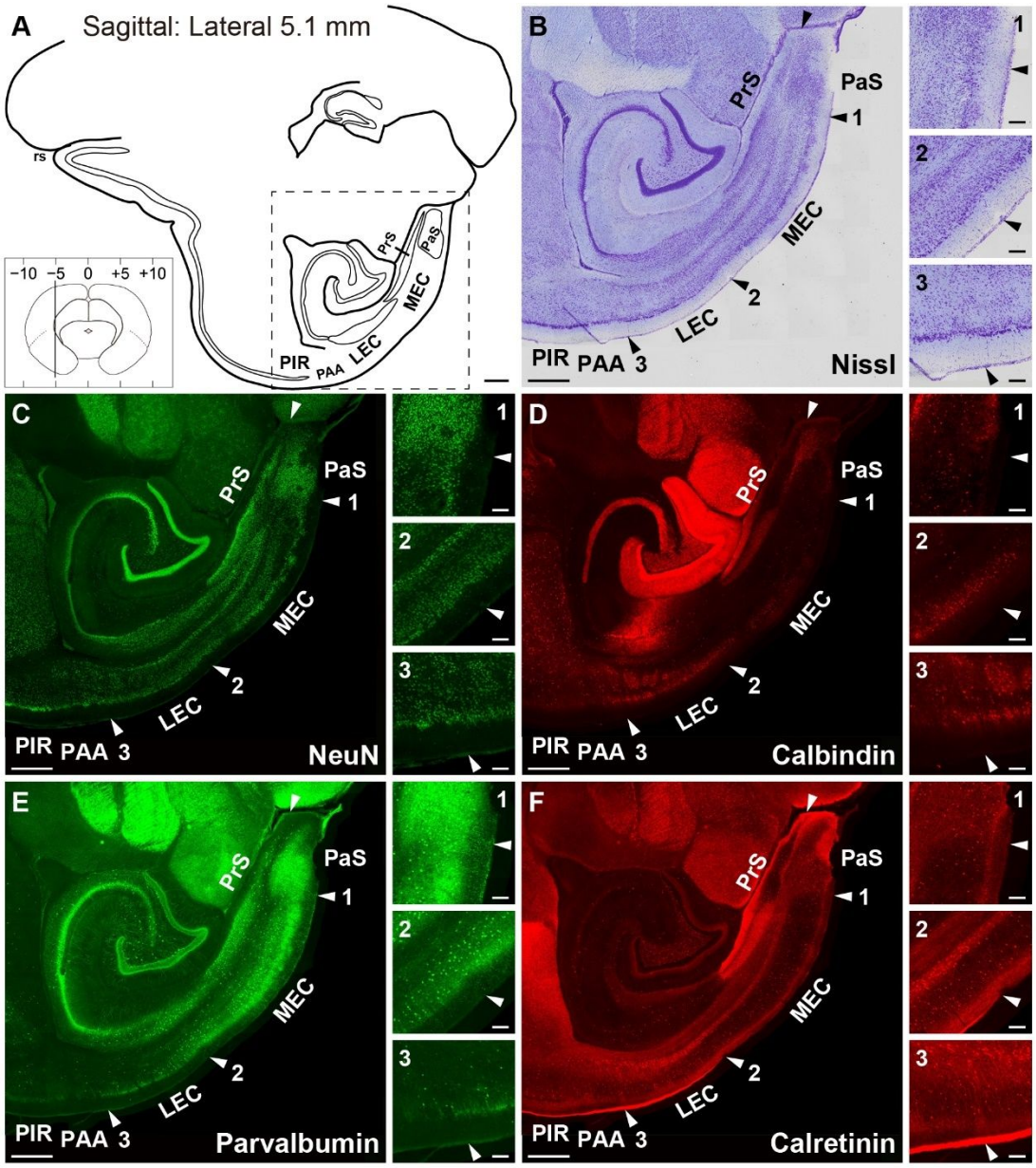

Supplementary Figure S11. Sagittal sections through the tree shrew EC at 5.1 mm lateral to the midline

A: Schematic diagram; boxed area indicates the field shown in B–F. Inset indicates the mediolateral level. B: Nissl-stained section; arrows denote regional borders. C–F, Adjacent sections immunostained for NeuN (C) & calbindin (D), and parvalbumin (E) & calretinin (F). Abbreviations: EC, entorhinal cortex; LEC, lateral entorhinal cortex; MEC, medial entorhinal cortex; NeuN, neuronal nuclei; PAA, periamygdaloid cortical area; PaS, parasubiculum; PIR, piriform cortex; PrS, presubiculum; rs, rhinal sulcus. Scale bars: 1 mm (diagram and overview images, left); 200 μm (magnified insets, right).

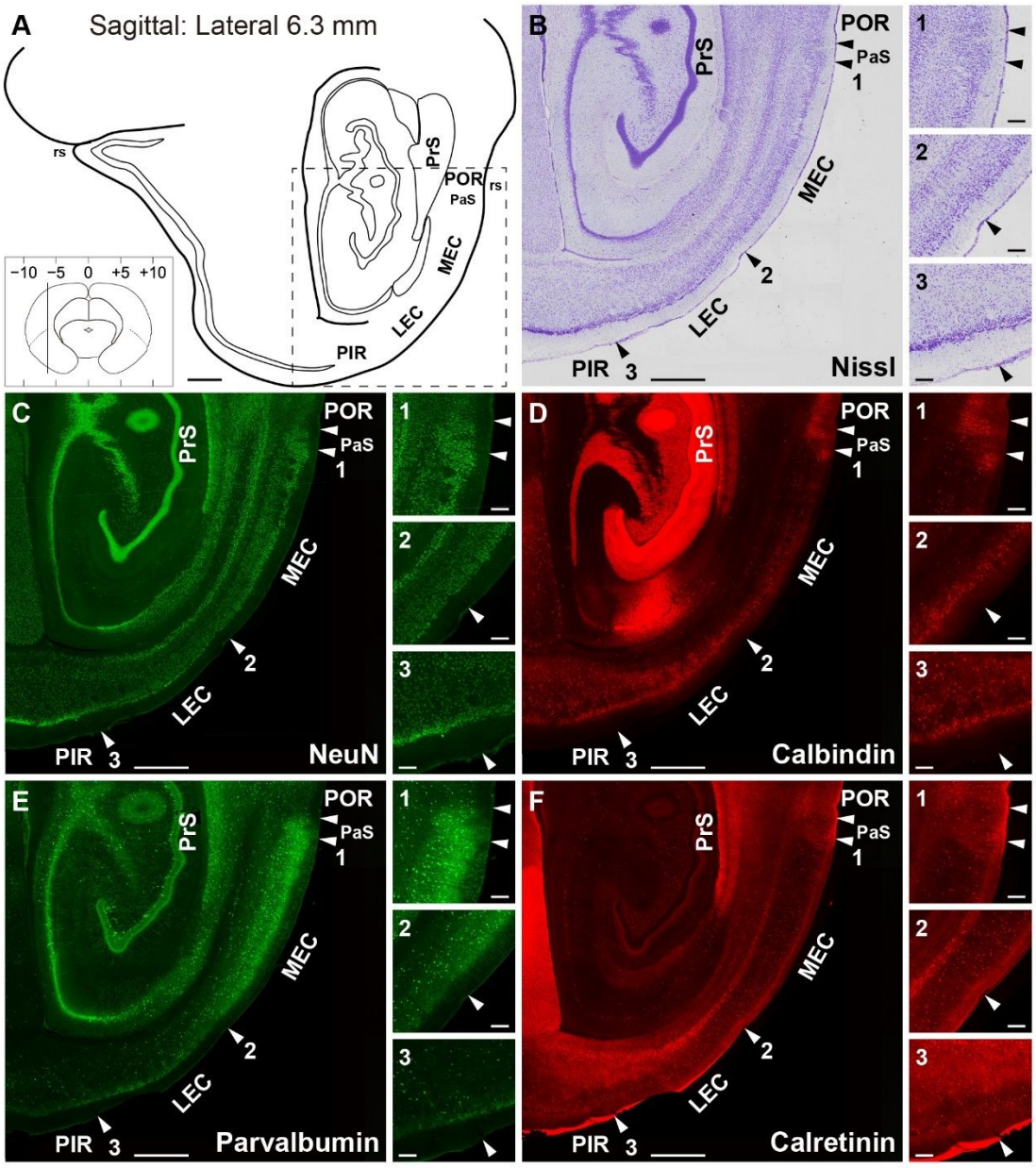

Supplementary Figure S12. Sagittal sections through the tree shrew EC at 6.3 mm lateral to the midline

A: Schematic diagram; boxed area indicates the field shown in B–F. Inset indicates the mediolateral level. B: Nissl-stained section; arrows denote regional borders. C–F, Adjacent sections immunostained for NeuN (C) & calbindin (D), and parvalbumin (E) & calretinin (F). Abbreviations: EC, entorhinal cortex; LEC, lateral entorhinal cortex; MEC, medial entorhinal cortex; NeuN, neuronal nuclei; PaS, parasubiculum; PIR, piriform cortex; POR, postrhinal cortex; PrS, presubiculum; rs, rhinal sulcus. Scale bars: 1 mm (diagram and overview images, left); 200 μm (magnified insets, right).

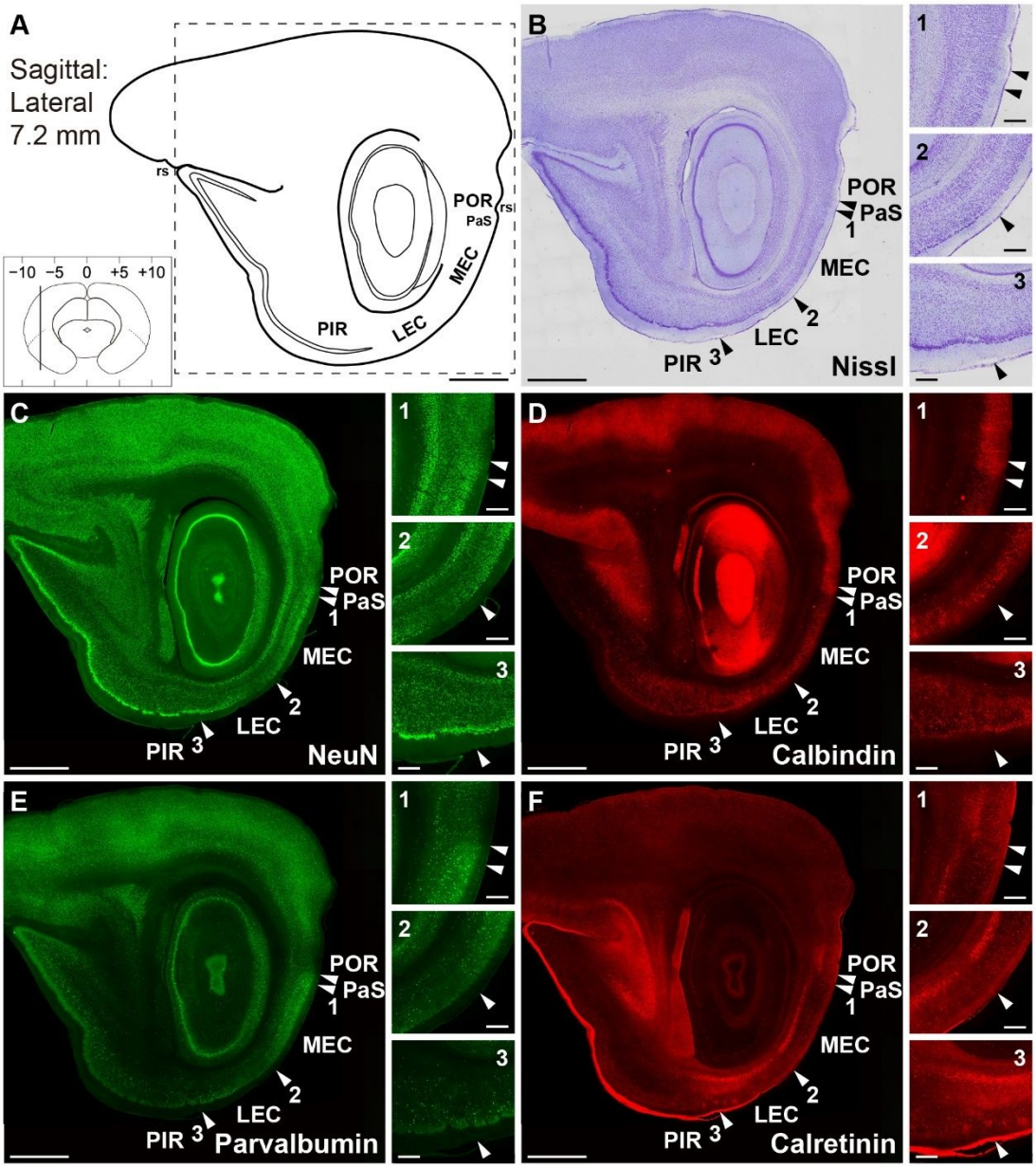

1715

1716 **Supplementary Figure S13. Sagittal sections through the tree shrew EC at 7.2 mm**
1717 **lateral to the midline**

1718 A: Schematic diagram; boxed area indicates the field shown in B–F. Inset indicates the
1719 mediolateral level. B: Nissl-stained section; arrows denote regional borders. C–F,
1720 Adjacent sections immunostained for NeuN (C) & calbindin (D), and parvalbumin (E)
1721 & calretinin (F). Abbreviations: EC, entorhinal cortex; LEC, lateral entorhinal cortex;
1722 MEC, medial entorhinal cortex; NeuN, neuronal nuclei; PaS, parasubiculum; PIR,
1723 piriform cortex; POR, postrhinal cortex; rs, rhinal sulcus. Scale bars: 1 mm (diagram
1724 and overview images, left); 200 μm (magnified insets, right).

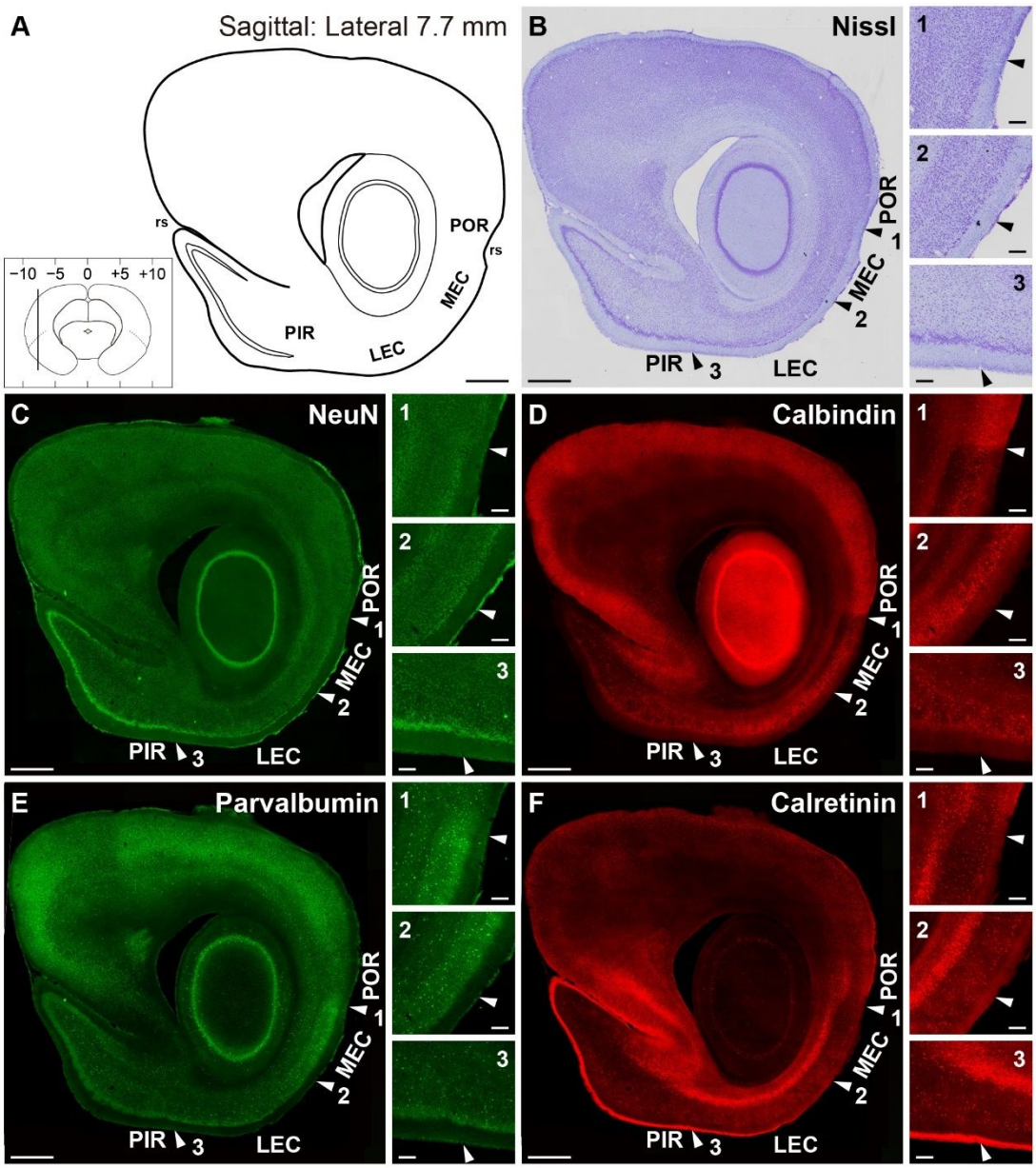

Supplementary Figure S14. Sagittal sections through the tree shrew EC at 7.7 mm lateral to the midline

A: Schematic diagram; boxed area indicates the field shown in B–F. Inset indicates the mediolateral level. B: Nissl-stained section; arrows denote regional borders. C–F, Adjacent sections immunostained for NeuN (C) & calbindin (D), and parvalbumin (E) & calretinin (F). Abbreviations: EC, entorhinal cortex; LEC, lateral entorhinal cortex; MEC, medial entorhinal cortex; NeuN, neuronal nuclei; PIR, piriform cortex; POR, postrhinal cortex; rs, rhinal sulcus. Scale bars: 1 mm (diagram and overview images, left); 200 μm (magnified insets, right).

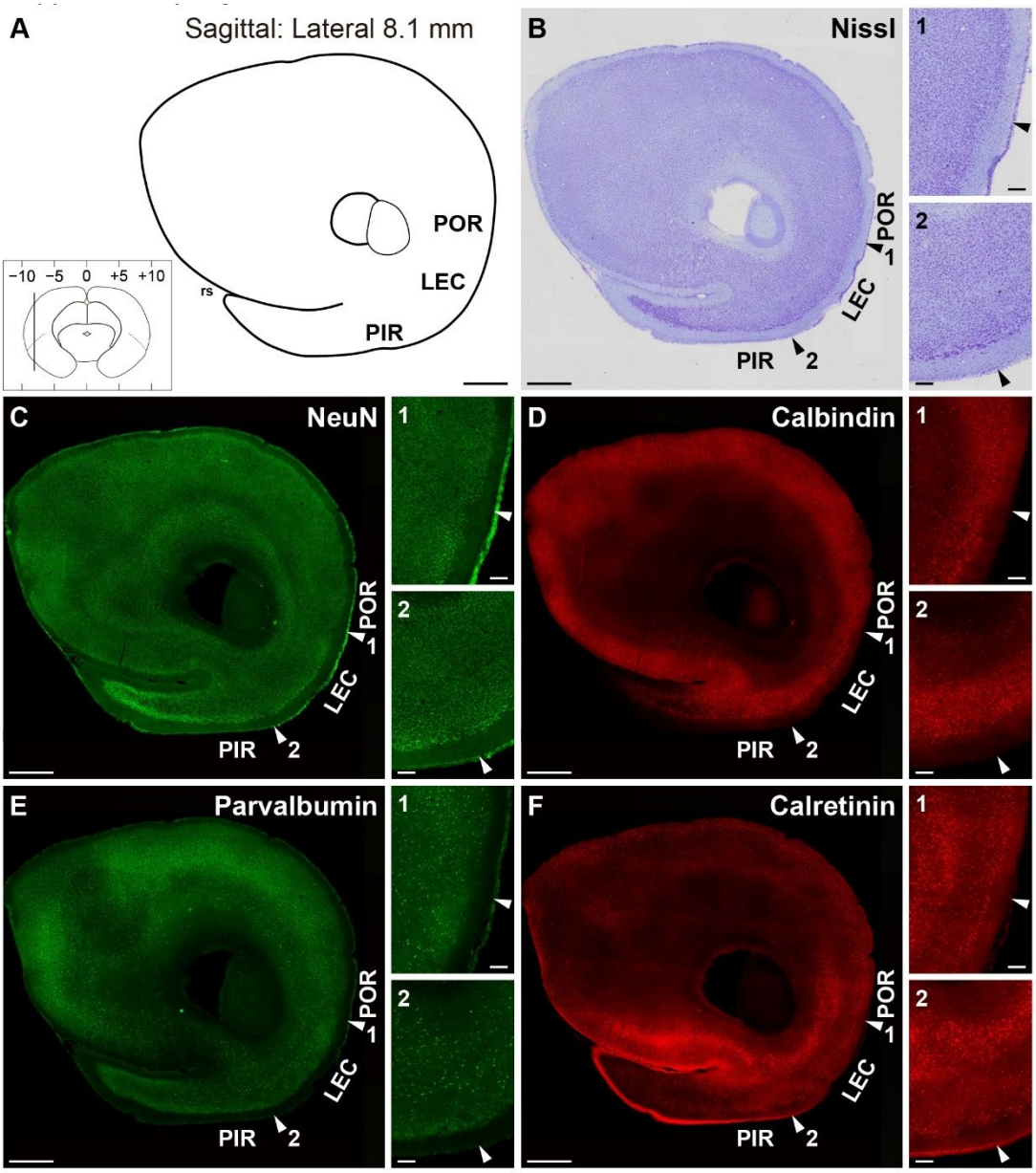

Supplementary Figure S15. Sagittal sections through the tree shrew EC at 8.1 mm lateral to the midline

A: Schematic diagram; boxed area indicates the field shown in B–F. Inset indicates the mediolateral level. B: Nissl-stained section; arrows denote regional borders. C–F, Adjacent sections immunostained for NeuN (C) & calbindin (D), and parvalbumin (E) & calretinin (F). Abbreviations: EC, entorhinal cortex; LEC, lateral entorhinal cortex; NeuN, neuronal nuclei; PIR, piriform cortex; POR, postrhinal cortex; rs, rhinal sulcus. Scale bars: 1 mm (diagram and overview images, left); 200 μm (magnified insets, right).

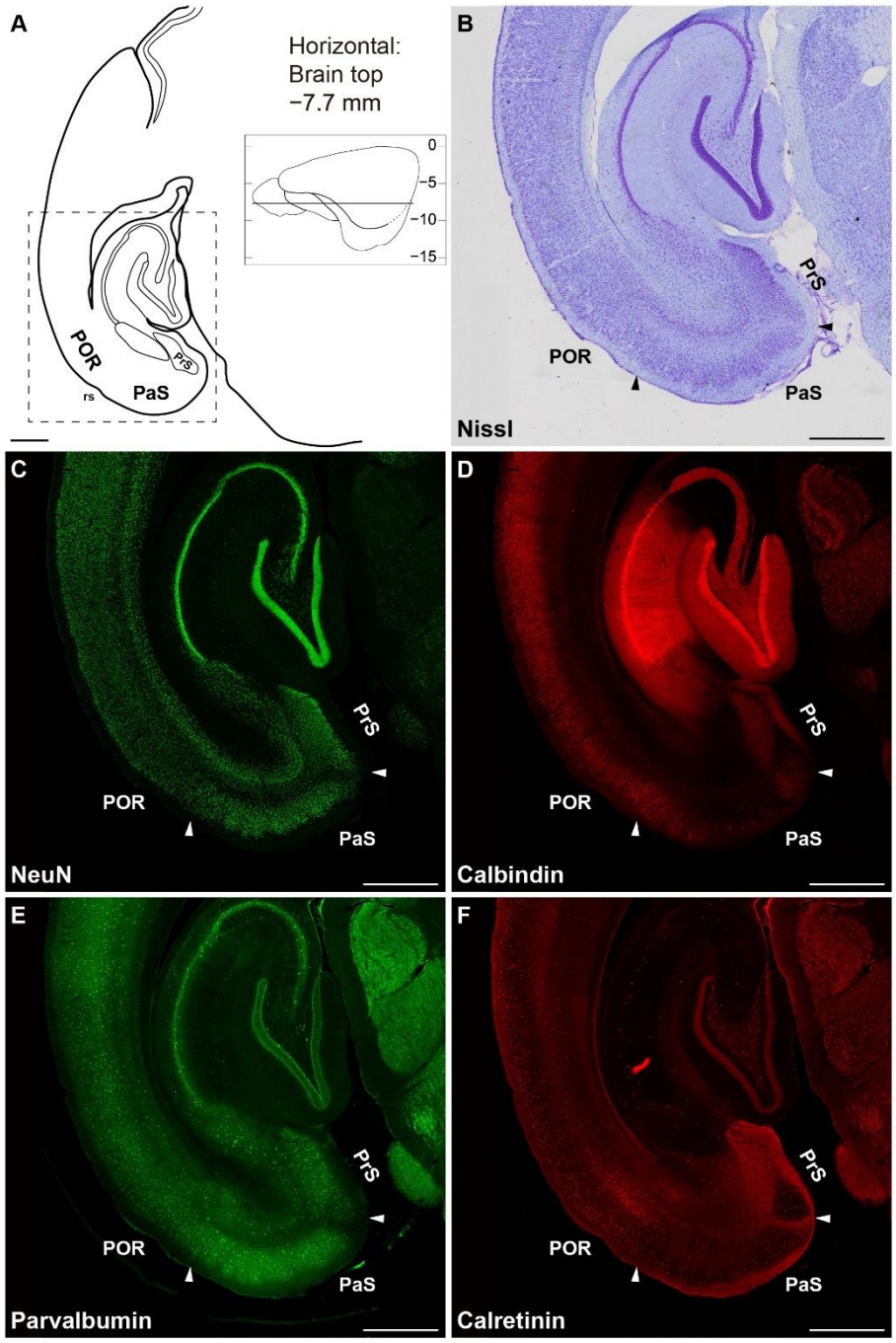

Supplementary Figure S16. Horizontal sections through the tree shrew para-hippocampal region at 7.7 mm below the dorsal cortical surface

A: Schematic diagram; boxed area indicates the field shown in B–F. Inset indicates the dorsoventral level. B: Nissl-stained section; arrows denote regional borders. C–F, Adjacent sections immunostained for NeuN (C) & calbindin (D), and parvalbumin (E) & calretinin (F). Abbreviations: NeuN, neuronal nuclei; PaS, parasubiculum; POR, postrhinal cortex; PrS, presubiculum; rs, rhinal sulcus. Scale bars: 1 mm.

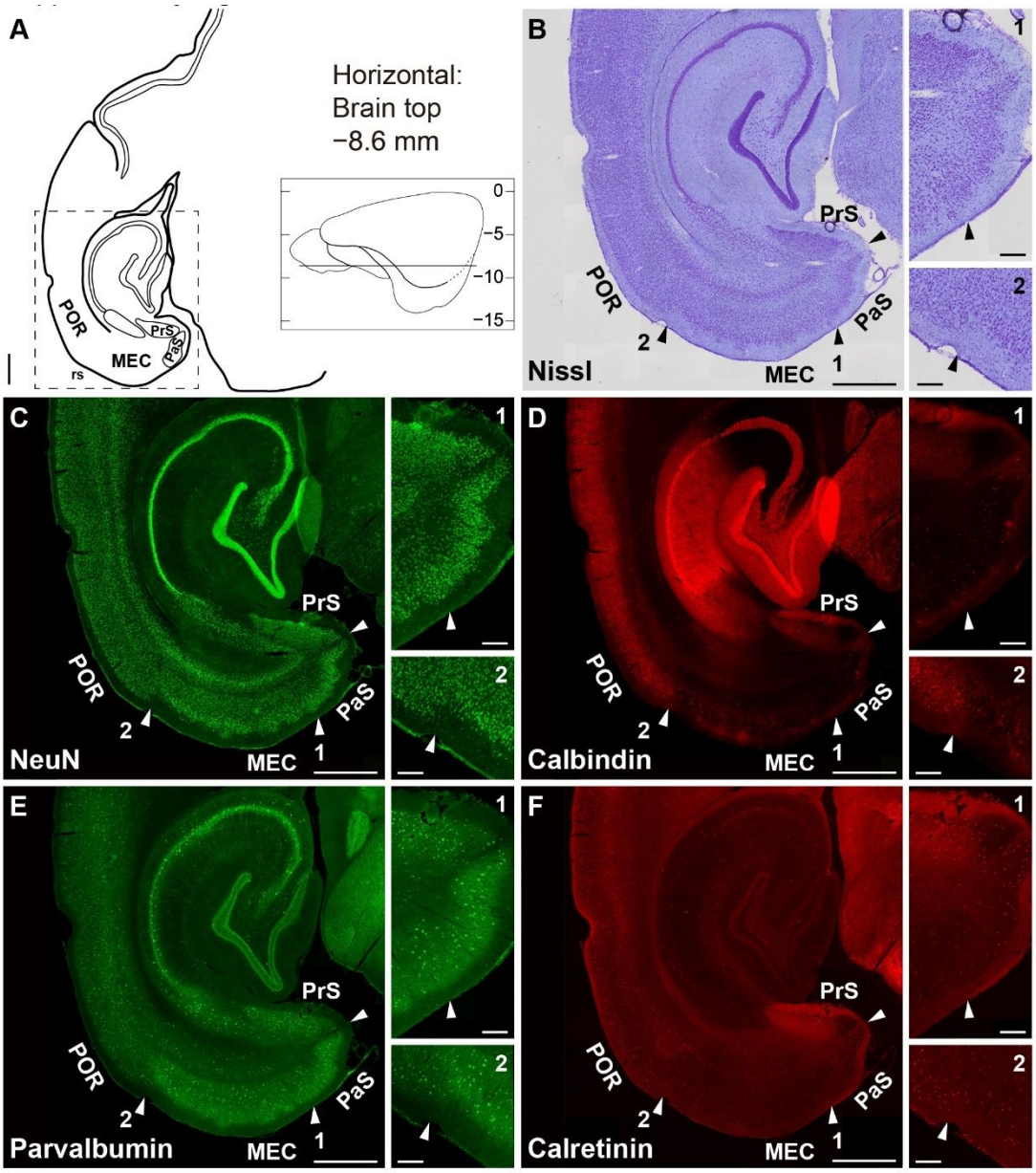

Supplementary Figure S17. Horizontal sections though the tree shrew EC at 8.6 mm below the dorsal cortical surface

A: Schematic diagram; boxed area indicates the field shown in B–F. Inset indicates the dorsoventral level. B: Nissl-stained section; arrows denote regional borders. C–F, Adjacent sections immunostained for NeuN (C) & calbindin (D), and parvalbumin (E) & calretinin (F). Abbreviations: EC, entorhinal cortex; MEC, medial entorhinal cortex; NeuN, neuronal nuclei; PaS, parasubiculum; POR, postrhinal cortex; PrS, presubiculum; rs, rhinal sulcus. Scale bars: 1 mm (diagram and overview images, left); 200 μm (magnified insets, right).

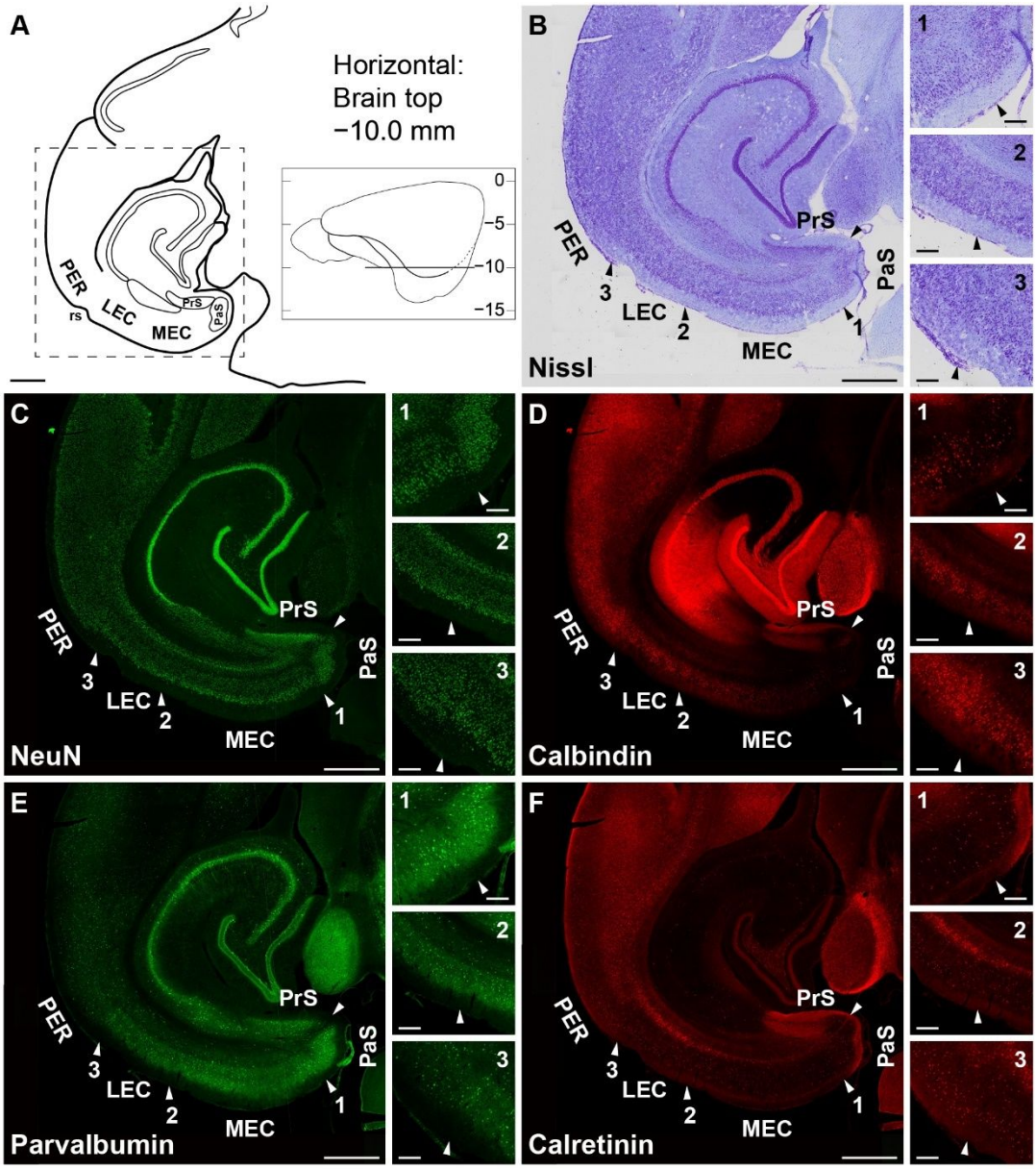

1762

1763 **Supplementary Figure S18. Horizontal sections through the tree shrew EC at 10.0**
1764 **mm below the dorsal cortical surface**

1765 A: Schematic diagram; boxed area indicates the field shown in B–F. Inset indicates the
1766 dorsoventral level. B: Nissl-stained section; arrows denote regional borders. C–F,
1767 Adjacent sections immunostained for NeuN (C) & calbindin (D), and parvalbumin (E)
1768 & calretinin (F). Abbreviations: EC, entorhinal cortex; LEC, lateral entorhinal cortex;
1769 MEC, medial entorhinal cortex; NeuN, neuronal nuclei; PaS, parasubiculum; PER,
1770 perirhinal cortex; PrS, presubiculum; rs, rhinal sulcus. Scale bars: 1 mm (diagram and
1771 overview images, left); 200 μm (magnified insets, right).

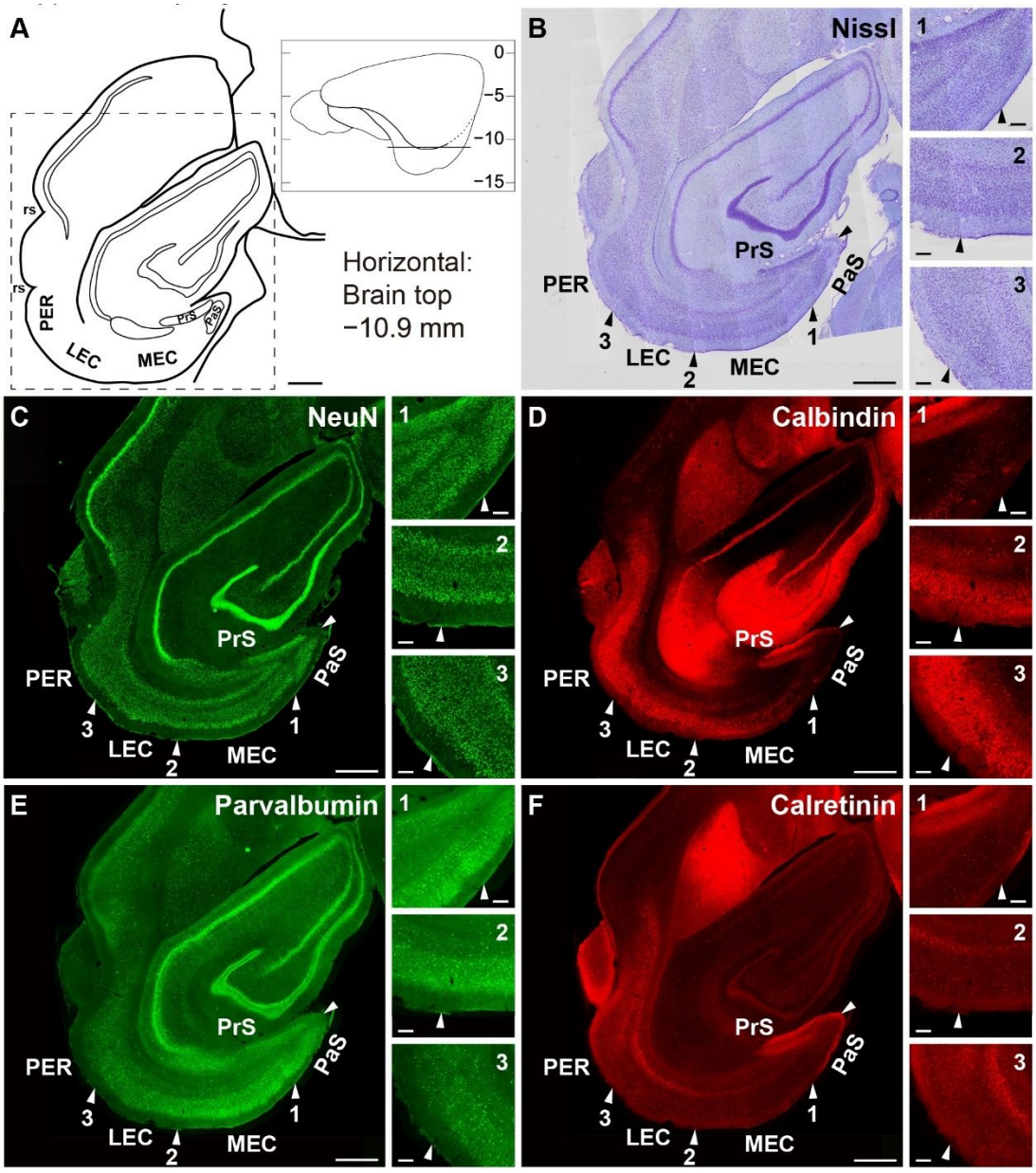

1772

1773 **Supplementary Figure S19 Horizontal sections though the tree shrew EC at 10.9**

1774 **mm below the cortical surface**

1775 A: Schematic diagram; boxed area indicates the field shown in B–F. Inset indicates the

1776 dorsoventral level. B: Nissl-stained section; arrows denote regional borders. C–F,

1777 Adjacent sections immunostained for NeuN (C) & calbindin (D), and parvalbumin (E)

1778 & calretinin (F). Abbreviations: EC, entorhinal cortex; LEC, lateral entorhinal cortex;

1779 MEC, medial entorhinal cortex; NeuN, neuronal nuclei; PaS, parasubiculum; PER,

1780 perirhinal cortex; PrS, presubiculum; rs, rhinal sulcus. Scale bars: 1 mm (diagram and

1781 overview images, left); 200 μm (magnified insets, right).

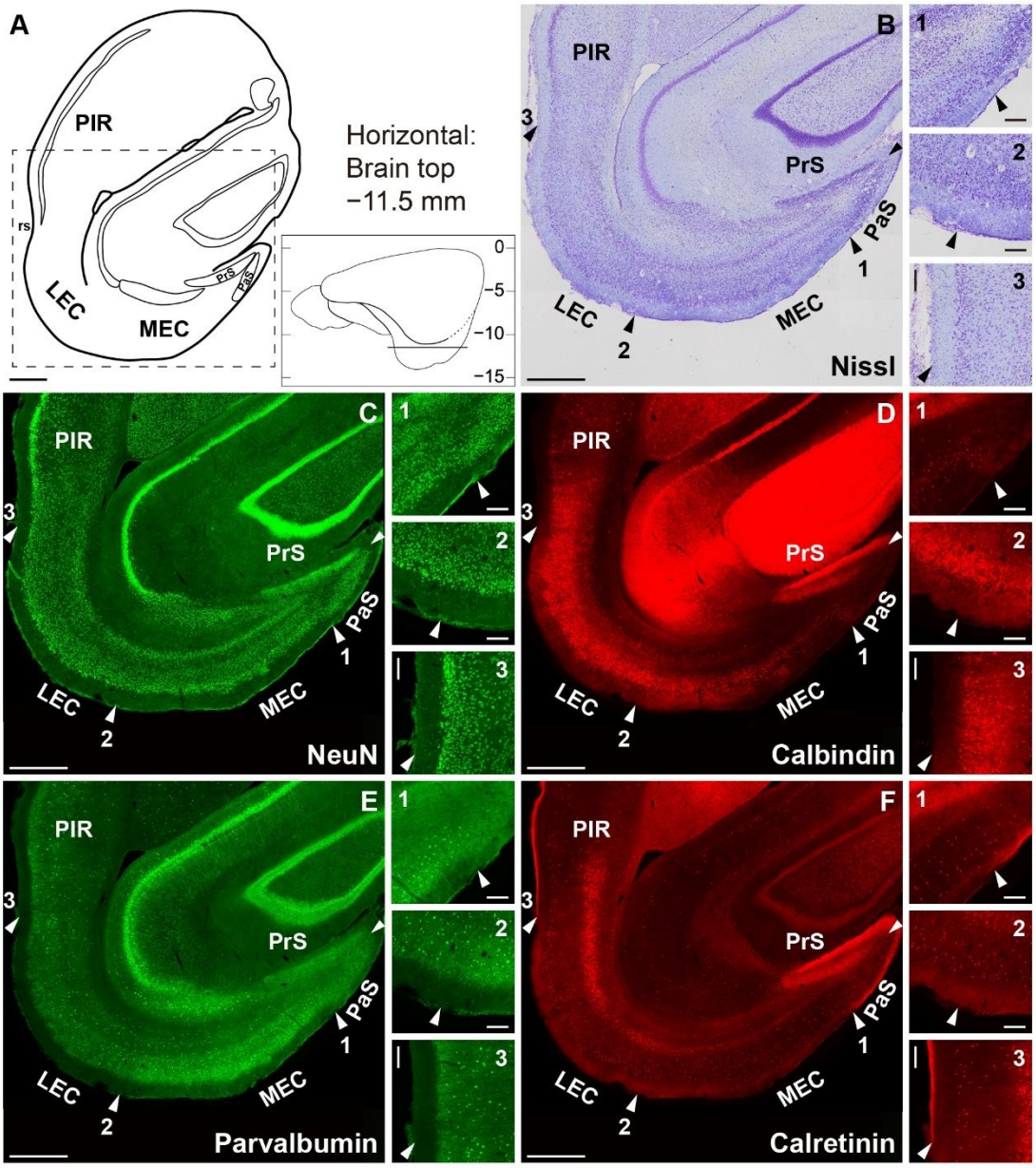

Supplementary Figure S20. Horizontal sections through the tree shrew EC at 11.5 mm below the dorsal cortical surface

A: Schematic diagram; boxed area indicates the field shown in B–F. Inset indicates the dorsoventral level. B: Nissl-stained section; arrows denote regional borders. C–F, Adjacent sections immunostained for NeuN (C) & calbindin (D), and parvalbumin (E) & calretinin (F). Abbreviations: EC, entorhinal cortex; LEC, lateral entorhinal cortex; MEC, medial entorhinal cortex; NeuN, neuronal nuclei; PaS, parasubiculum; PIR, piriform cortex; PrS, presubiculum; rs, rhinal sulcus. Scale bars: 1 mm (diagram and overview images, left); 200 μm (magnified insets, right).

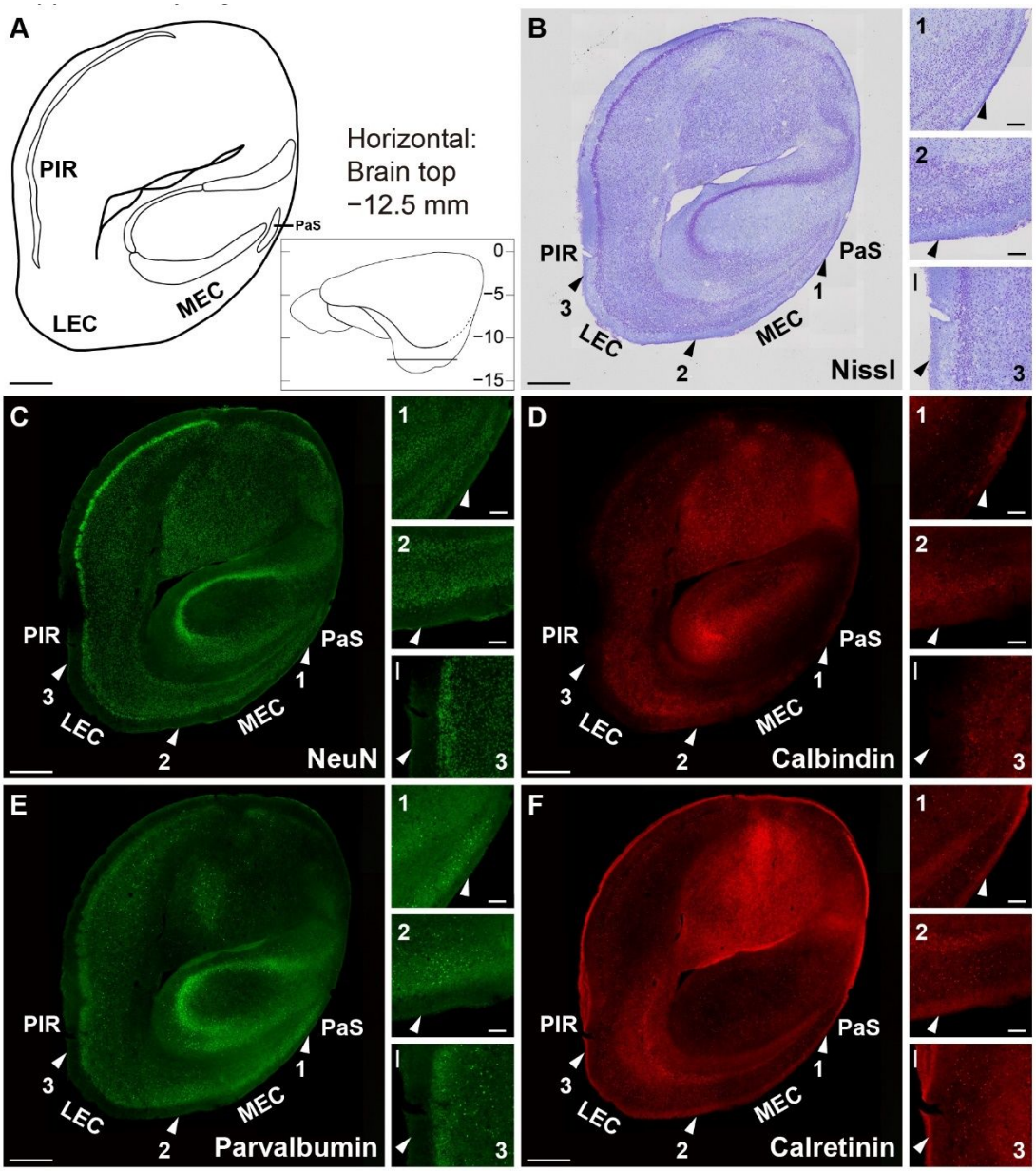

Supplementary Figure S21. Horizontal sections through the tree shrew EC at 12.5 mm below the dorsal cortical surface

A: Schematic diagram; boxed area indicates the field shown in B–F. Inset indicates the dorsoventral level. B: Nissl-stained section; arrows denote regional borders. C–F, Adjacent sections immunostained for NeuN (C) & calbindin (D), and parvalbumin (E) & calretinin (F). Abbreviations: EC, entorhinal cortex; LEC, lateral entorhinal cortex; MEC, medial entorhinal cortex; NeuN, neuronal nuclei; PaS, parasubiculum; PIR, piriform cortex. Scale bars: 1 mm (diagram and overview images, left); 200 μm (magnified insets, right).

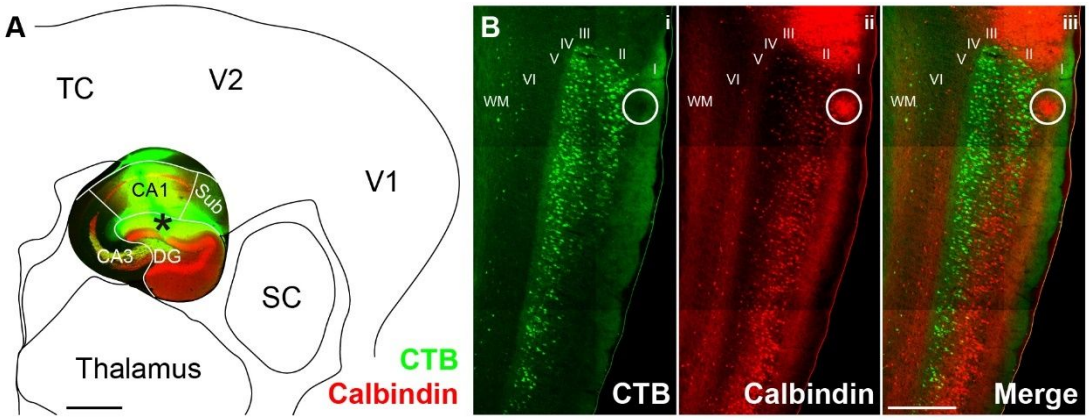

Supplementary Figure S22. Calbindin-rich clusters in MEC do not contribute to the hippocampal projection.

A: Another example of CTB injection (star) in dorsal hippocampus. Green fluorescence covers CA1, subiculum and DG. B: Entorhinal section co-stained for calbindin. A calbindin-rich cluster (circle) contains no CTB-positive neurons. Sparse retrogradely labeled somata are restricted to layer VI and white matter of MEC; layer V is devoid of labeling. Abbreviations: CTB, cholera toxin subunit B; DG, dentate gyrus; MEC, medial entorhinal cortex; SC, superior colliculus; Sub, subiculum; TC: temporal cortex; V1, primary visual cortex; V2, secondary visual cortex; WM, white matter. Scale bars: 1 mm.

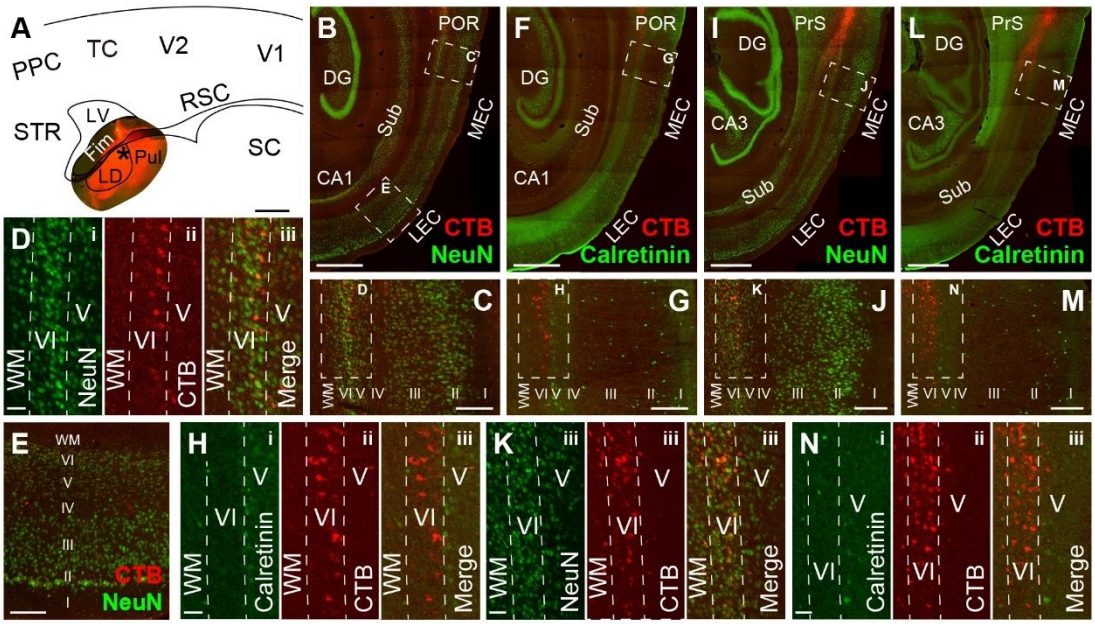

Supplementary Figure S23. Entorhinal layer VI identified by thalamus-projecting neurons.

A: CTB injection site (star) centered in laterodorsal thalamic nucleus with spread into pulvinar. B: NeuN-co-stained section showing CTB+ neurons clustered at the dorsal limit of MEC, matching earlier primate observations (Aggleton et al., 1986). C: Magnified view of upper boxed region in B. Roman numerals indicate layers. D: Higher-magnification view of boxed area in C; dashed lines delimit layers, confirming CTB+ somata coincide with the dense NeuN band of layer VI. E: Lower boxed region in B; no CTB signal is detected in LEC. F–H: Adjacent section co-stained for calretinin; CTB+ somata are confined to calretinin-poor layer VI, whereas calretinin-rich layer V is unlabeled. I–N: Series at a more medial level, arranged as in B–H; retrogradely labeled cells remain restricted to layer VI. Abbreviations: CTB, cholera toxin subunit B; DG, dentate gyrus; Fim, fimbria of the hippocampus; LEC, lateral entorhinal cortex; LD, laterodorsal thalamic nucleus; LV, lateral ventricle; MEC, medial entorhinal cortex; NeuN, neuronal nuclei; POR, postrhinal cortex; PPC, Posterior parietal cortex; Pul, pulvinar; RSC, retrosplenial cortex; SC, superior colliculus; TC, temporal cortex; STR, striatum; Sub, subiculum; V1, primary visual cortex; V2, secondary visual cortex; WM, white matter. Scale bars: 1 mm (A, B, F, I, L), 200 μm (C, E, G, J, M), 50 μm (D, H, K, N).

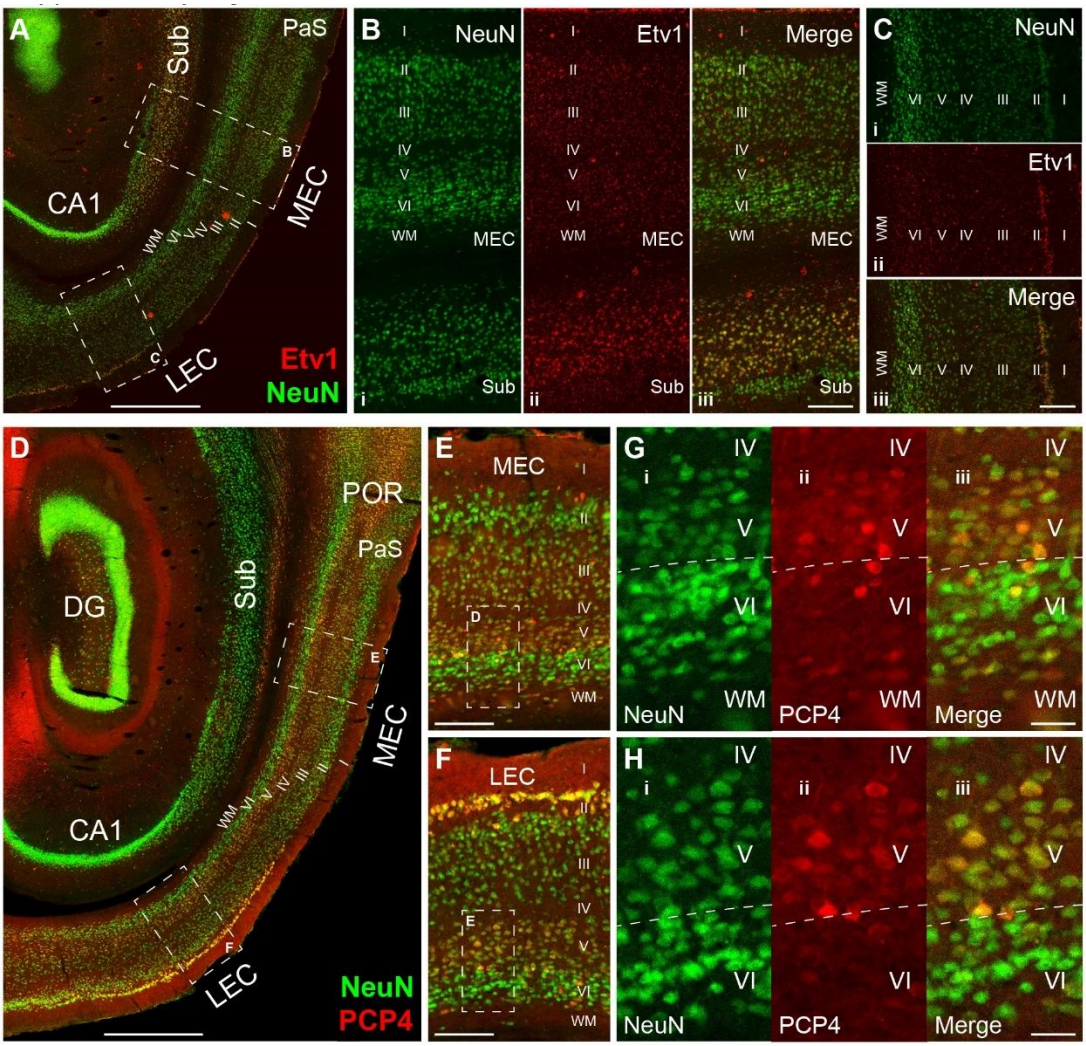

1841

1842 **Supplementary Figure S24. Etv1 and PCP4 do not demarcate entorhinal layer V**
1843 **sublayers.**

1844 A: Etv1 labeling (red) with NeuN (green) in the EC and hippocampus. Roman numerals
1845 label entorhinal layers. B, C: Enlargements of boxed regions in A; Etv1 signal is absent
1846 from layer V of both MEC and LEC. D: PCP4 immunofluorescence (red) with NeuN
1847 (green) across the EC. E, F: Magnified views of boxed regions in D; PCP4 is uniformly
1848 expressed throughout layer V in both MEC and LEC. G, H: High-magnification views
1849 of boxed areas in E and F; dashed lines mark the layer V/VI border. Abbreviations: DG,
1850 dentate gyrus; EC, entorhinal cortex; Etv1, ETS variant 1; LEC, lateral entorhinal
1851 cortex; MEC, medial entorhinal cortex; NeuN, neuronal nuclei; PCP4, Purkinje-cell
1852 protein 4; Sub, subiculum, WM, white matter. Scale bars: 1 mm (A, D), 200 μm (B, C,
1853 E, F), 50 μm (G, H).

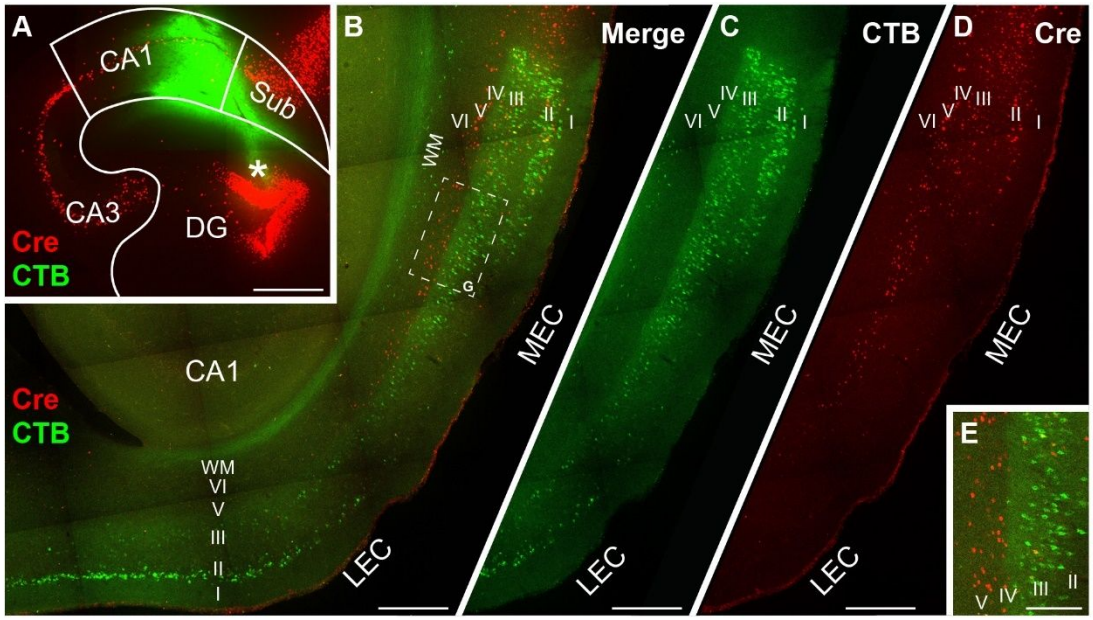

Supplementary Figure S25. Tree shrew entorhinal layer V does not project to CA1.

A: Dual delivery of CTB (green) and AAV-Cre (red) to dorsal CA1 and subiculum. B: Sagittal entorhinal section: CTB+ neurons fill superficial layers of MEC and LEC, but are absent from layer V; Cre+ somata concentrate in layer V, with intermittent superficial cells likely retrogradely labeled. Roman numerals denote cortical layers. C, D: Single-channel images of the section in B confirming no CTB signal in layer V. E: Higher-magnification view of boxed region in B; the absence of CTB labeling demonstrates that Cre+ layer V neurons are hippocampal-recipient, not hippocampus-projecting, in tree shrews. Abbreviations: CTB, cholera toxin subunit B; DG, dentate gyrus; LEC, lateral entorhinal cortex; MEC, medial entorhinal cortex; Sub, subiculum; WM, white matter. Scale bars: 500 μm (A–D), 200 μm (E).

基于细胞构筑、化学构筑及神经连接特征的树鼩内嗅皮层区域与层状组织架构

短标题：树鼩内嗅皮层的亚区划分与层状结构

作者

叶一帆[1,2,5], 邓 楚[1,2,5], 葛晓帆[1,2], 张 榕[1,3], 龙佳丽[1,2], 贾佳雪[1,2], 叶浩云[1], 李成季[1,3], 蔡 星[1,3], Menno P. Witter[4], & 卢 立[1,3,6]

作者单位

[1]**中国科学院昆明动物研究所** 遗传资源与进化国家重点实验室、云南省动物模型与人类疾病机理重点实验室，云南 昆明 650201

[2]**中国科学院大学昆明生命科学学院**，云南 昆明 650204

[3]**中国科学院昆明动物研究所** 非人灵长类资源库、昆明灵长类研究中心、模式动物表型与遗传研究国家重大科技基础设施（灵长类设施），云南 昆明 650107

[4]**Kavli Institute for Systems Neuroscience, NTNU Norwegian University of Science and Technology, Trondheim 7491, Norway.**

[5]**共同第一作者（贡献等同）**

[6]**通讯作者**：卢 立，E-mail：luli@mail.kiz.ac.cn，电话：+86-871-65155338

摘要

内嗅皮层（EC）作为关键的信息整合与传递枢纽，主要功能是整合多模态皮层及皮层

下信息并传入海马结构，同时将海马输出信息投射至端脑的各个区域，该脑区也是阿尔茨海默病（AD）发生中受影响最早、病变最严重的脑区之一。尽管中缅树鼩已成为AD 疾病研究中极具潜力的模式动物，但由于其内部嗅皮层的结构分布尚未被系统解析，极大限制了该动物模型在 AD 早期病程建模中的应用价值。本研究结合细胞构筑、化学构筑技术及神经示踪实验，通过明确界定中缅树鼩内嗅皮层与其他脑区的边界、精准划分其内侧与外侧亚区、系统绘制其层状结构图谱，成功为该物种的内嗅皮层构建了一套全面、精细的解剖学参考体系。本研究发现，中缅树鼩内嗅皮层的结构兼具啮齿类与猴类动物的特征，呈现出介于两者之间的过渡性架构，这一特征与其系统发育地位高度契合，并且可能与从啮齿类到灵长类的空间位置编码机制的逐步演化过程存在关联。本研究首次绘制了中缅树鼩内嗅皮层的精细化解剖图谱，不仅为后续相关神经示踪、电生理等研究奠定了关键基础，同时也进一步提升了中缅树鼩在空间编码和记忆的机制研究，以及 AD 早期自然病程模型构建中的应用潜力。

关键词

关键词：树鼩内嗅皮层；边界界定与亚区划分；层状组织架构；细胞构筑；化学构筑；连接特征